

**MODELING DISTAL PULMONARY PHYSIOLOGY IN
MICROPHYSIOLOGICAL SYSTEMS**

A Dissertation
Presented to
The Academic Faculty

by

Hannah Viola

In Partial Fulfillment
of the Requirements for the Degree
Doctorate of Philosophy
in Bioengineering

Georgia Institute of Technology
December 2022

COPYRIGHT © 2022 BY HANNAH VIOLA

**MODELING DISTAL PULMONARY PHYSIOLOGY
IN MICROPHYSIOLOGICAL SYSTEMS**

Approved by:

Dr. Shuichi Takayama, Adviser
The Wallace H. Coulter
Department of Biomedical Engineering
Georgia Institute of Technology

Dr. Hang Lu
School of Chemical and
Biomolecular Engineering
Georgia Institute of Technology

Dr. Rabindra Tirouvanziam
Department of Pediatrics
Center for Cystic Fibrosis Research
Emory University School of Medicine

Dr. Andrés García
George W. Woodruff
School of Mechanical Engineering
Georgia Institute of Technology

Dr. Jocelyn Grunwell
Department of Pediatrics
Division of Critical Care Medicine
Emory University School of Medicine

Date Approved: August 9th, 2022

To my beloved cat, Boosta.

ACKNOWLEDGEMENTS

Science is a team effort, and so is life. Both of them are also really hard.

First, thank you to every administrative assistant, custodial staff member, and barista I have ever interacted with. Special appreciation to Kay the custodian, Mo from Nectar, Greg from VWR, and magicians Aeryal Herrod and Ana Cleves from ordering. Y'all are the backbone of scientific progress and we owe you everything.

Shout out to my family and friends for your unending tolerance for listening to me talk about my project for like 1,000 hours. Especially Mom and Dad, Nicole, CJ, Maria, and Alexa. Y'all should get an honorary doctorate for learning how lungs work and what a neutrophil is and why I'm so obsessed with them. And for teaching me how to be a student, teacher, mentor, friend, advocate, and of course, a scientist.

Thank you to my adviser, Dr. Shuichi Takayama, and my committee Drs. Hang Lu, Andrés García, Jocelyn Grunwell, Rabindra Tirouvanziam for their guidance and support in shaping this project and developing my scientific skills. I am also very thankful to my collaborators, especially Mila Aldeco, Brian Dobosh, Vincent Giacalone, Kirsten Cottrill, Ahmad Mohammad, and Drs. Jocelyn Grunwell, Anne Fitzpatrick, Susan Stephenson, Rabin Tirouvanziam, and Octavian Ioachimescu. I have been very lucky to receive incredible support, guidance and scientific insights from these and countless other fantastic people. All of you had my best interest in mind and selflessly gave your time, energy and efforts to making me a better scientist and person. Although I can never repay you, I will always pay it forward.

TABLE OF CONTENTS

ACKNOWLEDGEMENTS	IV
LIST OF TABLES	VIII
LIST OF FIGURES	IX
LIST OF SYMBOLS AND ABBREVIATIONS	X
SUMMARY	XIII
CHAPTER 1. INTRODUCTION AND LITERATURE REVIEW	1
1.1 Introduction	1
1.1.1 Pulmonary anatomy	1
1.1.2 Small airway pathophysiology	2
1.1.3 Established methods of studying small airway disease	3
1.2 Modeling pulmonary physiology <i>in vitro</i>	5
1.2.1 Traditional Models	5
1.2.2 Modelling lungs in microphysiological systems	7
1.2.3 Mechanical forces in the distal lungs	8
1.3 Capturing Mechanical Forces in MPS	9
1.3.1 Limitations of mechanical force MPS	14
1.4 Capturing Inflammation in MPS	15
1.4.1 Immune cell infiltration in the small airways	15
1.4.2 Challenges of modelling inflammation in MPS	18
1.5 Challenges of Modeling the Lungs in MPS	20
1.5.1 Complexity	20
1.5.2 Heterogeneity	22
1.5.3 Data collection in microfluidic systems	23
1.5.4 Clinical relevance	23
1.6 Outlook	24
CHAPTER 2. OBJECTIVE OF THIS THESIS	25
CHAPTER 3. MICROFLUIDIC MODEL OF PULMONARY EDEMA IN THE DISTAL AIRWAYS	27
3.1 Introduction	27
3.2 Materials and Methods	29
3.2.1 Microfluidic device fabrication	29
Cell Culture	30
3.2.2 Plug generation	31
3.2.3 Cell counting and statistics	32
3.3 Results	32
3.3.1 Device design and fabrication	32
3.3.2 Plug generator	36
3.3.3 Liquid plug cell injury	37

3.3.4	Effect of liquid viscosity on plug propagation	38
3.4	Discussion	40
CHAPTER 4. A HIGH-THROUGHPUT DISTAL LUNG AIR-BLOOD BARRIER MODEL ENABLED BY DENSITY-DRIVEN UNDERSIDE EPITHELIUM SEEDING		42
4.1	Introduction	43
4.2	Methods	46
4.2.1	NCI-H441 maintenance in T-75 flasks	46
4.2.2	HUVEC maintenance in T-75 flasks	46
4.2.3	Lentiviral transduction	47
4.2.4	Trans-epithelial electrical resistance (TEER)	48
4.2.5	Staining and imaging	49
4.2.6	Histology	50
4.2.7	Permeability assays	50
4.2.8	Viral exposure	51
4.2.9	Cytokine quantitation	51
4.2.10	96-well Transwell upright seeding and maintenance	52
4.2.11	Upright underside seeding	52
4.2.12	HUVEC seeding	53
4.2.13	ALI culture	53
4.2.14	Statistical analysis	53
4.3	Results	54
4.3.1	Density-driven, inversion-free underside seeding robustly generates a functional air-blood barrier in 96-well throughput	54
4.3.2	Bilayer co-culture exhibits polarization and differentiation of epithelial cells in co-culture with primary endothelium	57
4.3.3	Epithelial exposure to viral and bacterial mimics induces endothelial inflammation and barrier loss	62
4.3.4	Epithelial viral exposure induces dose-dependent inflammatory signals in epithelial-endothelial co-culture	63
4.3.5	Epithelial aerosol exposure induces dose-dependent ROS and IL-8 response	64
4.4	Discussion	66
CHAPTER 5. HIGH-THROUGHPUT DOSE-RESPONSE ANALYSIS OF DISTAL LUNG NEUTROPHIL INFILTRATION AND ACTIVATION		72
5.1	Introduction	72
5.2	Materials and Methods	76
5.2.1	Preparation of air-blood barrier array (ABBA)	76
5.2.2	Neutrophil transmigration assays	76
5.2.3	Flow cytometry	77
5.2.4	Statistical analysis	79
5.2.5	Cell culture	80
5.2.6	Transwell preparation	81
5.2.7	TEER measurement	83
5.3	Results and Discussion	84
5.3.1	Preparation of standardized ABBA array	84

5.3.2	Parameters for standardized transmigration in high-throughput	87
5.3.3	Dose-dependent neutrophil recruitment and activation	91
5.3.4	Capturing a disease-specific microenvironment and inflammatory responses	94
5.3.5	Dose-response comparison of immunomodulatory therapeutics baricitinib and dexamethasone	98
5.4	Discussion	106
CHAPTER 6. CONCLUSIONS AND FUTURE DIRECTIONS		107
6.1	Major challenges	107
6.1.1	Tracheal aspirate sample dilution effects and phenotypic validation	107
6.1.2	Challenge: Sources of variability in ABBA experiments	109
6.1.3	Functional assay outcomes	111
6.1.4	Epithelial and endothelial biological relevance	112
6.2	Novelty and Future Applications	112
6.2.1	Isolation of disease-relevant phenomena	112
6.2.2	Dose-response analysis of therapeutics and toxins	117
6.2.3	Patient-specific physiology and drug responses	119
6.2.4	Generalizability	122
6.3	Closing statement	123
REFERENCES		124

LIST OF TABLES

Table 1. Comparison of in vivo airway and microfluidic device	34
Table 2. Seeding success rate.....	60
Table 3. Summary of Previous Transmigration Assays.....	74
Table 4. Flow cytometry antibody list	78
Table 5. Effect of TEER and Edge Position on Migrated Cell Number.....	89
Table 6. Permeability of epithelial-endothelial bilayers post-transmigration.....	99

LIST OF FIGURES

Figure 1-1 Injury-inflammation-repair in lung disease.....	3
Figure 1-2. In vitro model design schematic	7
Figure 1-3. Physiologic mechanical forces in the bronchoalveolar region and their computational models	11
Figure 1-4. MPS models of mechanical force in lung disease.....	14
Figure 1-5. Models of pulmonary inflammation in vitro.....	18
Figure 1-6. In vitro models of the lung microenvironment could be applied to study fibroproliferative disease in ARDS.....	22
Figure 3-1. Process for fabrication of microfluidic small airway-on-a-chip	29
Figure 3-2 Small airway plug generator	35
Figure 3-3 Liquid plug generation in microfluidic device.....	36
Figure 3-4 Liquid plug propagation and viscosity effects	39
Figure 4-1. Automatable underside seeding enabled by density-driven flotation forms a robust monolayer of NCI-H441 cells in co-culture with a vascular endothelium.	45
Figure 4-2 GFP- H441s (green) and RFP- HUVECs (orange) in co-culture.....	57
Figure 4-3 NCI-H441 cells grow into the membrane pores to contact the endothelium..	59
Figure 4-4. Co-cultured NCI-H441 cells and HUVECs show polarization and differentiation under ALI culture with serum-free medium.	61
Figure 4-5. Epithelial-endothelial signal propagation and barrier loss.....	64
Figure 4-6. ROS and IL-8 production after SOA exposure.....	66
Figure 5-1 Gating strategy for neutrophil flow cytometry.....	79
Figure 5-2 Preparation of Transwell bilayer coculture for transmigration assays.....	83
Figure 5-3 Humidity chamber prevents evaporation-dependent edge effects	86
Figure 5-4 Edge effects due to temperature gradients.	86
Figure 5-5 Transmigration assay models neutrophilic inflammation.	90
Figure 5-6. Neutrophils from different donors consistently migrate dose-dependently to chemoattractants	93
Figure 5-7. Transmigration replicates CF-like neutrophil activation and air-blood barrier properties.....	97
Figure 5-8 Permeability vs. TEER after transmigration	99
Figure 5-9 Baricitinib vs. dexamethasone dose-response.....	105

LIST OF SYMBOLS AND ABBREVIATIONS

APTES	(3-Aminopropyl)triethoxysilane
2-D	2-dimensional
3-D	3-dimensional
DAPI	4',6-diamidino-2-phenylindole
ARDS	Acute respiratory distress syndrome
ABBA	Air-blood barrier array
ALI	Air-liquid interface
ASN	Airway supernatant
ASL	Airway surface liquid
ATCC	American type culture collection
ANOVA	Analysis of variance
Papp	Apparent permeability
BLT	Block lipid transport
BALF	Bronchoalveolar lavage
CO ₂	Carbon dioxide
cm	Centimeter
COPD	Chronic obstructive pulmonary disease
CD	Cluster of differentiation
CI	Confidence interval
CTRL	Control
CXCR	C-X-C chemokine receptor
CXCL	C-X-C ligand motif
CF	Cystic fibrosis
DNA	Deoxyribonucleic acid
DMSO	Dimethyl sulfoxide
EBSS	Earle's balanced salt solution
EGK	Endothelial growth kit
ELISA	Enzyme-linked immunosorbent assay
EDTA	Ethylenediaminetetraacetic acid
FACS	Fluorescence-activated cell sorting
g	Gram
GFP	Green fluorescent protein
HTS	High-throughput screening
HUVEC	Human umbilical vein endothelial cell
IL	Interleukin
ICAM	Intracellular adhesion molecule
JAK	Janus kinase
JAKinib	Janus kinase inhibitor
LTB ₄	Leukotriene B ₄
LPS	Lipopolysaccharide
L	Liter

MDCK	Madin-Darby canine kidney
IC50	Median inhibition concentration
m	Meter
μ	Micro
MPS	Microphysiological system
miRNA	MicroRNA
m (prefix)	Milli
M	Molar
MOI	Multiplicity of infection
n	Nano
NET	Neutrophil extracellular trap
fMLP	N-formyl-methionyl-leucyl-phenylalanine
ns	No significance
NHBE	Normal human bronchial epithelial
NF-κB	Nuclear factor kappa B
Ω	Ohms (voltage)
OCT	Optimal cutting temperature compound
O ₂	Oxygen
PFA	Paraformaldehyde
P/S	Penicillin/streptomycin
Pen/strep	Penicillin/streptomycin
PBS	Phosphate buffered saline
PAF	Platelet activating factor
PDMS	Polydimethylsiloxane
Poly(I:C)	Polyinosinic:polycytidylic acid
ROS	Reactive oxygen species
RFP	Red fluorescent protein
RNA	Ribonucleic acid
RPMI	Roswell park memorial institute
s	Second
STAT	Signal Transducer and Activator of Transcription
NaFL	Sodium fluorescein
SD	Standard deviation
TEER	Trans-epithelial electrical resistance
TGF	Tumor growth factor
TNF	Tumor necrosis factor
UV	Ultraviolet
VCAM	Vascular cell adhesion molecule
VCBM	Vascular cell basal medium
VE	Vascular endothelial
VEGF	Vascular endothelial growth factor
VILI	Ventilator-induced lung injury
v:v	Volume:volume

vWF	Von Willebrand Factor
w/v	Weight/volume
WT	Wild type
ZO	Zonula occludens

SUMMARY

The distal airways can become obstructed and limit lung function in many pulmonary diseases, both acute and chronic. This small airway dysfunction results from aberrant mechanical forces, inflammatory mediators, abnormal fluid properties, and other factors. However, studying these contributions to small airway disease is challenging. Existing methods, such as biopsy of human tissue, animal models, and 2D in vitro models cannot reflect the dynamic processes of fluid-mediated injury and inflammation in the small airways with adequate precision and control. Therefore, in this thesis we develop methods to model the small airways in vitro using microphysiological systems (MPS). MPS are complex cell culture models that capture functional aspects of the tissue in a human-cell based, controlled microenvironment. Here, we utilize microfluidic platforms and high-throughput culture systems to recreate phenomena that contribute to small airway injury. In Aim 1, we demonstrate that fluid-mediated injury results in small airway epithelial cell death. In Aim 2, we develop a high-throughput method for generation of small airway air-blood barrier mimetic microtissues that respond to viral exposure with epithelial-endothelial coordination. Finally, in Aim 3 we apply the air-blood barrier array (ABBA) to develop a standardized, high-throughput method for modeling and studying the infiltration of neutrophils into the epithelial lumen. we demonstrate the model's disease-mimetic capability and generate patient-specific dose-response curves for anti-inflammatory therapeutics. Overall, this thesis contributes substantially to the field of lung-mimetic microphysiological systems and demonstrates novel applications of such systems for the investigation of complex components of small airway dysfunction.

CHAPTER 1. INTRODUCTION AND LITERATURE REVIEW

Portions of this chapter are reproduced from “Viola, H. et al. Microphysiological systems modeling acute respiratory distress syndrome that capture mechanical force-induced injury-inflammation-repair. APL Bioeng. 3, 041503 (2019)”¹ with the permission of AIP Publishing.

1.1 Introduction

1.1.1 Pulmonary anatomy

The lungs perform gas exchange with circulating blood to maintain cellular respiration. Gas exchange is performed in the alveoli, a sponge-like network of sub-millimeter air sacs that create a surface area of over 50-100 square meters in the adult lungs². The alveoli are interspersed with capillaries that deliver oxygen-depleted blood for diffusive exchange of blood carbon dioxide and air oxygen. Alveo-capillary gas exchange tissue comprises about $\frac{3}{4}$ of the lung's total volume with the other $\frac{1}{4}$ occupied by gas conducting airways that efficiently move gas in and out of the lungs during respiration². The bronchioles, or small airways, are conduits smaller than 2 mm in diameter that comprise the last few generations of conducting airways before gas reaches the alveoli. The proximal bronchioles are ~2-0.5 mm diameter airways lined with a pseudostratified epithelium containing mucus-producing goblet cells, ciliated cells, secretory and basal cells³. The more distal terminal bronchioles are approximately 0.2-0.2 mm diameter airways and transition to primarily exocrine, dome-shaped, monolayered club cells. In this region, air transport transitions from laminar bulk flow to diffusion^{2,4}. The respiratory

bronchioles are the smallest and most distal airways that are interspersed with alveoli. In these airways and in the alveoli, air moves only by diffusion.

1.1.2 Small airway pathophysiology

The small airways can become resistant to air flow due to disease processes such as inflammation, airway constriction, transient or permanent obstruction, airway or lobe collapse, or fibrosis⁵. Resultantly, the affected lungs become less efficient at exchanging oxygen and carbon dioxide, leading to systemic negative health effects^{3,5}. This phenomenon, termed small airway dysfunction, has been documented in a number of lung diseases including chronic obstructive pulmonary disease (COPD)⁶, cystic fibrosis (CF)^{7,8}, acute respiratory distress syndrome (ARDS)^{1,9}, bronchiolitis obliterans (BOOP)¹⁰, particulate exposure^{3,11}, asthma¹², and many others, especially primary bronchiolar disorders⁵.

Therefore, physicians and researchers are interested in studying the cellular and molecular pathophysiology of small airway dysfunction so that effective treatments can be developed. Investigations so far have led to tremendous advances in understanding disease processes in the small airways. These investigations have shown that common features of diseased small airways across etiologies include abnormal fluid properties (volume, viscosity, composition), immune cell infiltration, epithelial injury, and airway tissue remodeling⁵. The involved mediators of injury, inflammation and remodeling are disease-specific, though the overall features are similar. Further advances are required because therapeutics are not yet available to curb small airway dysfunction.

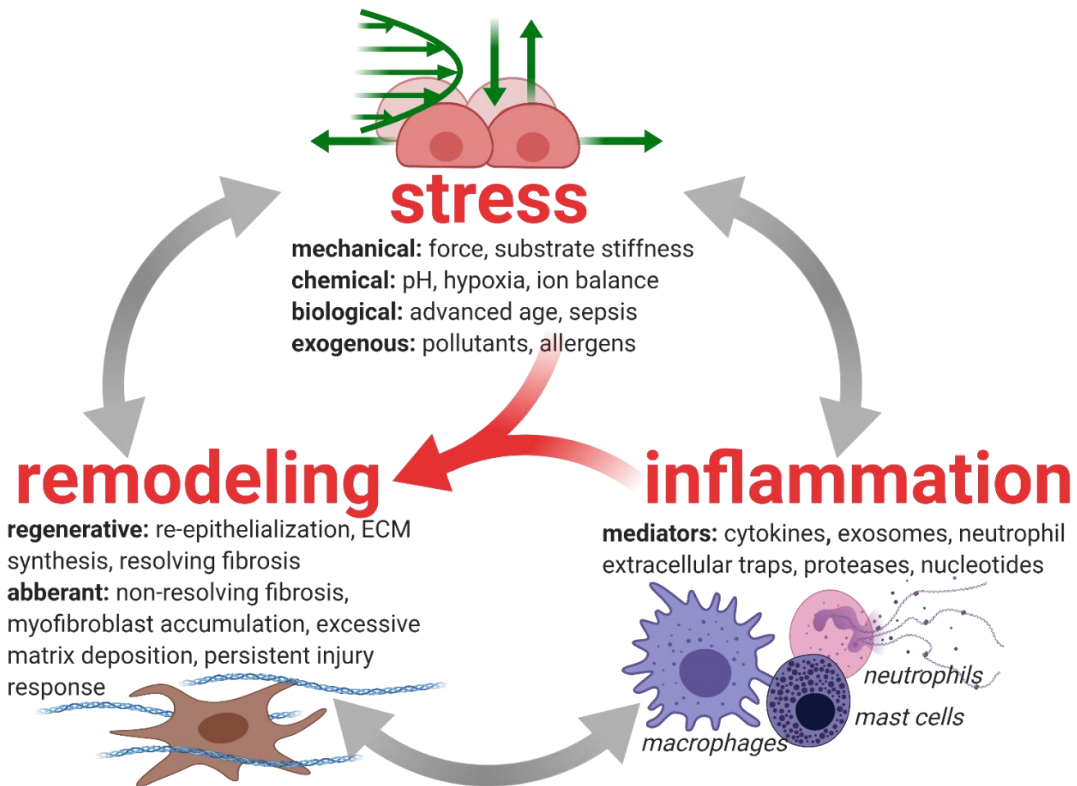


Figure 1-1 Injury-inflammation-repair in lung disease

Inflammation and fibrosis (resolving or non-resolving) cooperate to remodel tissue after injury^{13,14}. Both processes are heavily influenced by stressors in the tissue microenvironment. In various diseases, mechanical forces arising from surfactant dysfunction¹⁵, mechanical ventilation¹⁶, mucus dysfunction^{17,18}, or other stressors interfere with the tissue repair process by re-injuring the tissue, thereby inducing inflammation¹⁹ and promoting fibrosis^{20,21}. The interactions between tissue stress, inflammation and remodeling can direct the tissue towards successful tissue repair or towards aberrant remodeling that consists of progressive fibrosis and systemically dysregulated immunity.

1.1.3 Established methods of studying small airway disease

Unfortunately, the small airways are difficult to access directly in living human patients. Biopsies present patient risk and are rarely performed in routine clinical care. Therefore lung tissues are routinely obtained from deceased patients, biasing pathology

studies towards severe disease. Additionally, pathology studies cannot characterize the entire organ and lack information on the composition of the soluble mediators in the airway and capillary microenvironment.

The distal airway lumen can instead be sampled in human patients using bronchoalveolar lavage, wherein the deep lungs are rinsed with a saline solution²². The saline rinse collects liquid and debris from the surface of the epithelium in the small airways and alveoli, allowing characterization of the cellular and molecular components present during disease. BALF studies have yielded tremendous insights into the pathophysiology of disease in the distal lungs²²⁻²⁵. However, they do not provide temporal or spatial information: that is, the arrangement of cells and tissues in space and the ways in which that arrangement evolves over time. Additionally, BALF is diluted with an impossible-to-quantify volume of saline, making quantitative comparison between different BALF samples unreliable, even across the same patient over time^{22,26-30}.

Various animal models have also been established to study small airway disease. Mice lack the respiratory bronchioles that comprise a crucial portion of the small airways in humans³¹. Therefore larger mammals such as rats³², minipigs³³, sheep³⁴ are employed to investigate the small airways, with increased associated expenses. In animal models, pathology sections can be obtained at any stage of disease, and whole-organ dissociation followed by genomic analysis or flow cytometry can provide information about the cellular composition of the organ. BALF can be collected like in human lungs²⁶. However, most of the same limitations to pathology and BALF apply in animals, and new constraints are introduced. Species-specific differences in gene expression, molecular mechanisms, and cell functions present a barrier to human translation^{35,36}. Animal models at present do not

capture the clinically observed variation in disease presentation, termed subphenotypes, nor the individual patient-specific differences in disease progression and tissue microenvironment^{1,37,38}.

1.2 Modeling pulmonary physiology *in vitro*

1.2.1 Traditional Models

To understand the biological mechanisms that drive pulmonary disease, preclinical models are essential. The ideal preclinical model of pulmonary pathophysiology should recapitulate only the critical aspects of the complex disease microenvironment, focusing on a specific disease and its pathophysiologic features. Current models are limited in their ability to represent human pathophysiology for the study of disease and drug mechanisms.

2-D monoculture of the airway epithelium *in vitro* cannot capture intricacies of inflammatory networks and crosstalk between processes of injury, inflammation and remodeling. This culture method typically also neglects tissue-level stresses such as mechanical force and does not account for fluid stresses that are dominant in many lung diseases due to surfactant depletion, bronchoconstriction, pulmonary edema, and other causes. Finally, cell lines are limited in their relevance to pathophysiology. However, primary human cells are becoming more accessible. For example, the Marisco Lung Institute's CF Center Tissue Procurement and Cell Culture Core has pioneered isolation and culture techniques for primary human lung cells³⁹.

Animal models, notably mouse models, capture complex interactions between injury, inflammation and tissue repair in the lungs. However, species-specific differences in lung physiology and molecular pathophysiology could interfere with attempts to test therapeutics and investigate disease mechanisms. There is conflicting evidence regarding whether murine gene expression profiles in response to lung injury correlate well with those in humans. Sweeney et al. argue for significant similarity between murine and human inflammation after lung injury⁴⁰, although limitations to this study include the small human sample size (n=3) and the number of genes evaluated (n=432). Seok et al., in contrast, assert that when comparing almost 5,000 human and murine genes altered by the same inflammatory stressors (i.e., burn, trauma, hypoxemia), mouse models of inflammation show a close to random (R^2 between 0-0.1) association to human gene counterparts⁴¹. However, a comprehensive determination has not been reached about the relevance of murine gene expression to human disease. Therefore, there is interest in studying human specimens to complement animal studies.

Inherent limitations hinder the study of primary human specimens. It is impossible to control the cell types (e.g., immune cells, epithelium, fibroblasts) and mediators (e.g., cytokines, chemokines, extracellular matrix components) present in a patient's lung microenvironment, limiting the ability to interrogate individual components' contribution to pathophysiology. This limitation can result in studies that are descriptive rather than mechanistic. Biopsy samples are acquired primarily from deceased patients because biopsies are a high-risk procedure for living patients. Because of this, human lung samples are biased towards severe disease and provide little opportunity to study the evolution of the disease microenvironment from early to late stage. Bronchoalveolar lavage fluid

(BALF) provides a snapshot of the distal lung's cytokine, immune cell, and mucus content, but cellular-level mechanisms cannot be positively inferred without corroborating *in vitro* data. Overall, human samples are a vital component of lung pathophysiology research but corresponding *in vitro* data from more sophisticated models is needed to study specific mechanisms.

1.2.2 Modelling lungs in microphysiological systems

Microphysiological systems (MPS) are advanced *in vitro* culture platforms that mimic human tissue-level function and microenvironment by incorporating factors such as co-culture, three-dimensional geometry, cell migration, and mechanical cues^{1,42}. MPS therefore bridge the gap between animal models and human pathophysiology, providing a third paradigm for the study of complex disease processes and drug mechanisms.

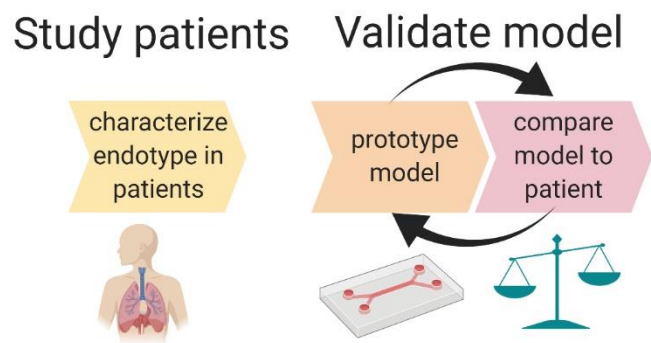


Figure 1-2. *In vitro* model design schematic

Iterative adjustments to model parameters, such as genetics (e.g., MUC5A over-expressing epithelium), physical forces, degree of initial injury, degree of fibrosis, and the type and ratio of inflammatory mediators, could enable the development of a model that produces biomarkers or functional characteristics (e.g., response to therapeutics, response

to mechanical strain, immune cell phenotype changes such as enhanced NETosis), mimicking those of a specific disease. The model should also be validated by testing functional outputs such as barrier function of the epithelium, and tissue healing. The final model provides the opportunity for pathophysiological mechanisms of disease to be clarified and for drug candidates to be tested *in vitro*. Both pathophysiology and drug testing will help predict whether a certain disease is likely to respond to novel treatments.

Of course, the challenge of recreating a pathophysiology that is poorly understood, for the purpose of advancing its understanding, cannot be overstated. MPS are uniquely suited to undergo iterative prototyping until a desired pathophysiological feature is adequately captured. This strategy is illustrated in **Figure 2-1**. MPS designers compare their prototype to the human phenotype using metrics such as biomarkers, immune cell phenotypes, and responses to stimuli (e.g., strain, hypoxia, infection). The prototype is then adjusted to better reflect *in vivo* metrics through the precise control of microenvironmental factors such as cell types, inflammatory and fibrotic mediators, and type/degree of mechanical force. MPS capture disease processes to the extent necessary to produce specific outcomes but remain simple enough to obtain a high signal-to-noise ratio, which is a desirable feature of *in vitro* models.

This work aimed to construct microphysiological systems that replicate pulmonary physiology and pathophysiology. we focus on mechanical forces and inflammation because they are central to pulmonary pathophysiology, difficult to capture *in vitro* with traditional methods, and readily adaptable to existing MPS technology.

1.2.3 Mechanical forces in the distal lungs

Small airway disease is associated with airway closure or obstruction. In some cases, this is caused by excess fluid, surfactant dysfunction, or hyperviscous fluid in the distal airways. All of these can lead to repeated airway closure and reopening that damages the small airways. Experimental and computational models have shown that large mechanical forces are imparted on the airway epithelium due to this stress and that these forces lead to epithelial injury (**Figure 2-2**).

1.3 Capturing Mechanical Forces in MPS

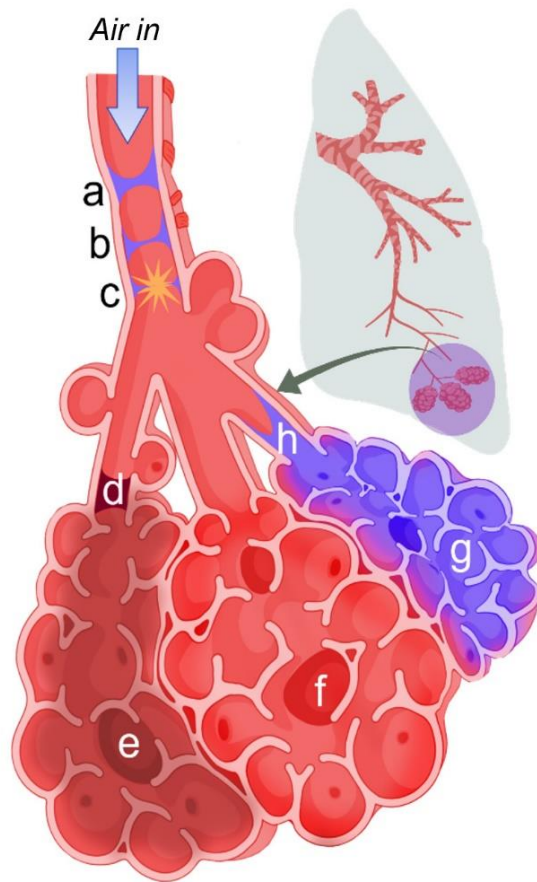
Lung mechanical forces can be categorized broadly as compressive stress, shear stress, and stretch (**Figure 2-2(B)**)⁴³. **Shear stress** is the force per area that acts parallel to a plane; often considered a “slipping” force. **Strain** (stretch) is the change in length of a plane divided by the initial length. **Compressive stress** is the force per area applied perpendicular to a plane; it includes pressure and normal force. The effects of mechanical forces on pulmonary epithelia have been studied *in vitro* for several decades^{44,45}. Most models incorporate membranes that allow for strain or compressive stress to be applied to well-differentiated cell lines or primary airway cells in air-liquid interface (ALI) culture.

Complex fluid stresses also contribute significantly to lung injury^{16,46-48}. Investigators have modeled the fluid stresses imparted by liquid plug propagation and rupture, small airway collapse and reopening, and alveolar collapse and reopening. The Gaver group was first to report an *in vitro* system for modeling the stress field associated with alveolar recruitment using a moving air bubble (**Figure 2-2(D)**)^{49,50}. They showed that slower bubble speeds increase cell death, despite a milder shear gradient, because the

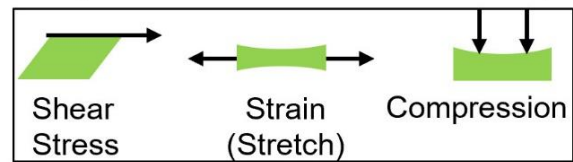
pressure gradient is significantly increased⁵¹. In the same moving air bubble model, Higuera-Castro et al. showed that increasing the substrate stiffness caused greater cell death after 1 and 5 bubbles⁵² (**Figure 2-3(C)**).

Additionally, Takayama and colleagues modeled liquid plug propagation and rupture in vitro^{53,54} (**Figure 2-3(A)**)^{53,55,56}. They found that liquid plug propagation caused cell death even without plug rupture. To explain this observation, Fujioka, Grotberg et al. showed that the front meniscus of a moving liquid plug imparts large stresses on the airway wall due to a narrow capillary wave that appears ahead of the plug's leading edge (**Figure 2-2(C)**, capillary wave circled)^{55,56}. Recently, Muradoglu, Grotberg et al. also showed that surfactant reduces the mechanical stress imparted by the liquid plug⁵⁷. In an alveolar closure/reopening model, Douville, Takayama et al. showed that repeat strain combined with fluid stress caused cell death and detachment, suggesting a mechanism for how atelectasis affects lung function⁵⁸ (**Figure 2-3(B)**). The work of the preceding investigators has brought attention to the major role of fluid stresses in promoting lung injury.

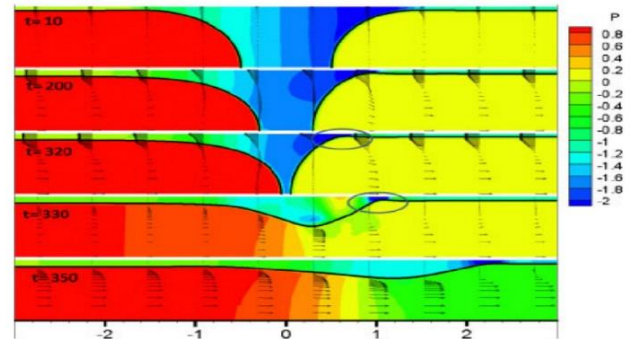
A. Excess fluid and mechanical ventilation exert mechanical force on the distal airways



B. Components of the stress field in air-liquid flow



C. Hassan et al. modeled pressure contours of liquid plug propagation and rupture



D. Bilek et al. and Yalcin et al. quantified the stress field of a propagating air bubble

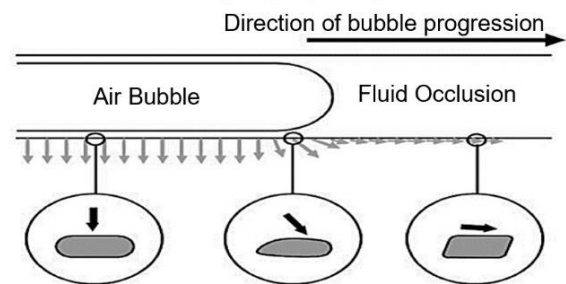
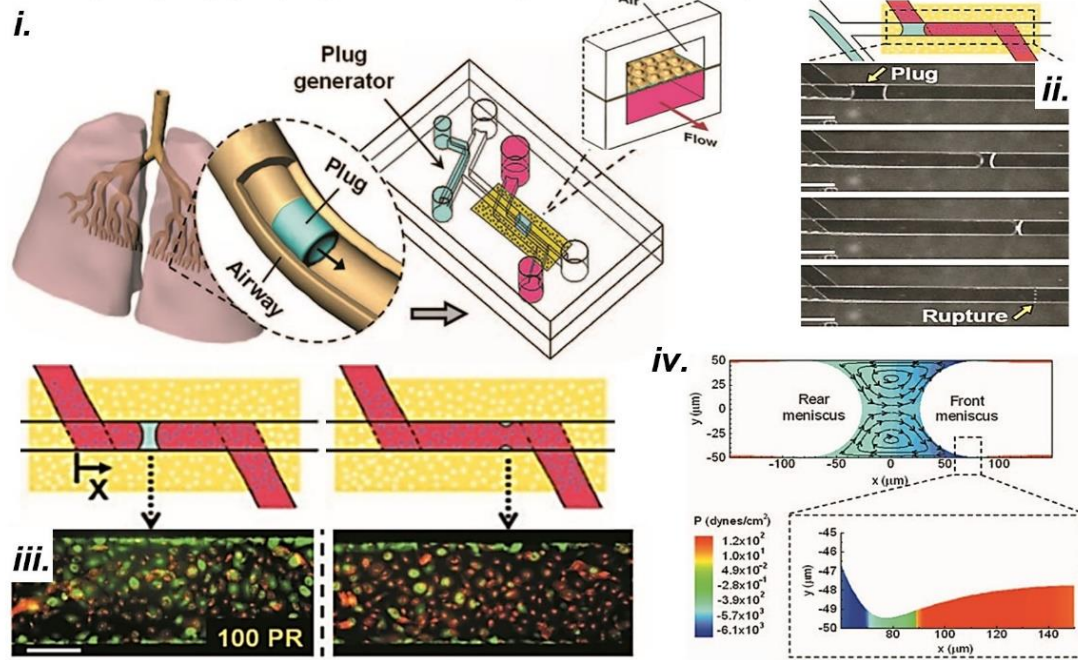


Figure 1-3. Physiologic mechanical forces in the bronchoalveolar region and their computational models

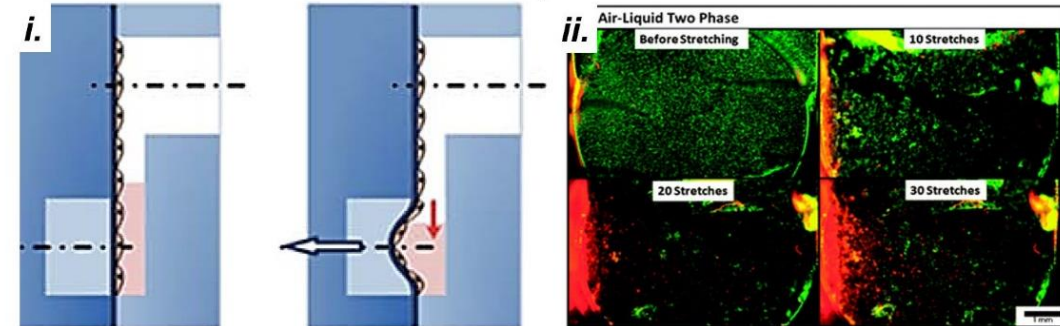
A. The acinus is a group of alveoli sharing a common terminal bronchiole (**d** or **h**); acini **e**, **f**, and **g** are depicted in this figure. Acinus **e** is cut off from air flow by the stagnant plug at **d**; acinus **f** is overinflated, and acinus **g** is flooded with proteinaceous fluid. **B.** Shear, strain, and compression are the main components of force present in the lungs, either independently or in concert. In the above depiction, strain results from overinflation of acinus (**f**) due to obstruction of acinus (**d**) and collapse of acinus (**g**). Compression of adjacent acini results from the overinflation of (**f**). Shear stress is a component of the stress field produced during airway reopening at (**h**)^{49,50}. **Interfacial flow** damages the small airways when liquid plugs propagate and rupture during inspiration^{53,54} (**a-c**). Transient liquid plugs form when the small airways collapse slightly and liquid on either side of the airways meets, forming the plug depicted in **a**. Upon inspiration, the plug is pushed by pressure-driven flow, becoming thinner and thinner (**b**) until it loses integrity and pops (**c**), creating the crackle sounds that are observed upon auscultation of the lungs. **C.** Hassan et al.⁵⁶ modeled liquid plug propagation and rupture and found that the leading edge of the

*plug creates a narrow capillary wave (circled). The wave's extreme pressure gradient imparts severe stress on the airway wall. D. The first in vitro model of airway reopening was introduced by Bilek et al.⁴⁹. Using this model, Yalcin et al. found that smaller airway diameters experience greater stress⁵⁰. C. Reproduced with permission from E.A. Hassan, E. Uzgoren, H. Fujioka, J.B. Grotberg, and W. Shyy, *Int. J. Numer. Methods Fluids* **67**, 1373 (2011). Copyright 2011, John Wiley and Sons. D. Reproduced with permission from A.M. Bilek, K.C. Dee, and D.P. Gaver, *J. Appl. Physiol.* **94**, 770 (2003). Copyright 2003, American Physiological Society*

A. Liquid plug propagation and rupture causes epithelial death



B. Fluid stress and strain causes epithelial death and detachment



C. Fluid meniscus mimicking atelectasis causes cell death, detachment

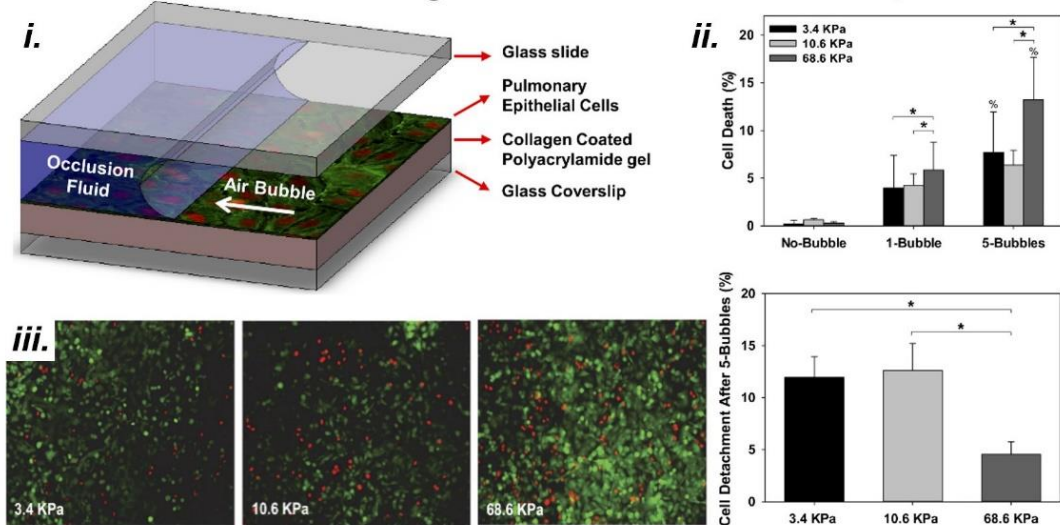


Figure 1-4. MPS models of mechanical force in lung disease

(A)(i) A microfluidic device replicates the generation of crackle sounds frequently heard in the distal airways of patients with pulmonary edema. (ii) The device generates liquid plugs that propagate and rupture in channels over alveolar type I pneumocytes. (iii) Plugs result in epithelial cell death (red) during propagation (left) and especially at the rupture site (right). Scale bar, 150 μ M. (iv) Fluid dynamic simulations show that the leading edge of the plug applies severe shear stress to the epithelium^{55,56}. Reproduced with permission from PNAS 104.48, 18886-18891 (2007). Copyright 2007 National Academy of Sciences⁵³. (B)(i) Douville *et. al* report a device that applies simultaneous fluid shear stress and mechanical strain to alveolar epithelium; vacuum stretches the membrane and simultaneously lowers the fluid level. (ii) Fluid stress and strain result in death (red cells) and detachment of alveolar epithelium in the device. Scale bar, 1 mm. Reproduced with permission from **Lab Chip**, **11**, 609-619 (2011). Copyright 2011, Royal Society of Chemistry⁵⁸. (C)(i) Higueta-Castro *et al.* mimic small airway or alveolar reopening by propagating an air bubble over the epithelium⁵². The device design, first conceived by Bilek *et al.*⁴⁹, has been extensively used to characterize the damage of liquid stress during atelectasis and airway reopening^{50-52,59,60}. (ii-iii) Higueta-Castro *et al.* show that the fluid meniscus causes increasing cell death and detachment with increasing substrate stiffness. Reproduced with permission from N. Higueta-Castro, C. Mihai, D.J. Hansford, and S.N. Ghadiali, *J. Appl. Physiol.* 117, 1231 (2014). Copyright 2014 American Physiological Society.

1.3.1 Limitations of mechanical force MPS

Few pulmonary force models consider the physical properties of the extracellular matrix, such as stiffness and substrate ligands. It is well established that substrate ligands affect epithelial and endothelial properties and that focal adhesions mediate mechanosensing^{61,62}. Of relevance to mechanical force models, aligned collagen fibers in the substrate amplify cell-cell mechanotransduction across distances greater than several cell diameters⁶³. In the moving air-finger model (**Figure 2-3(C)**)^{49-52,59,60}, Higueta-Castro *et al.* showed that increased substrate compliance leads to greater cell detachment and less necrosis⁵². More investigation is needed to determine the effects of substrate properties on physiology in mechanical force models.

Mechanical force models rarely contain multiple stress types, despite indications that stressors work synergistically to promote injury. For example, simultaneous surfactant loss and overstretching of the alveoli cooperatively promote secondary lung injury during mechanical ventilation^{64,65}. Even models that do capture complex force combinations or stress fields often fall short of describing the force's downstream effects on the tissue. Huh et al. and Douville et al., shown in **Figure 2-3(A-B)**, capture complex forces but characterize only cell death and detachment. Ghadiali and colleagues, in contrast, have characterized mechanotransduction in the moving air-finger model (**Figure 2-3(C)**)^{52,59,60}. Still, both models lack immune and fibroblast coculture.

1.4 Capturing Inflammation in MPS

1.4.1 Immune cell infiltration in the small airways

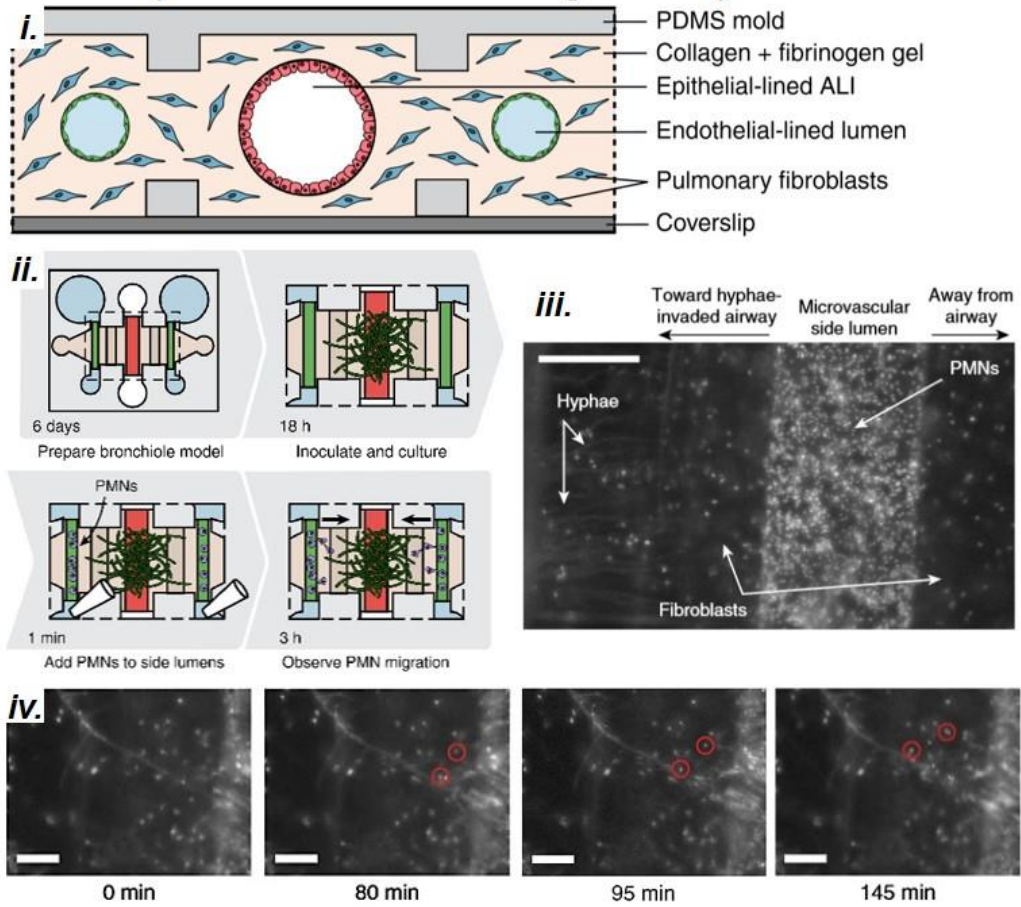
In addition to mechanical force, infiltration of immune cells significantly contributes to small airway disease. The characteristics of pulmonary inflammation in the distal lungs depends on the disease in question. Inflammation can be acute or chronic; concentrated into granulomatous lesions or dispersed diffusely amongst the tissue; and composed of different immune cell subsets depending on the disease, timing, and particular region of the distal lung under consideration^{66,67}. Further, both innate and adaptive arms of the immune system can contribute to the inflammatory milieu.

Nevertheless, the first cells to migrate into a new site of infection or injury are likely to be neutrophils. These innate immune cells form the second line of defense after tissue-resident macrophages. Upon arrival, they upregulate phagocytosis to clear debris and

pathogens. They release pre-packaged granules containing pro-inflammatory cytokines, chemokines, and antimicrobial enzymes like neutrophil elastase and matrix metalloproteases. They also interact with epithelial cells, endothelial cells, and macrophages that are already present in the microenvironment.

Although not the only cells responsible for inflammation, neutrophils comprise the majority of inflammatory cells in the distal lungs of patients with ARDS⁶⁸, COPD⁶⁹, neutrophilic asthma⁷⁰, bronchiolitis obliterans⁷¹, viral lower respiratory infection⁷², and other lung diseases⁷³. Therefore, much attention has been paid to studying and modelling neutrophilic inflammation.

A. Neutrophils chemotax towards fungi on a chip



B. Neutrophil transmigrates and phagocytoses E. coli on a chip

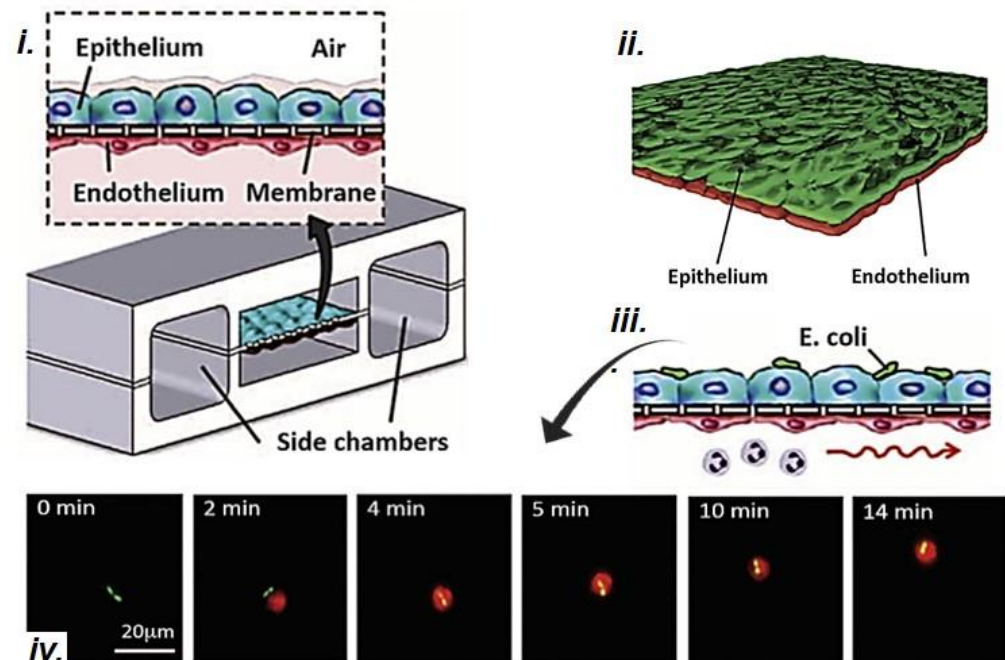


Figure 1-5. Models of pulmonary inflammation *in vitro*

(A)(i) A microfluidic small airway-on-a-chip replicates the endothelium, interstitial fibroblasts, and epithelium. (ii) Fungal infection is simulated by inoculating the epithelium with WT *Aspergillus fumigatus*, a model fungal pathogen. (iii) Neutrophils are added to the endothelial channels after the hyphae have extended into the interstitial space. Scale bar, 200 μM . (iv) Neutrophils chemotax from the endothelium through the interstitium towards fungal hyphae, attracted by volatile compounds produced by the fungus. Scale bars, 100 μM . Reproduced with permission from *Nat. Com.*, 8 (2017)⁷⁴ under CC BY 4.0 (<https://creativecommons.org/licenses/by/4.0/>). (B)(i-ii) A microfluidic alveolus-on-a-chip incorporates strain and neutrophil transmigration in a bilayer epithelium-endothelium coculture model. (iii) *E. coli* on the epithelium attracts neutrophils to transmigrate from the basal channel through endothelium and epithelium. (iv) Two *e. coli* bacteria (green) on the epithelium are chased and phagocytosed by a neutrophil (red) on the epithelium of the device. From D. Huh, B.D. Matthews, A. Mammoto, M. Montoya-Zavala, H.Y. Hsin, and D.E. Ingber, *Science* 328, 1662 (2010). Reprinted with permission from AAAS⁷⁵.

1.4.2 Challenges of modelling inflammation in MPS

The choice of cell types, source, and degree of activation or polarization can greatly affect cell phenotype and responses to stimuli. Tissue repair *in vivo* involves the migration, activation, and cross-contact of multiple cell types including fibroblasts, neutrophils, monocytes, and lymphocytes. The ideal model would capture a high degree of *in vivo* cell functionality including fibroblast proliferation, immune transmigration and *in situ* activation, degranulation, NETosis, and elevated phagocytosis. However, many of these behaviors are difficult to control and modulate in complex model systems with multiple cell types. For example, TGF- β activates fibroblasts but may have concurrent effects on the epithelium and immune cells. MPS should capture the minimal activation necessary to recapitulate the disease mechanism of interest.

Barkal et al., for example, focused on neutrophil activation in their small airway-on-a-chip model of fungal infection. Neutrophils migrated towards volatile fungal

chemoattractants through the endothelium and epithelium (**Figure 2-4(A)**)⁷⁴. In a model of invasive aspergillosis, the device recapitulated the well-characterized inflammatory cytokine response and increased recruitment of neutrophils observed in murine and zebrafish models. In another example, Choe et al. focused on activation of fibroblasts⁷⁶. They applied strain to a co-culture of human bronchial epithelial cells atop a fibroblast-seeded collagen gel. They found that strain induced myofibroblast differentiation and type III & IV collagen deposition. Both myofibroblasts and type III collagen were concentrated close to the basal side of the epithelium, suggesting that the epithelium is a source of profibrotic mediators that promote matrix remodeling. Their *in vitro* model included the minimum cell types and activating stimuli to capture remodeling events. Furthermore, the model showed that the pathway is not mediated by immune cells, because they are not present. Rational choice of the required cell types and activating stimuli enables MPS to remain simple enough for analysis but sophisticated enough to capture inflammation and remodeling *in vitro*.

Immune cell and fibroblast cocultures greatly improve the physiological relevance of ARDS MPS but present significant design challenges. First, very few MPS have studied the impact of mechanical strain on fibrosis. Swartz²⁰ and Choe⁷⁶ showed that strain-induced fibrosis can be mediated by the epithelium, but such mechanical force pathways that induce fibrosis are likely complex and multifactorial. As such, they should be further explored in MPS that can incorporate physiological forces in co-culture systems. Additionally, the presence of multiple cell types obfuscates the source of inflammatory and fibrotic mediators (e.g., cytokines, proteases, miRNA, reactive oxygen species, TGF- β). To overcome this hurdle, MPS data is sometimes analyzed with systems biology techniques

similar to those used to parse out *in vivo* signaling pathways^{77,78}.

Additionally, airway epithelia, especially from primary cells, require many days to weeks to polarize. Media optimization may not be adequate to maintain the health and desired phenotype of all cell types present in co-culture in the long term. Sellgren et al. reported a triple co-culture of primary airway epithelium, fibroblasts and endothelium and noted that an airway-like phenotype (cobblestone morphology, mucus production and cilia) was difficult to maintain in coculture conditions⁷⁹. MPS designers should consider if long-term co-culture can be avoided, and if not, what media formulations can maintain co-cultured cells in their desired phenotypes.

Substrate properties and mechanical forces also affect immune and fibroblast cell phenotypes. MPS should have physiologically relevant physical forces and substrate properties so that immune and fibroblast phenotype mimic those *in vivo*. While models have independently considered immune cell and fibroblast mechanobiology in response to single stresses such as substrate stiffness or mechanical force, few combine multiple stress types in the same microenvironment. Although Huh et al. 2010 (**Figure 2-4(B)**) incorporated interstitial flow, strain and transmigration into their alveolus on-a-chip, they did not study how these forces affected the neutrophils in the model.

1.5 Challenges of Modeling the Lungs in MPS

1.5.1 Complexity

A major challenge of designing MPS is determining the level of model complexity. An overly complex model will produce noisy data, but an overly simplistic one is not useful. One option is to utilize functional readouts that are already familiar to the biology community, such as phenotypic assays (e.g., assays for bacterial phagocytosis and killing by neutrophils), to reduce the dimensionality of the data while keeping the model relatively complex. MPS are, however, limited in how complex they can become before losing physiological relevance. A model that is too complicated could create conditions that induce non-physiological cell behaviors. Additionally, elaborate models are difficult to fabricate which limits their throughput and accessibility to the greater research community. Designers must consider what aspect of pathophysiology they desire to model and carefully consider what features are necessary to capture the phenomenon while minimizing the components of the system.

Pulmonary pathophysiology is complex and involves multiple stages with different characteristics. The designer must consider how much disease progression they will model. For example, Huh et al. captured pulmonary edema, fibrin deposition and impaired gas exchange in response to toxic levels of IL-2 in a lung-on-a-chip microdevice including only the epithelium and endothelium (**Figure 2-5**). They discovered that immune cells and fibroblasts were not necessary to produce these tissue-level functions, but strain was necessary, indicating that strain a significant initiator of early pulmonary drug toxicity responses *in vivo*.

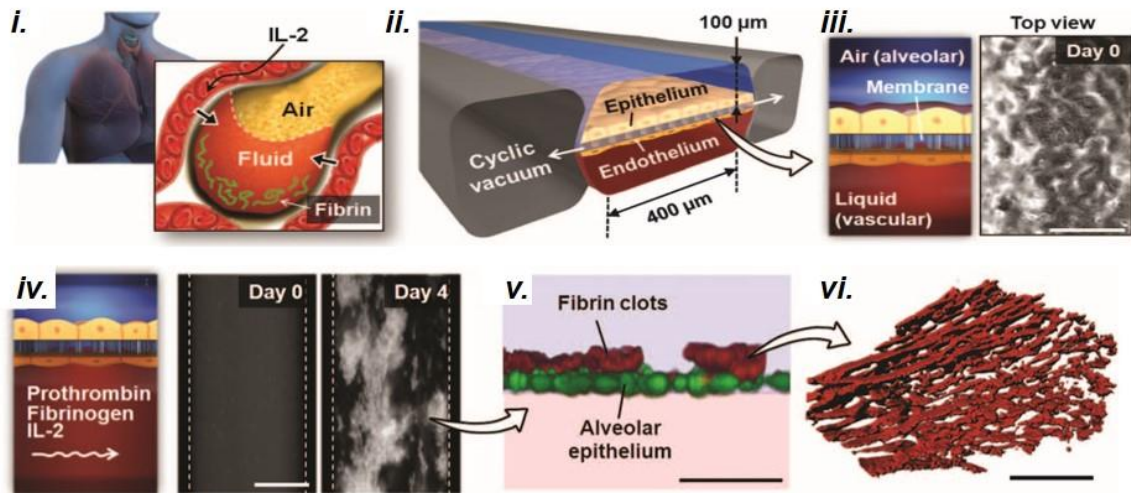


Figure 1-6. *In vitro* models of the lung microenvironment could be applied to study fibroproliferative disease in ARDS

(i) A lung-on-a-chip that replicates vascular leakage leading to pulmonary edema and fibrin clotting⁷⁵. (ii) Strain is applied, by pulling vacuum on either side of the chamber, to a membrane (iii) with alveolar epithelium on the apical side and endothelium on the basal side. Scale bar, 200 μ M. (iv) IL-2 induces endothelial and epithelial permeability allowing basal media loaded with prothrombin and fibrin to pass through the membrane and flood the apical channel, simulating pulmonary edema. Scale bar, 200 μ M. (v-vi) Fibrin clots form on the apical channel after it becomes flooded with basal media containing fibrin and prothrombin. Scale bar (v), 50 μ M. Scale bar (vi), 5 μ M. From D. Huh, D.C. Leslie, B.D. Matthews, J.P. Fraser, S. Jurek, G.A. Hamilton, K.S. Thorneloe, M.A. McAlexander, and D.E. Ingber, *Sci. Transl. Med.* 4, 159ra147 (2012). Reprinted with permission from AAAS.

Conversely, designers must consider whether even the most complex MPS is comprehensive enough to replicate the phenomenon of interest. For example, a single MPS could not capture multiple organ failure. Systemic dysregulated immunity that is observed in sepsis is likewise unlikely to be captured in a single MPS. Many MPS also lack an immune component, a challenge that has not been addressed sufficiently. However, the simplicity MPS compared to *in vivo* models is often a benefit because it allows the isolation of confounding factors from the system, such as in Choe⁷⁶ and Huh⁷⁵.

1.5.2 Heterogeneity

Primary human cell heterogeneity is also a significant challenge. Quality control of primary-cell-sourced cultures is difficult, especially in microfluidic culture with very small cell populations, due to variability across patients and even among cells from a single source. Conversely, models constructed with cell lines typically lack adequate cell heterogeneity. For example, models of the small airways that use the H441 club cell line lack the small populations of goblet cells, basal cells, and macrophages also present in this microenvironment. Most MPS mimicking the alveoli only include alveolar type I pneumocytes and neglect type II pneumocytes, macrophages, and fibroblasts. Mertz et al.⁸⁰ provides a discussion of the considerations of cell heterogeneity in MPS.

1.5.3 Data collection in microfluidic systems

Traditional assays are difficult to adapt to microfluidic MPS. Epithelial barrier permeability is usually absent from microfluidic devices, especially real time permeability⁸¹. This measure of epithelial response to stress and recovery from injury would greatly increase the information provided by microfluidic MPS. The scratch wound assay is a common metric of epithelial repair and recovery from injury that has only been adapted to microfluidics by Felder et al.^{82,83} in a custom device. Cytokine levels produced by very small cell numbers could fall below the detection limit of Luminex or ELISA assays. The MPS designer who considers microfluidics should determine whether their study will be sensitive to these limitations.

1.5.4 Clinical relevance

Finally, for MPS to move from proof-of-concept to clinical application, close cooperation with clinicians and the medical research community is essential. Clinicians

connect researchers with urgent medical needs of patients and help researchers design their models in the context of a specific motivating question. Researchers in disease-specific fields provide essential information from studies of primary samples and basic science experiments that direct the design of more complex systems. An accurate model will be validated against clinical data and will recapitulate relevant aspects of disease-specific pathophysiology or treatment.

1.6 Outlook

Despite the challenges of using MPS for lung research, opportunities abound. Such models could elucidate mechanisms that drive tissue repair towards regenerative or maladaptive responses to injury. Additionally, MPS can be applied to study pulmonary drug delivery for surfactant replacement or other therapies⁸⁴. MPS are applicable to lung diseases: asthma and bronchiectasis endotypes have been described recently, and similar to ARDS, little is known about the biological mechanisms behind them^{85,86}. However, both diseases also involve inflammation, remodeling and mechanical force in the lungs.

In conclusion, MPS have transformed *in vitro* cell culture and opened the door to complex *in vitro* analysis that could uncover these biological mechanisms and accelerate the translation of new phenotyping methods to critically ill patients. Overall, MPS have tremendous potential to reveal patient-specific biological endotypes which would improve personalized outcomes of importance to patients.

CHAPTER 2. OBJECTIVE OF THIS THESIS

As established in Chapter 1, certain lines of investigation into small airway disease are inaccessible using traditional methods such as animal models, primary human specimens, and *in vitro* monoculture. Particularly, several central mechanisms of small airway injury are excluded from investigation with these methods. Improved methods of studying small airway fluid mechanical injury and inflammation could therefore lead to novel treatments that address these mechanisms. The goal of this thesis is therefore to establish novel small airway microphysiological models for the study of small airway diseases.

In Aim 1, we establish a novel microfluidic lung-on-a-chip that recapitulates the dimensions and fluid properties of the distal airway. We generate controlled-volume liquid plugs using electronically actuated valves and propagate plugs to injure primary small airway epithelial cells in the microfluidic device. We demonstrate that alteration of fluid viscosity increases plug propagation speed, indicating a role for viscosity in airway epithelial injury.

In Aim 2, we model the small airway air-blood barrier (ABBA) in high-throughput using automatable techniques. This Aim provides a critical *in vitro* platform for the investigation of epithelial-endothelial interactions that potentiate barrier function. We establish novel methods for the generation of a 96-well ABBA and demonstrate dose-dependent epithelial-endothelial responses to viral and bacterial mimics, as well as live virus.

In Aim 3, we extend the ABBA platform developed in Aim 2 to perform a neutrophil transmigration assay. We show that neutrophils migrate and become activated dose-dependently and without edge effects. We demonstrate that the transmigration model recapitulates key features of CF airway disease. Finally we generate dose response curves of two inflammation-modulating therapeutics to compare their potency for two donors.

Overall, this thesis contributes novel methods for the generation of small airway disease-relevant microphysiological systems. The methods established herein form the foundation for investigations of small airway disease pathophysiology in a tightly controlled microenvironment that captures functional disease mechanisms, including fluid mechanical stress, barrier potentiation and immune cell recruitment.

CHAPTER 3. MICROFLUIDIC MODEL OF PULMONARY EDEMA IN THE DISTAL AIRWAYS

3.1 Introduction

The distal airways are coated in a thin layer of airway surface liquid that keeps the epithelial cells hydrated, sequesters pathogen and particles for clearance, and has antimicrobial properties⁸⁷⁻⁸⁹. However, the annular liquid coating is subject to the Rayleigh instability, which is the result of fluids' tendency to minimize their surface area. In the liquid-lined airway, Rayleigh instability describes the instability of the interface between the air and the liquid coating the airways. The instability manifests as coalescence of the liquid lining into an obstructing liquid plug⁹⁰ (**Figure 3-2**). In healthy airways, the Rayleigh instability is minimized by the presence of surfactant in the airway surface liquid that lowers the surface tension at the air-liquid interface. Therefore, the probability of liquid plug formation is significantly reduced to start out with and the fluid mechanical stress of any plugs that do form are low making this not typically a problem in healthy individuals⁵⁴.

Under disease conditions, however, liquid plugs can appear in much larger numbers. Causes include surfactant dysfunction, excess fluid volume, and alterations in the airway surface liquid viscosity⁹¹. The liquid plugs can be pushed along the airway during breathing. As they propagate, they leave behind their liquid volume until the meniscus becomes too thin and the plug pops⁴⁷. This phenomenon is thought to create the lung sounds called crackles that are heard by a physician with a stethoscope⁴⁷. Crackles are associated with a number of lung diseases and serve as a non-specific indicator of potential

illness when observed in the clinic⁴⁷. Additionally, experimental evidence suggests that they contribute to pathophysiology in distal lung diseases^{1,47}.

Liquid plugs are poorly understood owing to complexity of fluid mechanics analysis and limited availability of experimental model systems. Observation of this process within a live animal or *ex vivo* organ is incredibly difficult, because of control the flow of air and liquid within a given airway precisely and in imaging the flows. Conditions that lead to plug formation is also typically confounded by other factors, cell types, structures, etc. making analysis of the effect of the fluid mechanical events difficult. Previously our group modeled liquid plug propagation and rupture in a microfluidic system, showing that liquid plugs induce epithelial cell death^{53,54,92}. This system had a two-inlet two-outlet design with continuous air- and liquid-flow with intermittent diversion of air flow to generate the plugs. The two-outlet design made stable long-term operation (more than ~10 minutes) difficult due to rapid uneven resistance build up between the two outlet channels owing to the continuous inflow of liquid. Therefore, we were unable to investigate long-term impacts of liquid plug generation on the airway epithelium.

Here, we describe a device that has a two-inlet one-outlet design that can maintain long-term stable operation. Additionally, the new device has a more physiologically curved, rather than rectangular, cross-sectional shape, has a much lower liquid inflow rate, and has a more physiologically-relevant mechanism of liquid plug formation. To assess stability and robustness of the new device, we analyze liquid plug generation stability and generate plugs with viscosities significantly higher than that of aqueous solutions used previously.

3.2 Materials and Methods

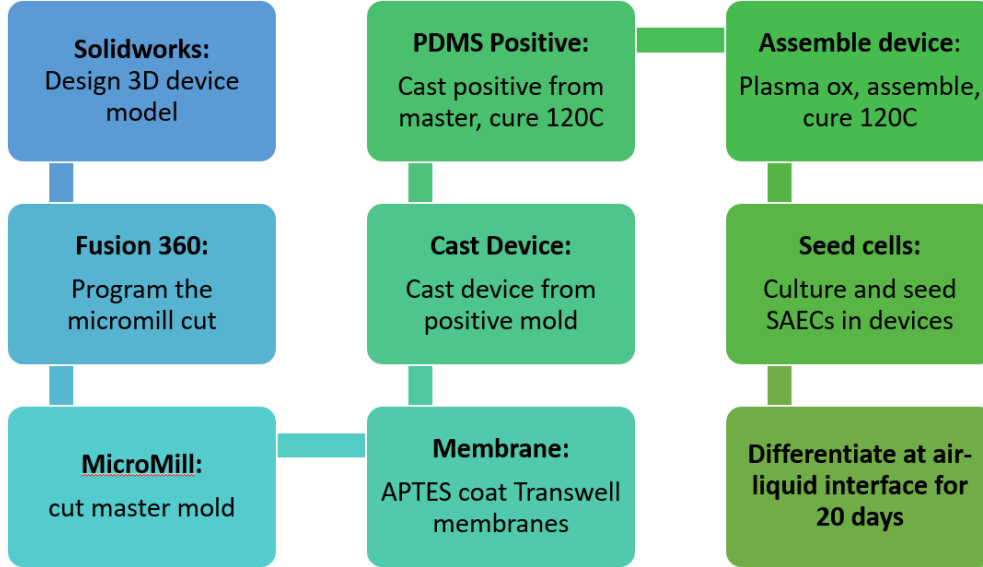


Figure 3-1. Process for fabrication of microfluidic small airway-on-a-chip

3.2.1 Microfluidic device fabrication

Microfluidic device fabrication followed the process depicted in **Figure 3.1**. In brief, 3D designs for the top and bottom microfluidic channels were created in SolidWorks. Negative molds were micromilled into acrylic using paths designed in Fusion360 (AutoDesk) with 1 mm, 200 μm and 100 μm tools (Performance Micro Tool and Harvey Tool). Positive molds were cast into the acrylic negative mold with PDMS in a 5:1 wt:wt ratio with SU-84 crosslinking agent. The PDMS-crosslinker was poured onto the acrylic mold, placed under vacuum for 20 minutes to remove air bubbles, and baked at 65C overnight. The PDMS was then separated from the acrylic mold and further baked at 120C overnight. Finally, the PDMS positive mold was used to cast devices in PDMS. PDMS was mixed 1:10 with SU-84 crosslinker and poured over the PDMS positive mold. This was placed under vacuum for 20 minutes, and then baked for 2 hours at 65C. The PDMS devices were then separable from the PDMS mold. Devices were cut out, and holes were biopsy

punched (1.5 mm diameter). Membranes were fabricated from Transwell inserts (Corning 353102) with pore size 1 μm . Membranes were cut out of the plastic Transwell insert and treated with 5% v/v APTES solution in distilled water at 80 °C for 20 minutes. Temperature during the surface treatment was maintained by verifying with a laser thermometer. Following the surface treatment, membranes were hung to dry in the fume hood overnight. Finally, devices were assembled using plasma oxidation. Membranes and top channel were treated with oxygen plasma for 30 seconds at 120 volts and the membrane was bonded to the top channel. Then, the top channel + membrane was treated with the bottom channel (30 seconds, 120 V) and the top and bottom channels were assembled. The finished device was post-baked at 65 °C for an additional 2 hours to solidify the bonding.

Cell Culture

Complete devices were sterilized under UV light for 20 minutes prior to use. Type I rat tail collagen (Corning 354236) was suspended at 26 $\mu\text{L}/\text{mL}$ in cold, sterile PBS that was previously adjusted to pH 9 with sodium hydroxide to avoid collagen gelation. Collagen suspension was added to top channels and allowed to incubate for 90 minutes. Following incubation, the collagen was replaced with cell culture media and the T-channel was plugged to prepare for cell seeding. The entrance and exit to both top and bottom channel were given cut-off P1000 pipette tips to serve as media reservoirs and to deliver cells and media. Primary small airway epithelial cells were purchased from Lonza (CC-2547) and expanded in Lonza's small airway growth medium with BulletKit supplements as instructed (CC-3118). For device seeding, cells were passaged at 60-80% confluence according to Lonza instructions using Lonza Reagent Pack (CC-5034). Small airway cells were then seeded into devices at 3-4 million cells/mL, 30 $\mu\text{L}/\text{channel}$, by adding the cells

to the top channel pipette tip (to avoid lethal excess shearing). Cells were allowed to flow across the top channel and settle evenly. The devices were incubated for 2 hours to allow cell attachment, and then 100 μ L of cell culture media was perfused across the top channel to remove unattached cells. Devices were cultured under liquid-liquid conditions for 2 days following seeding with daily media exchanges. On Day 3, media was replaced with Lonza's S-ALI differentiation media (CC-4539) on the top and bottom channels. After 24 hours, the media in the top channel was removed extremely gently, and cells were fed from the bottom with daily media changes for 14 days until experiments. Devices were placed on a wave plate inside a humid incubator to perfuse media through the bottom channel continuously during the ALI culture period.

3.2.2 *Plug generation*

Valve control was achieved by programming an Arduino controller to apply arbitrary voltage patterns to two 3-way solenoid valves (Lee Company). The air flow comes from a compressed air tank, passes through a mass flow meter (density, temperature, and pressure-independent flow measurement based on the Coriolis principle, Bronkhorst), enters the 3-way valve, splits to a pressure meter (Omega Engineering, PX409-001DWUUSBH) and finally enters either to the device or to the vent. The liquid is fed from a flow-rate controlled syringe pump (NemeSys) and passes through the 3-way valve and pressure meter into either to a drain line or into the device. The device outlet is attached to a 2-inch drain tube at atmospheric pressure that lands in a conical vial to collect waste. The liquid plug generator was mounted on a brightfield microscope (Olympus) to capture images of plug propagation and rupture. The images were captured by a Phantom high speed microscope (Vision Research).

3.2.3 *Cell counting and statistics*

Following plug exposure, devices were incubated for 10 minutes with a mixture of live cell-permeable NucBlue (Invitrogen R37605) and live-cell impermeable Sytox Green (Invitrogen S7020) followed by rinsing with Hank's Balanced Salt Solution. Membranes were cut out from devices and mounted on glass slides. Images were captured, using identical settings across conditions, on a Leica DMI8 Microscope. Image-based quantitation of cells from resultant immunofluorescent stains was performed using the ImageJ segmentation plugin CellPose⁹³.

3.3 **Results**

3.3.1 *Device design and fabrication*

We aimed to replicate the distal airways to capture physiologically relevant fluid dynamics. The distal lungs are those with diameter 0.1-2 mm. We modeled the terminal bronchioles that are the most distal airways with bulk air flow. Their diameter ranges from 0.5-0.1 mm⁹⁴. Our device diameter was therefore approximately 0.5 mm (0.05 cm). We used a micro mill to design a semi-rounded channel that would approximate the shear stress profile of the airways in a circular conduit⁹⁵. To determine the air speeds required in our device, we utilized general calculations for air speeds based on airway generation developed by Weibel⁹⁴. The approximate velocity of airflow at airway diameter 0.05 cm in a healthy adult is calculated as follows:

$$d_n = d_0 * 2^{-\frac{n}{3}}$$

$$A_n = \frac{\pi d_n^2 2^n}{4}$$

$$U_n = \frac{Q}{A_n}$$

Where:

d_n = airway diameter at generation n [cm],

d_0 = tracheal diameter [cm]

n = airway generation

A_n = cross-sectional area of generation n airway

Q = flow rate of air into the lungs [mL/s]

U_n = air velocity at generation n airway [cm/s]

The resultant Reynolds number can be calculated:

$$Re = \frac{\rho D_h v}{\mu} = \frac{Q}{A_n} * \frac{d_n}{\nu}$$

where

ρ = density [kg/m³],

D = hydraulic diameter [m],

μ = dynamic viscosity [kg/m-s]

ν = kinematic viscosity [m²/s]

Assuming a round airway of diameter 5 mm, a breathing rate of 500 mL/s, tracheal diameter of 2 cm, and kinematic viscosity of air 0.15 m²/s, the resultant airway generation is 16 and the velocity is 3.95 cm/s and $Re = 1.31$. Therefore, airflow is laminar. We aimed to replicate this air speed in the channel while incorporating physiologically rounded

airway geometry. Therefore, we designed a channel with hydraulic diameter of 0.46 mm and cross-sectional area 0.193 mm² (**Figure 3-2(B)**). This semicircular geometry closely approximates a round tube with diameter 0.5 mm and cross-sectional area 0.196 mm² (**Table 1**). Further, the measured air velocity in the microfluidic channel confirms that air velocity approaches the approximate calculation.

Table 1. Comparison of *in vivo* airway and microfluidic device

Value	Airway (Gen.16)	Microfluidic Device
Hydraulic diameter [mm]	0.496	0.46
Cross-sectional area [mm ²]	0.196	0.193
Velocity [cm/s]	3.95	15
Re	1.31	4.6

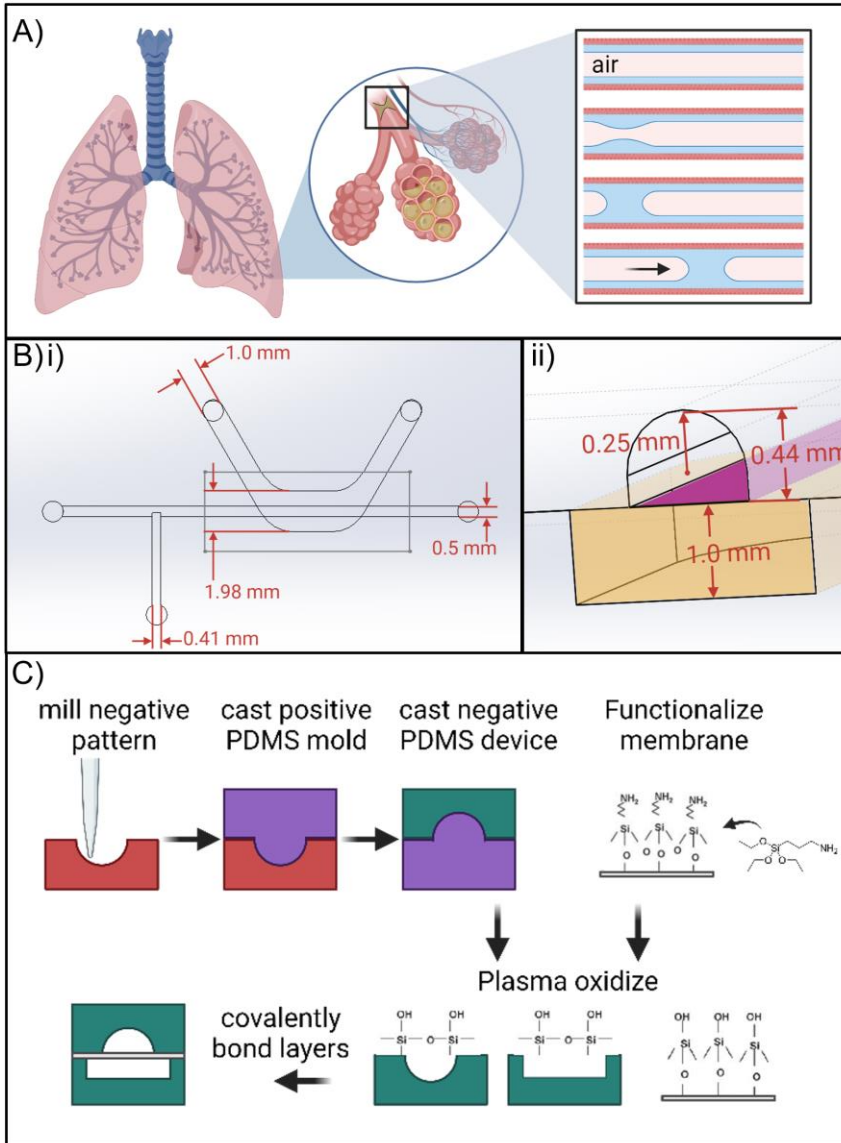


Figure 3-2 Small airway plug generator

A) Rayleigh instability in the distal airways can lead to liquid plug obstruction and propagation. B) The microfluidic device design and dimensions. C) Fabrication of the microfluidic device.

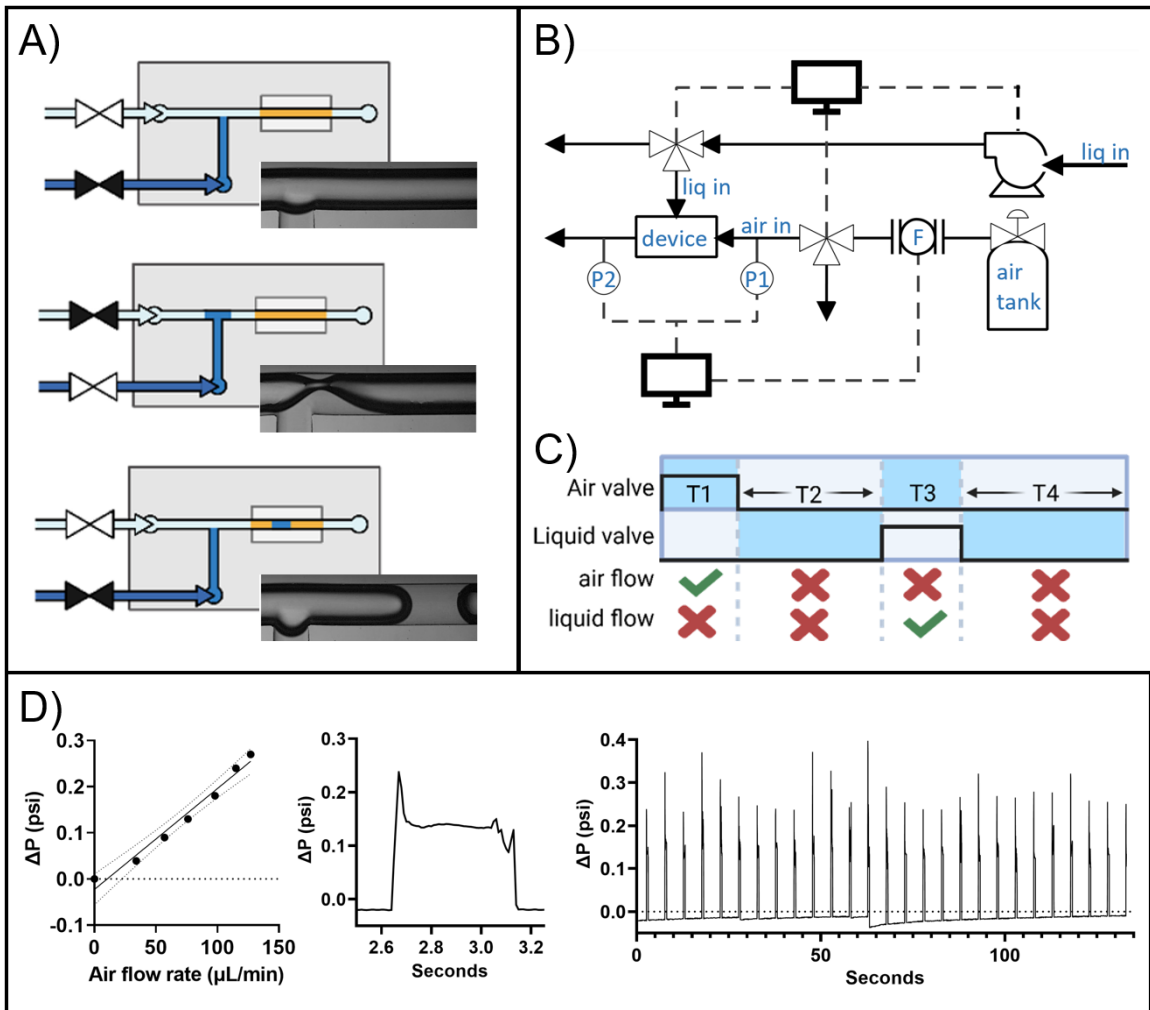


Figure 3-3 Liquid plug generation in microfluidic device

A) Plug generation based on alternative activation of valves. B) Process flow diagram for plug generator. C) Voltage scheme for valve control with four controllable times (T1-T4). D) Pressure drop from the inlet to outlet of the device. Left: pressure drop vs. air flow rate. Middle: Zoom-in of a single plug pressure vs. time graph. Right: pressure vs. time for over two minutes shows consistent plug generation.

3.3.2 Plug generator

While previous plug generating microfluidic airway devices have been reported, this device is the first, to our knowledge, to enable stable plug generation. This feature is critical to future studies that require long term plug application. Importantly, plugs may rupture in a single airway with every breath or infrequently over a longer time scale.

Therefore, we designed a plug generation process that automates plug fabrication and enables consistent generation of controlled-volume plugs (**Figure 3-3**). The device consists of a straight air channel perpendicular to a liquid injection channel. Conveniently, air and liquid sources (gas tank and syringe pump, respectively) were allowed to generate a constant flow rate. Air and liquid inlets were controlled by three-way electronically actuated valves that diverted air and liquid from the microchannel inlets upon applying a voltage. During liquid injection, air flow was stopped to prevent premature movement of the liquid bolus. After liquid loading is complete, liquid inlet is closed and the air flow is returned to the channel, enabling propagation of the liquid plug. Control of valve actuation and therefore air and liquid inlets was achieved using LabView fed to an Arduino control board. Controllable parameters are air flow rate, liquid flow rate, and T1-T4. Liquid plugs were generated according to the strategy described above, for a liquid flow rate of 500 $\mu\text{L}/\text{min}$ and air flow rate of 60 $\mu\text{L}/\text{min}$.

3.3.3 *Liquid plug cell injury*

To demonstrate the application of the lung-on-a-chip towards studying fluid mechanical stress, primary small airway epithelial cells were cultured in the microfluidic devices for 3 days (**Figure 3-4**). Then, either no plugs or 10 plugs were applied to the cells over a period of 50 seconds (one plug every five seconds). Application of surfactant-free liquid plugs induced epithelial cell death along the center of the channel.

3.3.4 *Effect of liquid viscosity on plug propagation*

To demonstrate an application of the model system, we investigated the effect of increased liquid viscosity on plug propagation speed. In various lung diseases, airway surface liquid has abnormally high viscosity due to excessive mucins, extracellular DNA, low water content, and other disease-associated factors⁹⁶. We generated liquids of increasing viscosity that modeled COPD airway surface liquid by dissolving PBS with increasing concentrations of 500k Dextran. Viscosities were verified on a rheometer. The control PBS had an average viscosity of 1.0 cP, the healthy individual, 6.1 cP, healthy smoker, 12.6 cP and COPD smoker 628.5 cP. These values fall within the ranges of mucin viscosity found by Lin et al⁹⁷ for COPD patients.

After the solutions with different viscosities were made, the plugs were propagated through microfluidic devices with an Arduino controlled set up. Within a period of 5 seconds, liquid would enter the channel for 0.5 seconds, followed by air for 0.5 seconds. To capture physiological rates, the air flow rate from the gas tank was set to 50 +/- 2 $\mu\text{L}/\text{min}$ and liquid flow rate was set 100 $\mu\text{L}/\text{min}$ from the Nemesys syringe pump. The speeds were collected with the assistance of the Phantom Camera Control (PCC) software. Each video had a sample rate of 500 frames per second and a resolution of 832 x 400 pixels. The speed was defined using the 2-point instant active measurement. The first point being the end of the plug at rest and the second that same edge of the plug before it left the camera frame. Increasing the fluid viscosity decreased the speed of plug propagation (**Figure 3-4(B)**).

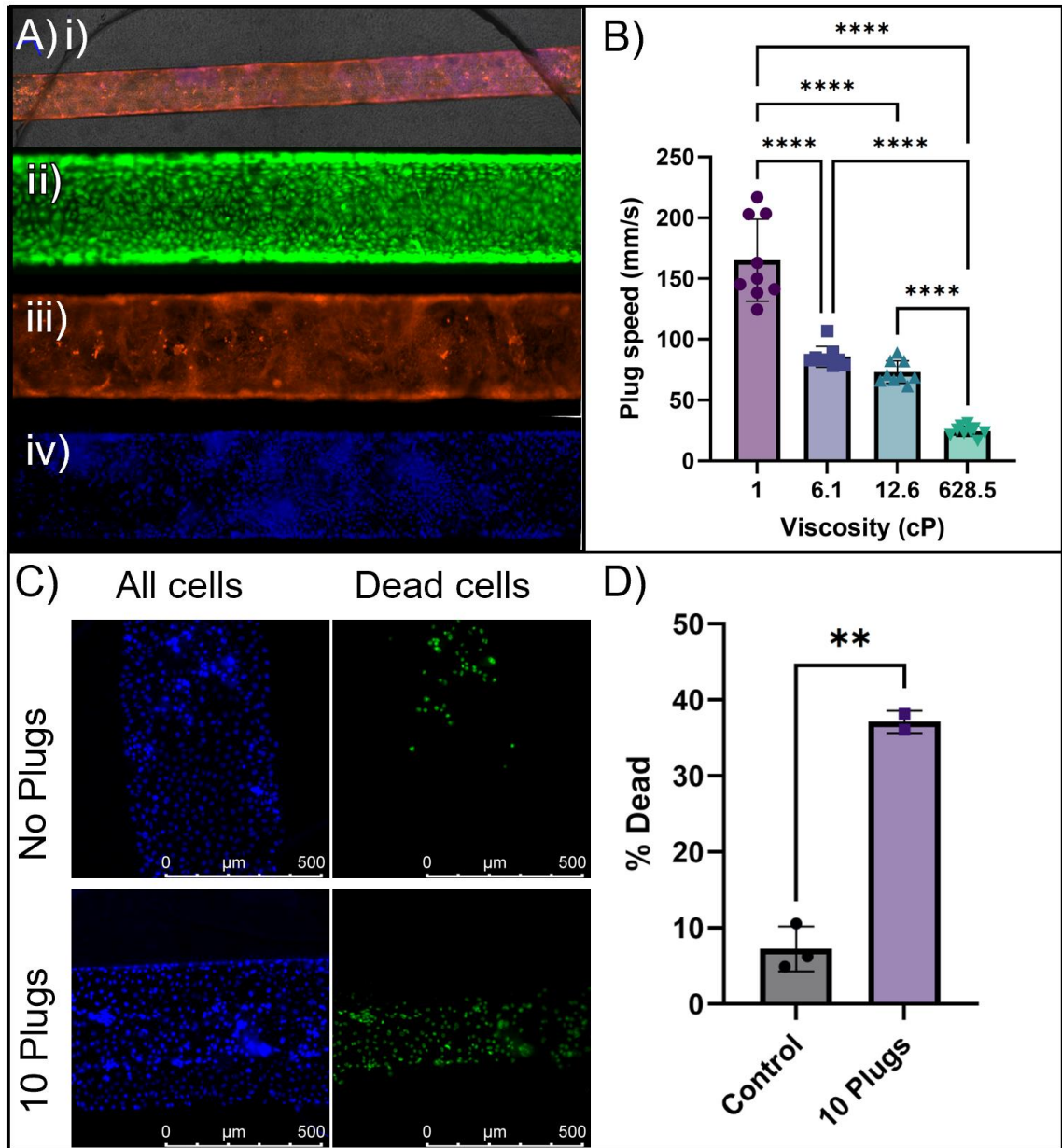


Figure 3-4 Liquid plug propagation and viscosity effects

A) Cell culture in the microfluidic device. Top: CellMask stain of the cell membrane. ii) live cell stain shows that cells are confluent and alive 24 hours after seeding. iii) Cell membrane stain (CellMask) showing that cells are confluent after 3 days of submerged culture. iv) NucBlue stain of the nuclei from iii). B) Viscosity vs. plug speed. C) Imaging of NucBlue and Sytox Green stain to determine viability. D) Viability for control vs. plug condition.

3.4 Discussion

In this chapter, we developed a microfluidic model of fluid mechanical stress in the distal airways using a custom-designed and fabricated microfluidic device. While our group previously developed a liquid plug generating device to study respiratory fluid mechanics, the plug generation was stable for only minutes at a time. Here, we automate plug generation to stably produce consistent liquid plugs of arbitrary size, speed, and time between plugs. We show that plugs can be generated consistently. Second, we demonstrate that liquid plugs injure the epithelium, replicating previous findings.

Finally, we show that liquid viscosity alters plug propagation speed. This suggests that in diseases with viscous pulmonary exudates, such as CF and chronic obstructive pulmonary disease, liquid plugs take longer to clear the airways when the same pressure differential is applied compared to liquid plugs comprised of lower-viscosity liquid. This potentially longer residence time in diseased airways means that plugs significantly impact the sick patient's lung function. In asthma, mucus plugs in the small airways were found to correlate with inflammation and overall airflow obstruction⁹⁸. The effect of viscous airway surface liquid with abnormal properties, therefore, appear compounding. Not only are sick patients predisposed to plug formation due to an abnormally thick airway surface liquid, surfactant dysfunction, or narrowed airways due to remodeling, but the plugs they do form are more likely to take a long time to clear, having further impacts on lung function.

Importantly, previous work suggests that slower liquid plug propagation is less injurious to the epithelium than fast propagation⁹⁹. The high-viscosity, low-velocity plugs

may impart less epithelial injury than fast, low-viscosity plugs, despite the deleterious effects on lung function. However, the increased viscosity also increases wall shear stress which contributes to epithelial injury⁹⁹. Future experimental studies using the liquid plug propagation microfluidic device should investigate whether slow-speed, high-viscosity plugs are more injurious to the epithelium compared to faster-speed, low-viscosity plugs.

CHAPTER 4. A HIGH-THROUGHPUT DISTAL LUNG AIR-BLOOD BARRIER MODEL ENABLED BY DENSITY-DRIVEN UNDERSIDE EPITHELIUM SEEDING

While developing the microfluidic platform, we appreciated the significant limitations that microfluidics introduced to the small airway model. The arduous custom fabrication process required significant time and resources and was difficult to reproduce precisely. There was great difficulty culturing cells at the air liquid interface due to Rayleigh instabilities. Finally, the nature of plug generation and rupture necessitated low throughput experiments where only one device was exposed at a time.

Our next goal was to incorporate endothelial cells into the small airway model. However, given the above limitations we experienced so far, we determined that a novel design was required that would meet reasonable standards of throughput and quality control. Ultimately we decided to transition to a high-throughput culture platform that would be more suitable for studies of cell-cell communication and, later, immune cell transmigration.

*This chapter is reproduced from our publication “A high-throughput distal lung air-blood barrier model enabled by density-driven underside epithelium seeding” in *Advanced Healthcare Materials* (2021)¹⁰⁰.*

4.1 Introduction

High-throughput (96-well or more) cell culture platforms enable rapid testing of large condition sets for physiologic studies of cellular responses to various stimuli. In the lung, submicron aerosols and particles accumulate preferentially in the alveoli and respiratory bronchioles^{101,102}. Therefore, the distal lung region is frequently modeled *in vitro* using high-throughput platforms to study pathophysiology and screen for therapeutics^{103–105}.

However, high-throughput lung barrier models typically consist of a monocultured epithelium that neglects the barrier-potentiating effects of the nearby capillary endothelium^{103–108}. The epithelium provides the majority of the air-blood barrier strength through robust expression of tight junctional complexes¹⁰⁹, but the capillary endothelium potentiates epithelial barrier function by paracrine signaling with significant consequences for overall air-blood barrier function¹¹⁰. For example, acute lung injury characterized by loss of epithelial barrier function can originate from endothelial activation and dysfunction rather than direct epithelial injury^{111,112}. Additionally, an injured epithelium may release cytokines that activate the endothelium to recruit and activate neutrophils^{73,113,114}, in some cases resulting in severe epithelial damage^{115,116}. Therefore, to capture the distal lung's barrier function and inflammatory response to stimuli, incorporating both the epithelium and endothelium in a model is critical.

To account for endothelial contribution to barrier function, existing distal lung tissue barrier models include the epithelium layer grown on a permeable support membrane opposite a co-cultured endothelium. These bilayer co-culture models have yielded

substantial insights regarding the pulmonary physiology during exposure to viral infection^{117,118}, bacterial insult¹¹², particles^{119,120}, toxins^{121–123}, and tissue injury¹²⁴. Some models also include co-cultured or transmigrating immune cells that further enhance physiologic relevance^{125–129}. However, these co-culture models are almost exclusively in 6-, 12-, or 24-well plates and in low-throughput microfluidic devices that limit their utility^{1,130}.

One reason for this limitation in throughput is the requirement to culture two cell types on opposite sides of a culture membrane. Such co-culture is typically performed in 6- to 24-well plates where underside of the culture inserts is seeded by manually inverting the culture insert, seeding cells in a bolus of liquid, and allowing them to attach before righting the membrane. (**Figure 4-1(B)**)^{131–133}. However, in a 96-well Transwell, this inversion method is difficult to automate and prone to failure due to the limited culture area of 0.143 cm² per well. Specifically, less than 30 μ L of liquid can be placed on inverted 96-well membrane inserts, meaning that cells must be very concentrated, and the risks of evaporation and contamination during cell attachment are significant (author observation).

To address these challenges, we eliminate the need for inversion by exploiting density-driven cell floating for underside cell seeding. We then use this technique to develop a robust tissue barrier platform with scalable, automatable co-culture that requires no plate inversion and uses commercially available reagents and liquid handling equipment. We show in a model of the distal lung epithelial-endothelial barrier that co-culture is necessary for increased barrier strength, and communication between cell types mediates response to inflammatory pathogens. The model recapitulates key air-blood barrier features including low permeability, high trans-epithelial electrical resistance

(TEER), epithelial-endothelial communication, and loss of barrier function in response to inflammatory stimuli. We also demonstrate the capability of epithelial culture on the underside of the membrane under air-liquid interface culture (ALI) conditions with serum-free, glucocorticoid-free media. This novel seeding method should be translatable to many vascular-epithelial tissue barriers and eliminates a bottleneck step of the bilayer co-culture process.

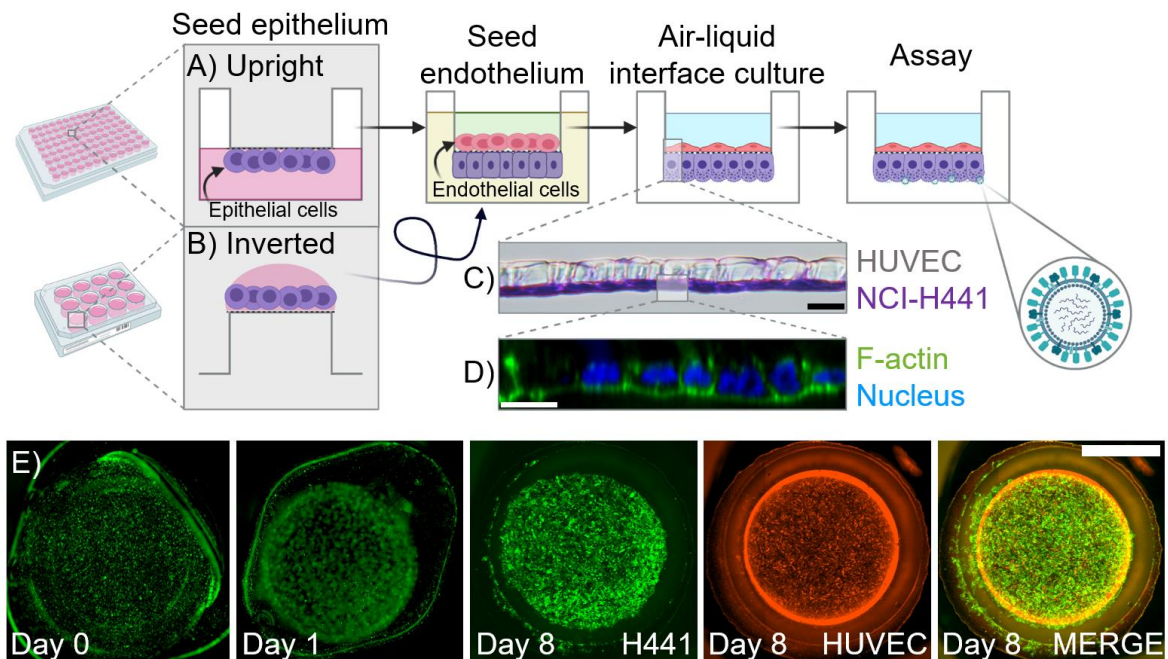


Figure 4-1. Automatable underside seeding enabled by density-driven flotation forms a robust monolayer of NCI-H441 cells in co-culture with a vascular endothelium.

A,B) Seeding on the underside of Transwell membranes is typically accomplished by insert inversion (B). Density-driven flotation method enables upright underside seeding without inversion (A) for facile generation of bilayer co-cultures. **C)** Histology section with hematoxylin and eosin stain shows epithelial-endothelial culture on opposite sides of the Transwell membrane. **D)** Confocal imaging of the epithelium stained for F-actin shows that NCI-H441 cells form a monolayer with this seeding method. **E)** At initial seeding time (Day 0), NCI-H441 cells float to the underside of the Transwell membrane where they adhere for 2 hours. By 24 hours (Day 1), epithelial cells are attached on the underside of the membrane. On Day 8, following 6 days of ALI culture, NCI-H441 cells are limited to the culture area that is fed from the opposite side and both layers are confluent. Scale bar, 20 μ M (top 2 images), 2.13 mm (bottom).

4.2 Methods

4.2.1 NCI-H441 maintenance in T-75 flasks

NCI-H441 human adenocarcinoma cell line was purchased from American Type Culture Collection (ATCC) (ATCC® HTB-174™). NCI-H441 cells were expanded in RPMI-1640 (ATCC® 30-2001™) supplemented with 9% fetal bovine serum (50 mL into 500 mL media for total volume 550 mL), Penicillin-Streptomycin (Gibco™ 15140148) diluted 1:100 v:v, and 1.5 µg mL⁻¹ puromycin. NCI-H441 cells were transduced to express GFP as described below. For routine culture, GFP-H441 cells were seeded at density 1e6 cells per 75 cm² in 20 mL cell culture media. After passage (day 0), media was changed every 48 hours on the following schedule: day 2, 20 mL; day 4, 40 mL; day 6, passage. For media changes, NCI-H441 media was aspirated, cells were rinsed with 10 mL warm phosphate buffered saline (PBS) (Gibco™ 10010023), and media was replaced. For passage, NCI-H441 T-75 flasks were rinsed with 10 mL warm PBS and lifted with 2 mL 0.05% Trypsin-EDTA (Gibco™ 25300120). Trypsin was neutralized with media and cells were spun down (200 g, 5 min, 25 °C), resuspended in 1 mL media and counted for seeding with Nexcelcom Cellometer Auto T4 Bright Field Cell Counter (Nexcelcom Bioscience) using Trypan Blue viability stain. Cells were used below the 8th passage after obtaining from ATCC.

4.2.2 HUVEC maintenance in T-75 flasks

Primary HUVECs were purchased from ATCC (ATCC® PCS-100-013™) and expanded according to manufacturer instructions in Vascular Cell Basal Medium (ATCC®

PCS-100-030™) supplemented with Endothelial Cell Growth Kit-VEGF (ATCC® PCS-100-041™) with added Penicillin-Streptomycin (Gibco™ 15140148) diluted 1:100 v:v. HUVECs were transduced to constitutively express RFP as described under Lentiviral Transduction. However, puromycin was not included in routine cell culture medium because the cells did not tolerate it well for long time periods (unpublished observation). Cells were passaged at 60-80% confluence according to manufacturer instructions, counted with Nexcelcom Cellometer Auto T4 Bright Field Cell Counter (Nexcelcom Bioscience) using Trypan Blue viability stain, and used below the passage 10 since expanding from ATCC.

4.2.3 *Lentiviral transduction*

NCI-H441 cells and HUVECs were transduced with lentivirus to constitutively express GFP and RFP, respectively. NCI-H441 cells were seeded in T-75 flasks at 0.75×10^6 cells per 75 cm^2 and allowed to attach overnight. Then NCI-H441 cells were inoculated with lentivirus encoding GFP and puromycin resistance (Cellomics Technology, CMV-GFP lentivirus). 8 transfection units per cell were suspended in NCI-H441 routine culture media with the addition of transfection reagent polybrene ($1 \mu\text{g mL}^{-1}$). The cells were inoculated overnight and then allowed to recover in routine cell culture media for 72 hours with media changes every 48 hours. Then, expressing cells were selected with puromycin. Cells were cultured in routine culture media plus puromycin ($1.5 \mu\text{g mL}^{-1}$) until passage 3. GFP-H441 cells were then frozen in puromycin-containing media with 0.05% v/v cell culture-grade DMSO (ThermoFisher D12345). For RFP transduction of HUVECs, HUVECs were seeded at 8000 cells per cm^2 in 6-well plates and allowed to attach overnight. Then they were inoculated with 8 TU cell⁻¹ RFP-gene bearing lentivirus

(Cellomics Technology, CMV-RFP lentivirus) in cell culture media supplemented with polybrene ($1 \mu\text{g mL}^{-1}$) and incubated overnight. The viral media was removed and the cells were allowed to grow in routine culture media for 72 hours with media change every 48 hours. Then, RFP-expressing cells were selected by culturing in cell culture media supplemented with $1.5 \mu\text{g mL}^{-1}$ puromycin for 2 days. The selected cells were then expanded to passage 5 and frozen in puromycin-containing media with 0.05% v/v cell culture-grade DMSO (ThermoFisher D12345). For routine culture of HUVEC-RFP after thaw, puromycin was not included because HUVECs did not tolerate it for long time periods (author observation).

4.2.4 *Trans-epithelial electrical resistance (TEER)*

TEER was monitored daily beginning 48 hours after NCI-H441 cell seeding using EVOM2 0-10 k Ω Range Epithelial Volt/Ohm Meter (World Precision Instruments) with the STX100C96 electrode (World Precision Instruments). The electrode was maintained as recommended by the manufacturer. The electrode was cleaned by incubating overnight with Tergazyme (Alconox 1304-1), sanded gently as needed with sandpaper provided by the manufacturer to keep the metal surfaces clean and exposed, and was soaked as needed in 5% v/v sodium hypochlorite for 5 minutes to maintain conductivity. Raw measurements of TEER were corrected according to the following formula:

$$TEER (\Omega \cdot \text{cm}^2) = [(Raw TEER value) - 200 \Omega] * 0.143 \text{ cm}^2$$

200 Ω is the average value of a blank well with the equivalent volume of cell culture media, while 0.143 cm^2 is the surface area of the cell culture insert. For TEER measurements of wells at ALI, 200 μL pre-warmed 37 $^\circ\text{C}$ PBS was added to the bottom

chamber for measurement. For all TEER measurements, plates were placed on aluminum warming blocks to maintain constant temperature because TEER can change with temperature.

4.2.5 Staining and imaging

All stains used reagents from from ThermoFisher's Image-iT™ Fixation/Permeabilization Kit (R37602) for washing, fixing, blocking and permeabilization. For all stains, inserts were cut out and fixed on glass slides for 10 minutes at 37 °C. For stains requiring permeabilization, the inserts were incubated with 0.5% w/v Triton X (ImageIT kit) for 5 minutes at 37 °C. All inserts were blocked for 1 hour at 37 °C, counterstained with DAPI (1:1000 in PBS for 5 minutes) and mounted between two coverslips with ProLong™ Diamond Antifade Mountant (Invitrogen). *F-actin*. After fixation, permeabilization, and blocking, inserts were incubated for 1 hour at 37 °C in Alexa Fluor™ 647 Phalloidin (Invitrogen) diluted 1:20 from stock solution in 1% w/v BSA (Image-iT™). *ZO-1/e-cadherin co-stain*. After fixation, permeabilization, and blocking, the primary antibodies (ZO-1 Rabbit anti-human polyclonal antibody, ThermoFisher 61-7300, 1:200; e-cadherin Mouse anti-human monoclonal antibody, ThermoFisher 13-1700, 1:2000) were suspended together in 1% w/v BSA (Image-It Kit) and co-incubated with the inserts for 2 hours at 37 °C. The filters were washed 3 times with 1% w/v BSA. The secondary antibodies (Goat anti-Rabbit IgG, Alexa Fluor 405, Abcam ab 175665, 1:200; Goat anti-mouse IgG, Alexa Fluor 647, ThermoFisher A32728, 1:500) were suspended in 1% BSA and incubated with the filters for 2 hours at 37 °C. *VE-cadherin*. After fixation, permeabilization, and blocking, the primary antibody (Goat anti-human polyclonal VE-cadherin antibody, R&D Systems AF938, 1:13) was suspended in 1% w/v BSA and

incubated with the inserts for 2 hours at 37 °C. The filters were washed 3 times with 1% w/v BSA. The secondary antibody (Donkey Anti-Goat IgG H&L (Alexa Fluor® 405) preadsorbed (ab175665)) was suspended in 1% BSA and incubated with the filters for 2 hours at 37 °C. The filters were washed 3 times with 1% BSA and stained with DAPI. *Von Willebrand Factor*. After fixation and blocking, the primary antibody (Rabbit anti-human polyclonal, Abcam ab6994, 1:200) was incubated with the filters in 1% w/v BSA for 1 hour at 37 °C. The filters were washed 3 times with 1% BSA. Then the secondary antibody (Goat anti-rabbit polyclonal, ThermoFisher A-21245, 1:200) was incubated with the inserts in 1% w/v BSA for 1 hour at 37 °C. Then the filters were washed and stained with DAPI. Epifluorescence images were taken using Leica DMI-8 or EVOS. Confocal images were taken at Georgia Tech's Optical Microscopy Core with a PerkinElmer UltraVIEW VoX spinning disc confocal microscope using a 40X (numerical aperture 1.3) or 60X (numerical aperture 1.49) objective.

4.2.6 *Histology*

Histology was performed in the Parker H. Petit Institute's histology core. Inserts were fixed (Image-iT™) and embedded in OCT so that the filters are perpendicular to the cutting angle. Blocks were sectioned at 10 µm thickness, stained with hematoxylin and eosin, and imaged on Leica DMI-1 with a color camera.

4.2.7 *Permeability assays*

Fluorescein sodium salt (Sigma-Aldrich, F6377) was diluted to 30 µM in ALI media. 200 µL media was added to the bottom chamber and 140 µL media with tracer was added to the top chamber. 50 µL was sampled and replaced with fresh media every 30

minutes for 2 hours. Sample fluorescence was measured in black-walled 96-well plates against a standard curve to determine the mass of tracer in the bottom chamber at each timepoint. Net tracer mass was calculated by accounting for the lost sample at each timepoint. Permeability was calculated using the equation:

$$P_{app} = \left(\frac{dC}{dV} \right) \times \frac{V}{AC_0}$$

Where dC/dV is the slope of a linear fit to the concentration vs. time plot, V is the volume of media in the receiver plate (200 μ L), A is the surface area of the membrane (0.143 cm^2), and C_0 is the concentration of NaFL added in the top chamber (30 μ M).

4.2.8 *Viral exposure*

Influenza A virus, subtype H1N1, strain A/Puerto Rico/8/1934 (NCBI:txid211044) (PR8) was provided by Nick Heaton's laboratory at Duke University School of Medicine. Human coronavirus OC43 (HCoV-OC43) was provided by Rabindra Tirouvanziam's group at Emory University School of Medicine. For infection experiments, PR8 and OC43 were diluted to the desired MOI in cell culture media. Transwell receiver plates were prepared with 200 μ L per well of virus-laden cell culture medium. The Transwell insert plate was placed into the virus-loaded receiver plate and incubated at 37 °C, 95% humidity, 5% CO_2 for 1 hour. Following this incubation, the Transwell receiver plate was moved back to an empty receiver plate to return to ALI without rinsing. The exposed cells were further incubated at 37 °C, 95% humidity, 5% CO_2 until the specified endpoint (24, 48 or 72 hours).

4.2.9 *Cytokine quantitation*

Cell culture supernatants were collected at specified intervals. IL-8 was quantified with ELISA assays according to manufacturer instructions (Human IL-8/CXCL8 DuoSet ELISA, R&D Systems, DY208-05; DuoSet ELISA Ancillary Reagent Kit 2, R&D Systems; DY008).

4.2.10 96-well Transwell upright seeding and maintenance

Polycarbonate 96-well HTS Transwell Permeable Supports with pore size 3 μm were purchased from Corning (CLS3386, CLS3382). The inserts were collagen coated prior to cell seeding to promote attachment. Rat tail collagen type I (Corning 354236) was suspended at 30 $\mu\text{g}/\text{mL}$ in 60% v/v ethanol (Fisher BP8203-1GAL) that was adjusted to pH 6 with hydrochloric acid (0.1 M) and diluted to 60% v/v in sterile distilled water. Inserts were inverted in a sterile biosafety cabinet and 30.3 μL collagen solution was added to the underside of each insert with the VIAFLO-96 liquid handler (INTEGRA Biosciences #6001 and #6106). The inserts were allowed to dry overnight in the sterile biosafety cabinet.

4.2.11 Upright underside seeding

NCI-H441 cells were passaged and suspended at 1.18×10^6 cells/mL in warm cell culture media. The cell solution was gently mixed with sterile, pre-warmed (37 °C) 50% v/v OptiPrep™ Density gradient medium (STEMCELL Technologies 07820) until a homogeneous solution was observed. The solution was immediately transferred to the lower chamber of the HTS 96-well plates (85 $\mu\text{L}/\text{well}$) using a multichannel pipettor or VIAFLO-96 liquid handler, ensuring adequate mixing for even cell distribution. This concentration and volume results in 50,000 cells/well (350,000 cells/cm²). The cells

adhered in this condition for 2 hours in a humid incubator at 37 °C, 5% CO₂, 95% humidity. After 2 hours, 150 µL cell culture media was slowly added to the bottom chamber and 75 µL was added to the top chamber using a VIAFLO-96 Liquid Handler. The plate was then allowed to incubate overnight before HUVEC seeding.

4.2.12 HUVEC seeding

The day following NCI-H441 seeding, the culture inserts were moved to a new receiver plate. HUVECs were seeded in the Transwell chamber on the opposite side of the NCI-H441 cells. HUVEC-RFP cells were passaged and suspended at 80,000 cells/mL. 10,000 cells/well in 100 µL cell culture media were seeded in each well and allowed to incubate overnight.

4.2.13 ALI culture

Inserts were transitioned to ALI after >90% of wells were confluent upon manual inspection with epifluorescence microscopy. Typically this occurs 24-48 hours after HUVEC seeding. To culture at ALI, the media was removed from the bottom chamber and the media in the top chamber was replaced with 50/50% v/v NCI-H441 and HUVEC cell culture media with all supplements except FBS. Instead of FBS, the media contained 1:50 v/v Ultrosor G serum substitute (final concentration 0.2 mg/mL) (Sartorius 15950-017) to promote differentiation and polarization of the epithelium. The plate was then cultured at ALI for 5-7 days until TEER reached above an average of 400 Ω·cm². Assays were typically performed on day 6 of ALI culture, day 9 since seeding NCI-H441.

4.2.14 Statistical analysis

All analysis was performed in GraphPad Prism V8.2.1 using appropriate methods: **Figure 4-5(A)**), Two-way ANOVA with posthoc Tukey's t-test; **Figure 4-5(B)**), 1-way ANOVA with post-hoc Tukey's t-test. Both ANOVAs were performed with multiple comparisons (independent data replicates for each timepoint). (**Figure 4-5(A)**) ANOVA compared across each MOI within the same timepoint for each virus. (**Figure 4-5(B)**) ANOVA compared different conditions versus each other and versus the control condition.

4.3 Results

4.3.1 *Density-driven, inversion-free underside seeding robustly generates a functional air-blood barrier in 96-well throughput*

To capture the properties of the distal lung *in vitro*, we modeled the epithelial barrier using the human adenocarcinoma-derived club cell line NCI-H441. This cell line exhibits properties of both alveolar type II pneumocytes and club cells, making it a suitable representation of the alveolar epithelium or the distal airway epithelium, respectively, depending on the application of interest. NCI-H441 cells function similarly to alveolar type II pneumocytes with regard to ion and drug transport, expressing comparable function and levels surfactant proteins, claudins, Na⁺-K⁺-ATPase, and epithelial sodium channel; as well as drug transporters of the organic cation transporter family^{106,134,135}. However, NCI-H441 cells also maintain features of distal airway club cells regarding inflammatory signaling and barrier function including microvilli, dense cytoplasmic granules holding lectins and proteins, unique expression of the anti-inflammatory CC16 protein, and apical dome shape of cells^{136,137}. NCI-H441 cells also demonstrate strong barrier function reflected by

expression of ZO-1, e-cadherin, and a high TEER^{106,134,138}. Finally, NCI-H441 cells replicate club cells' participation in host defense through production of cytokines, chemokines, anti-inflammatory surfactant proteins, antibacterial, antiviral and anti-protease proteins; and regulation of epithelial barrier function^{118,119,136,137}.

To model the distal lung microvasculature, we used primary human umbilical vein endothelial cells (HUVECs). While there are minor differences in characteristics of endothelial cells from the pulmonary microvasculature vs. other tissue sites, cardinal endothelial properties are maintained in primary HUVECs¹³⁹. These include characteristic surface protein expression (CD31); pinocytotic vesicles; an ellipsoid nucleus with one to three nucleoli; and the presence of Weibel-Palade bodies¹⁴⁰.

The epithelial-endothelial barrier was modeled with the epithelium cultured opposite the endothelium on a 96-well Transwell culture insert (Corning) (**Figure 4-1(C)**, **4-1(D)**). The epithelium was cultured facing downwards, i.e., on the underside of the membrane, due to technical advantages under ALI conditions. Namely, epithelial cells attached outside the co-culture area are rinsed off during ALI culture (**Figure 4-1(E)**), ensuring that the epithelium is a constant surface area and consisting of only co-cultured cells directly opposite the endothelium. Second, underside epithelial culture provides immediate, visual quality control during ALI: faulty wells that cannot hold ALI due to failed seeding or contamination leak quickly and collect media in the plate, while successful wells hold liquid in the top chamber. Finally, the liquid in the underlying plate of the 96-well Transwells is prone to media wicking between wells even when less than the recommended 235 μ L of media is used (here 200 μ L), presenting contamination risk. Therefore, the technical advantages resulting from underside epithelial seeding and ALI

culture reduced well-to-well variability, provided quality control, and minimized cross-contamination risk during ALI culture.

In the key step of this method, NCI-H441 cells were seeded on the underside of 96-well Transwell inserts without plate inversion or removal of the inserts from the underlying plate by manipulating cell culture media density so that cells float to contact the underside of the membrane (**Figure 4-1(A)**). To increase the medium density, we chose OptiPrep (STEMCELL™ Technologies). OptiPrep is a commercially available solution of 60% w/v iodixanol in water with a density of 1.32 g/mL. Since it is typically used for density-gradient cell separation, it is iso-osmotic, non-ionic, non-toxic and metabolically inert¹⁴¹. Then, we reasoned that because the average density of a single cell is close to 1.10 mg/mL¹⁴², a solution with density of ~1.16 mg/mL, composed of 50% OptiPrep and 50% culture media, would be great enough to exceed the cells' density but provide enough media for cells to survive the required 2 hour attachment period. This formulation was highly effective, and optimization was not required.

The homogeneous, dense cell culture solution causes NCI-H441 cells to float and contact the underside of the Transwell membrane, where they adhere over a 2-hour period (**Figure 4-1(E)**). After attachment, the dense medium is diluted by adding regular cell culture medium to give an approximately 1.7:1 ratio of regular to dense media. Following 24 hours, the OptiPrep-containing media is replaced by regular media and the endothelial cell layer is seeded on the top of the membrane to form a bilayer co-culture model of the small airway-capillary barrier. Notably, the underside seeding method is automatable, and we could perform 96-well seeding using the commercially available Viaflow-96 liquid handling system.

This novel epithelial seeding method consistently generates monolayered, confluent epithelium with co-cultured endothelium that reaches an average peak TEER in co-culture of $521 \Omega \cdot \text{cm}^2$ on Day 7 of ALI (S.D. 208.35, 95% CI 481.88-560.26) (**Figure 4-4(A)**) and sodium fluorescein (NaFL) permeability of $7.04 \times 10^{-6} \text{ cm/s}$ (S.D. 1.63×10^{-5} , 95% CI 1.53×10^{-6} – 1.25×10^{-5}) (**Figure 4-5(B)**).

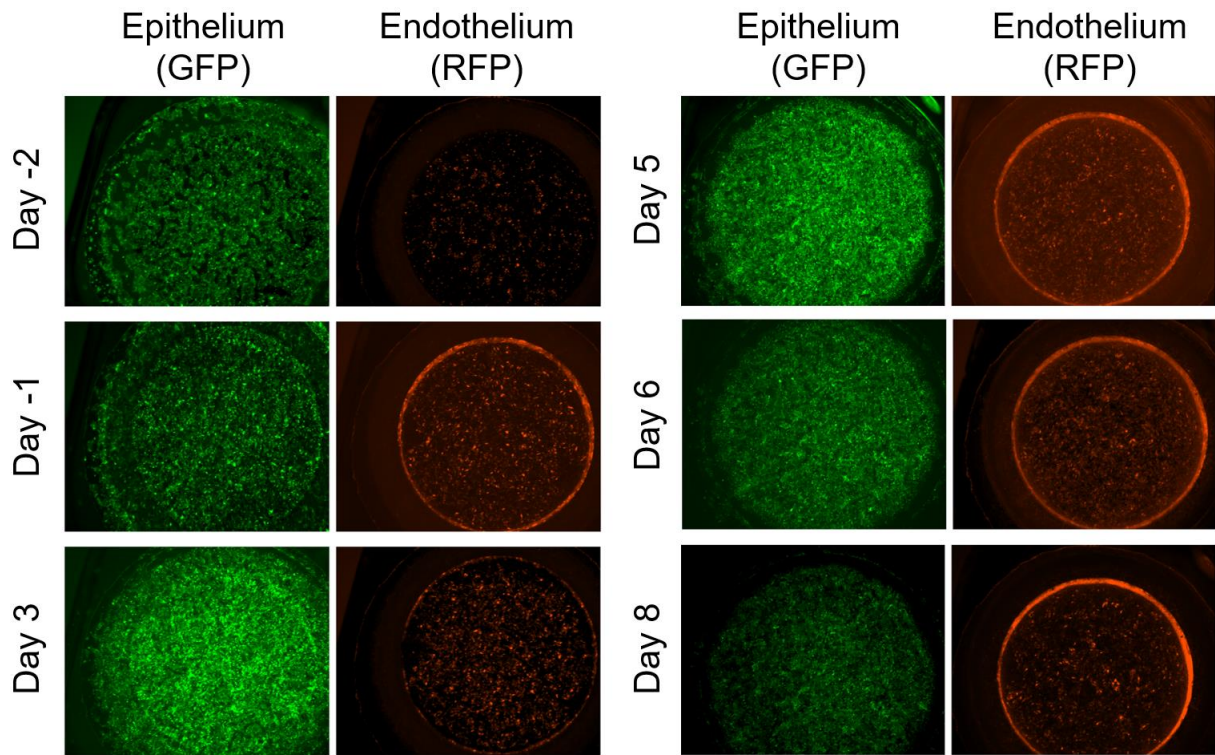


Figure 4-2 GFP- H441s (green) and RFP- HUVECs (orange) in co-culture

The epithelium is seeded on Day -3 and endothelium is seeded on day -2. ALI begins on Day 0. Day 3-Day 8 shows the progression to a culture area limited to that shared with the upper compartment due to ALI culture conditions.

4.3.2 *Bilayer co-culture exhibits polarization and differentiation of epithelial cells in co-culture with primary endothelium*

NCI-H441 cells in co-culture with HUVECs were differentiated at ALI in serum-free medium containing Ultrosor™ G (Sartorius) serum substitute to promote polarization. After 5 days of ALI, the epithelium showed differentiation and polarization indicated by the robust expression of tight junctional proteins ZO-1 localized at the air interface, and E-cadherin lining the entire cell-cell junction (**Figure 4-4(C)**). The co-cultured endothelium also lined cell-cell junctions with the adherens junctional protein VE-cadherin. All wells typically reached confluence on both sides of the membrane according to observation by fluorescence microscopy of GFP- and RFP-expressing cell layers. The variation in TEER that we observed is consistent with similar models models^{106,126,138}. Despite some TEER variation, almost all wells (average of 93/96 wells, or 97%) in every experiment reached the threshold for acceptable barrier function, defined as $285 \Omega \cdot \text{cm}^2$ (**Figure 4-4(B)**). This threshold was determined through observation that an epithelial-endothelial co-culture was confluent if its TEER was greater than $250 \Omega \cdot \text{cm}^2$. Below this value, some wells were not completely confluent. This quality control metric showed quantitatively that wells were confluent and possessed barrier function after seven days of ALI culture.

Epithelial-endothelial co-culture, in comparison to NCI-H441 and HUVEC cell monocultures, demonstrated statistically elevated TEER ($p < 0.001$, Student's t-test) for the entire culture period from days 0-10. In co-culture, TEER peaks at day 7 for an average maximum value of $521 \Omega \cdot \text{cm}^2$ (S.D. 208.35, 95% CI 481.88-560.26) (**Figure 4-4(A)**) and permeability of NaFL reaches $7.04 \times 10^{-6} \text{ cm/s}$ (S.D. 1.63×10^{-5} , 95% C.I. 1.53×10^{-6} – 1.25×10^{-5}). Comparatively, NCI-H441 cell monoculture TEER peaks on day 7 at $226.99 \Omega \cdot \text{cm}^2$ (S.D. 7.15, 95% CI 228.63–225.34) and HUVEC monoculture peaks on day 10 at $30.35 \Omega \cdot \text{cm}^2$

(S.D. 3.12, 95% CI 28.0–32.7) (**Figure 4-4(A)**). These barrier function values are consistent with similar reported Transwell co-culture models^{112,117,118,138,143}. This synergistic TEER elevation in co-culture suggests that, similar to the physiologic case, the co-cultured endothelium influences epithelial barrier strength. The increased TEER could also be caused in part by NCI-H441 cells growing into the pores to contact the endothelium (**Figure 4-3**). This epithelial growth into the pores has been observed in similar pulmonary epithelial-endothelial co-culture models cultured on microporous inserts^{124,144,145}. This interaction is thought to enhance epithelial-endothelial communication in a physiologically relevant manner by allowing the production of heterogeneous gap junctional complexes¹²⁴.

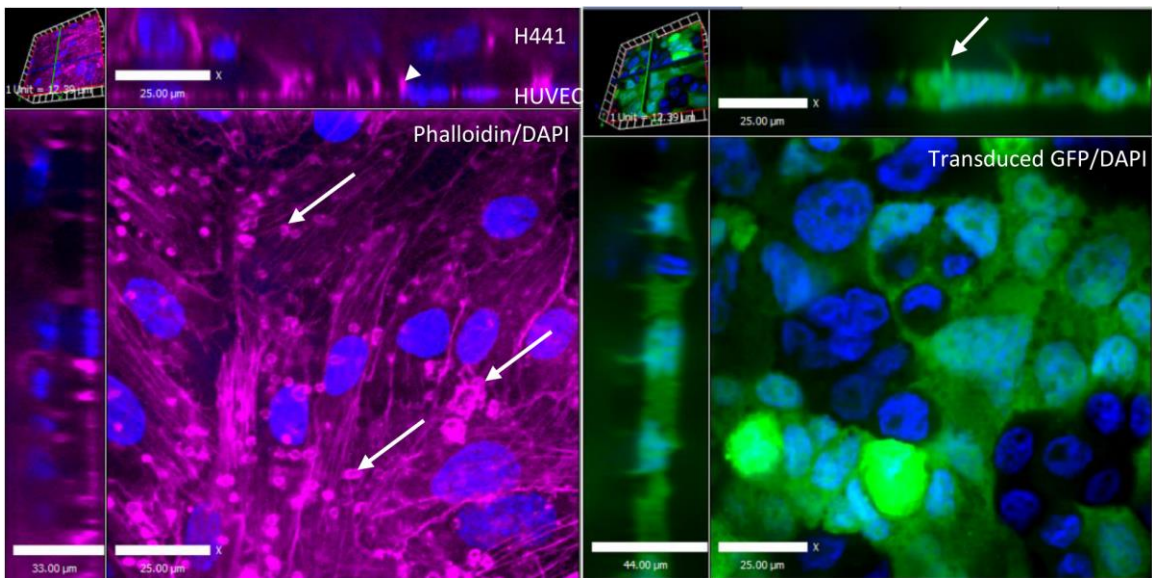


Figure 4-3 NCI-H441 cells grow into the membrane pores to contact the endothelium.

Left, F-actin stain with phalloidin shows the endothelial layer with interspersed epithelial cell protrusions (arrows). The top cross-section shows the NCI-H441 layer on top, endothelial layer on the bottom, with protrusions extending between the layers (arrowhead). Right, GFP-expressing NCI-H441 cells in co-culture grow protrusions through the membrane pores (arrow). Images taken by confocal microscopy.

Table 2. Seeding success rate

Run	Met Standard	Total Seeded	% Success	
A	91 wells	96 wells	94.8	%
B	93 wells	96 wells	96.9	%
C	93 wells	96 wells	96.9	%
D	95 wells	96 wells	99.0	%
		AVG	96.9	%
		STDEV	1.5	%
		95% CI	2.0	%

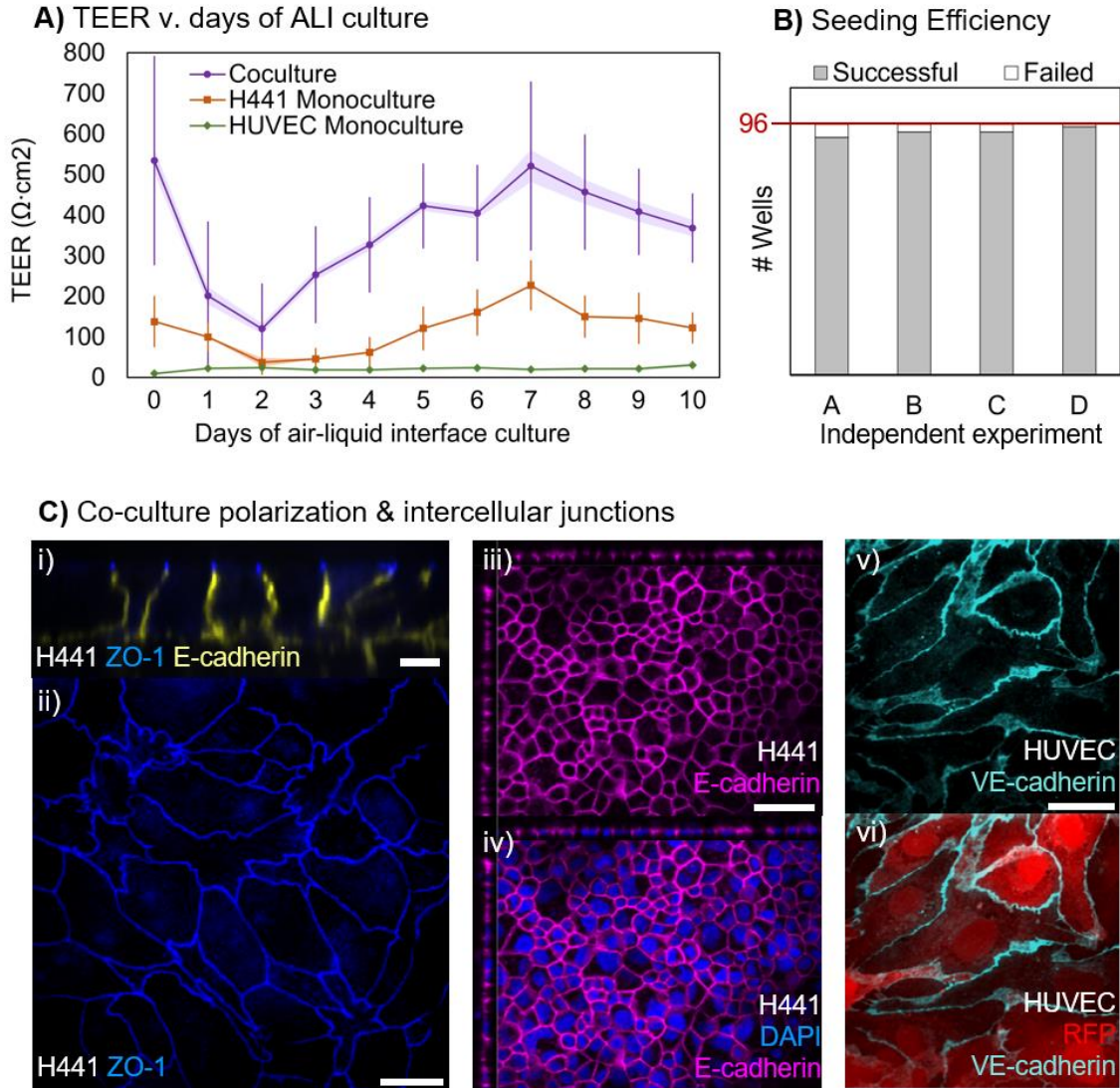


Figure 4-4. Co-cultured NCI-H441 cells and HUVECs show polarization and differentiation under ALI culture with serum-free medium.

*A) Co-cultured H441-HUVEC bilayers exhibit synergistically elevated TEER ($p < 0.05$, Student's t -test) compared to both monocultures during 10 days of ALI culture. Vertical lines indicate standard deviation; shaded lines indicate 95% confidence interval. $n = 72$, coculture; $n = 49$, NCI-H441 monoculture; $n = 9$, HUVEC monoculture. **B)** In 4 independent seeding experiments, seeding efficiency was close to 97%, meaning that on average, 93 of 96 wells met quality control criteria. Successful wells are defined as those meeting the criteria: TEER $> 286 \Omega\text{-cm}^2$ on Day 6 of ALI culture; confluent NCI-H441 and HUVEC monolayers determined by visual inspection; retention of medium in the top compartment without leakage, also determined by visual inspection. **C)** NCI-H441 cells in co-culture with HUVECs at ALI develop appropriate cellular junctions indicating barrier formation. **i)** NCI-H441 cells demonstrate polarization of the epithelium by ZO-1*

*localization at the apical air-cell boundary (blue) with intercellular e-cadherin indicating formation of adherens junction complexes (yellow). Scale bar, 10 μ M. **ii**) ZO-1 (blue) tight junction stain on co-cultured, ALI-differentiated NCI-H441 cells indicates robust intercellular barrier formation. Scale bar, 25 μ m. **iii, iv**) E-cadherin staining in co-cultured NCI-H441 cells indicates robust intercellular barrier formation and epithelial monolayer. Scale bar, 50 μ M. **v, vi**) Co-cultured HUVECs express adherens junctional protein VE-cadherin, indicating formation of an endothelial barrier. Scale bar, 25 μ m. Images representative of at minimum $n = 3$ independent wells per stain.*

4.3.3 Epithelial exposure to viral and bacterial mimics induces endothelial inflammation and barrier loss

Exogenous stimuli such as pathogens can initiate systemic pathophysiology through the propagation of epithelial insult to the endothelium, and the resulting communication of inflammatory signals into the bloodstream where they can travel systemically^{110,146}. To demonstrate the utility of the model for studying this phenomenon, we tested if the air-blood barrier model can recapitulate the transfer of inflammatory signals from the epithelium to endothelium during epithelial exposure to viral mimic and live viral pathogens. We first exposed the epithelial side of the bilayer to the viral RNA mimic polyinosinic:polycytidylic acid (poly(I:C)) for 10 minutes, and showed that the endothelium immediately exocytoses von Willebrand factor (vWF), a pro-coagulant macrostructured glycoprotein that assembles on the endothelial surface in response to inflammatory stimuli to aggregate platelets and attract immune cells. Such immediate vWF release has been reported previously upon direct stimulation of the endothelium with poly(I:C)¹⁴⁷.

To demonstrate barrier function in response to a viral or bacterial mimic, NCI-H441 cells in co-culture were exposed to poly(I:C) or lipopolysaccharide (LPS, component of gram-negative bacterial membranes) at 2 doses each for 24 hours. While LPS at 1 μ g/mL

did not induce an increase in permeability, LPS at 20 $\mu\text{g}/\text{mL}$ did (**Figure 4-5(B)**). Permeability of NaFL was measured after 24 hours of poly(I:C). Both 1 and 10 $\mu\text{g}/\text{mL}$ induced permeability increase. Permeability of the control bilayer co-culture was $7.04 \times 10^{-6} \text{ cm/s} \pm 0.163 \times 10^{-6} \text{ cm/s}$ measured by NaFL over a 3-hour period (**Figure 4-5(B)**). Overall, 2 of the 4 exposure conditions resulted in statistically significant increases in permeability compared to the controls that received no exposure and remained at ALI; $n = 3$ per condition; $n = 4$ for controls. Analysis was performed with 1-way ANOVA with post hoc Tukey's t-test (GraphPad Prism).

4.3.4 Epithelial viral exposure induces dose-dependent inflammatory signals in epithelial-endothelial co-culture

We exposed the epithelial NCI-H441 cell layer to influenza A virus (subtype H1N1, strain A/Puerto Rico/8/1934) and human beta-coronavirus (HCoV-OC43) in cell culture media for one hour before returning the epithelium to ALI. This allowed the virus to attach while maintaining the epithelium at ALI over the 3-day influenza. Infection of the epithelium by influenza A virus and human beta-coronavirus results in dose-dependent endothelial production of leukocyte chemoattractant IL-8 after 72 hours, indicating that epithelial infection leads to endothelial induction of the appropriate inflammatory response (**Figure 4-5(A)**). Of note, after 72 hours, none of the wells had lost ALI (no media leaked through to the bottom well). This proof-of-concept experiment demonstrates the feasibility of detecting MOI-dependent responses in the co-culture system and the capability to enable parallel screening of a multiplicity of conditions with one plate.

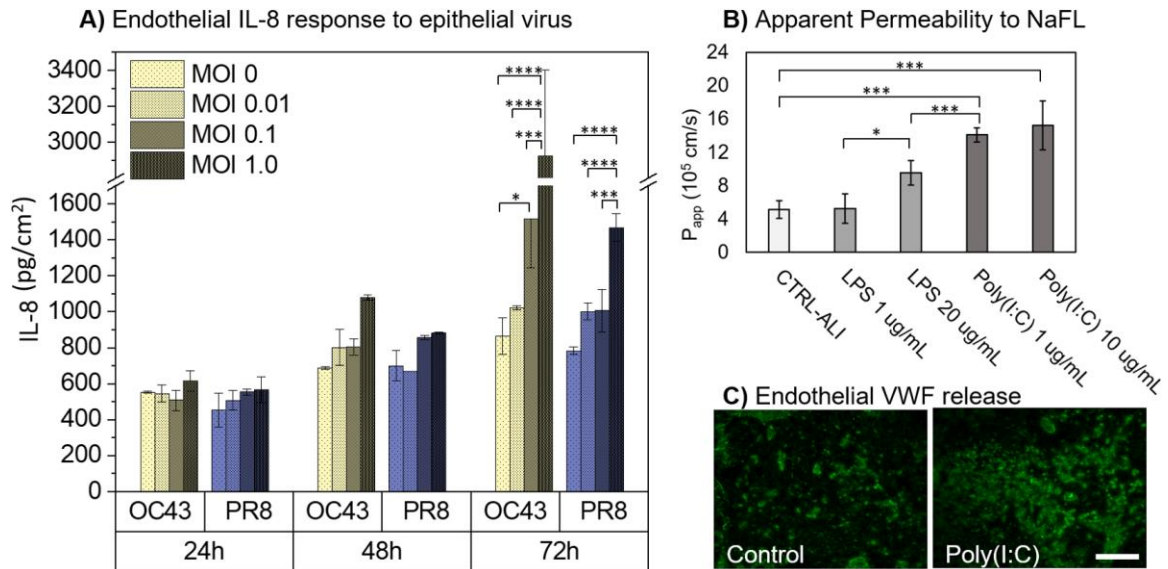


Figure 4-5. Epithelial-endothelial signal propagation and barrier loss.

A) Exposure to influenza A virus (PR8) and human beta-coronavirus (OC43) at four multiplicities of infection (MOI) results in MOI-dependent increase in endothelial IL-8 production under ALI conditions over 72 hours. $n = 3$ technical replicates per condition. Independent replicates for each day. **B)** NCI-H441 cells in co-culture were exposed to poly(I:C) or LPS at 2 doses each for 24 hours. Permeability of NaFL was measured after 24 hours of exposure. LPS and poly(I:C) increased permeability in all cases except low-dose LPS. Error bars represent standard deviation. $n = 2-3$ replicates per condition; $n = 4$ for controls. Error bars represent standard deviation. $n = 3$ biological replicates per condition. **C)** Co-cultures that were exposed on the epithelium to viral or bacterial mimics poly(I:C) for 10 minutes induced endothelial release of von Willebrand Factor, linking epithelial stimulation and endothelial activation in our co-culture model. Images are representative of the entire cell layer. Scale bar, 200 μ M. For all graphs: . * $p < 0.05$, *** $p < 0.0001$, **** $p < 0.00001$, Two-way ANOVA with post hoc Tukey's t -test (GraphPad Prism 8).

4.3.5 Epithelial aerosol exposure induces dose-dependent ROS and IL-8 response

To further demonstrate the utility of this culture model for the high-throughput investigation of physiological disease stimuli, we studied the impact of secondary organic aerosol (SOA). SOA is particulate matter in the atmosphere that is formed by the oxidation of aerosolized organic material¹⁴⁸. Particulate matter exposure is associated with increased incidence of various respiratory illnesses¹⁴⁹. The contribution of SOA to health risks is not

fully understood, but it is known that SOA exposure to the airway epithelium can induce the production of reactive oxygen species^{149–151}.

The epithelial cell side was treated with the ROS probe Carboxy-H2DCFDA (ThermoFisher, C400), then the epithelial side was exposed to different types of SOA suspensions at the concentrations designated in the graphs for 2 hours (n=4 per condition). Production of reactive oxygen species (ROS) was measured through increase in mean fluorescence intensity (MFI) of the fluorescent ROS reporter carboxy-H2DCFDA. Two-way ANOVA showed no significant effect of SOA type on ROS production but significant effect of dose ($p < 0.0001$). Multiple comparisons using post-hoc Tukey's t-test identified significant differences between SOA suspension concentrations. (Right) The epithelial side was treated with SOA for 24 hours. Then, IL-8 produced on the endothelial side was measured by ELISA (R&D Systems). Two-way ANOVA showed effect of both SOA type ($p < 0.0001$) and dose ($p < 0.0001$) on IL-8 production. Multiple comparisons with Tukey's post hoc t-test showed significant differences between dose for a given SOA. We monitored the production of epithelial SOA using live cell fluorescence imaging of the ROS reporter (carboxy-H2DCFDA). We found that both oxidation states of SOA dose-dependently increased the generation of epithelial ROS and endothelial IL-8. However, the dry SOA was less potent at generating endothelial IL-8 than the humid SOA.

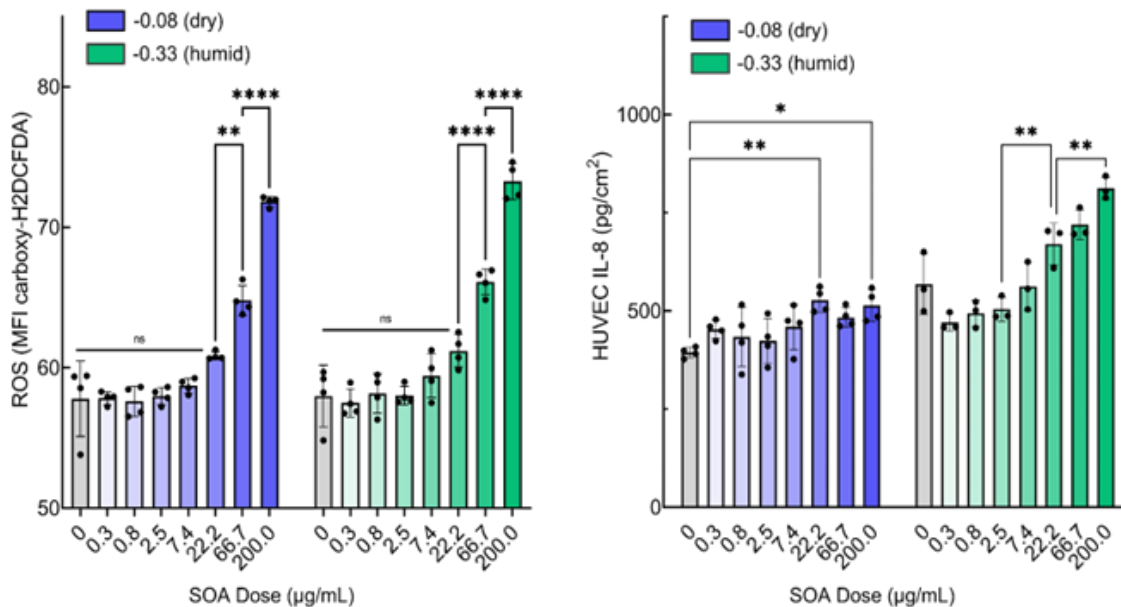


Figure 4-6. ROS and IL-8 production after SOA exposure.

A) Epithelial ROS generation after epithelial secondary organic aerosol exposure after 30 minutes. **B)** IL-8 production by the endothelium after 24 hours of epithelial exposure to secondary organic aerosol. For both graphs: * $p < 0.05$, ** $p < 0.01$, *** $p < 0.001$, **** $p < 0.0001$. Statistics were performed in GraphPad Prism 9.

4.4 Discussion

In this work we exploited density-driven cell buoyancy to enable underside attachment without the inversion of the culture membrane, therefore enabling semi-automated culture in a high-throughput 96-well platform. As a demonstration of this underside seeding method, we constructed a co-culture model of the distal lung air-blood barrier. This region is heavily involved in the mediation of inflammatory responses during toxin and pathogen exposure⁵. Successful barrier maintenance in this region is critical to prevent acute lung injury from developing after insults or infection. We showed that upon stimulation of the epithelial side of the engineered ABBA with bacterial or viral insults, the apposing endothelium exhibited prothrombotic (vWF release) and proinflammatory

(IL-8 secretion) responses. The many wells available for testing conveniently allowed comparison of the effect of different viruses, MOI, and time points. We also showed that epithelial exposure to SOA induced endothelial IL-8 and epithelial ROS dose-dependently.

Our model enhances the capabilities introduced by previous respiratory culture systems by offering multiplexing capability for high-throughput applications in a co-cultured, an ALI differentiated platform that can be generated using automated methods. Previous lung culture models have incorporated ALI culture^{106,134}, bilayer co-culture^{118,119,125,126,152}, and/or high-throughput capability^{104,105,133}, but few if any include these in one platform, and none utilize an automatable underside seeding method to our knowledge¹⁰⁷. Notably, we are unaware of any other co-culture model offered at the 96-well scale that does not require custom equipment, presumably due to the unique challenges presented by this small culture area for underside seeding¹³³. Finally, we consistently generate a monolayered epithelium covering the entire culture area, despite reports that NCI-H441 can form multilayers at high seeding densities comparable to mine^{125,134}. we postulate that this underside seeding method facilitates the formation of a monolayer during initial attachment by allowing even cell spreading compared to seeding on the top side of a Transwell or confining the cells to a droplet during underside seeding.

Additionally, while this application to cell attachment is novel, density-driven buoyancy has been used previously for cell manipulation. Buoyancy is often exploited for density-gradient separation of cells and extracellular vesicles, and it has been used to generate scaffold-free tissue constructs such as substrate-free cell sheets¹⁵³ or spheroids¹⁵⁴. Chandrasekaran et al. used buoyancy to culture cell rafts at ALI¹⁵⁵. This application

complements these previous methods by enabling high-throughput, robust cell attachment on the underside of a surface.

The functional responses demonstrated in this model are similar to those achieved in lower-throughput co-cultured Transwell systems. Previous models have demonstrated the loss of TEER and increase in permeability in response to viral and bacterial mimics, and endothelial expression of IL-8 and other cytokines by the endothelium in response to epithelial insults including LPS¹¹², virus¹¹⁸, pro-inflammatory cytokines¹⁴³, particles¹²⁶, and toxins¹²⁰. However, few if any *in vitro* co-culture models have demonstrated that epithelial stimulus can induce endothelial release of vWF by the co-cultured endothelium, although this response is observed *in vivo*¹⁵⁶. Additionally, while co-culture models have shown that the epithelium and endothelium secrete IL-8 in response to PR-8 virus, there are no prior data, to our knowledge, showing that IL-8 production on the endothelium increases proportionally to the MOI, although such a scaled response is expected for the influenza A virus infecting the epithelium^{118,157,158}. Finally, this model is the first co-culture system to our knowledge to utilize a serum replacement for ALI differentiation. Previous co-cultured ALI models have included serum and used dexamethasone to promote polarization and tight junction formation^{117,143}. The elimination of serum and glucocorticoids for ALI differentiation increases the inter-well reliability and more faithfully recapitulates cellular responses to inflammatory stimuli. Overall, this model enhances the capabilities of co-culture to include the standardized testing of large condition sets in a physiologically relevant system.

This culture platform is ideal for the investigation of large condition sets, particularly in the study of toxins and therapeutic candidates. Indeed, there is growing

interest in the adaptation of barrier models to cell types with greater physiologic relevance^{104,159}. The current standard for early-stage cell-based screening is Vero cells or MDCK cells that are far removed from the tissue physiology and may not reflect the true performance of drug candidates *in vivo*¹⁶⁰. This platform enables facile automation of a physiologically relevant pulmonary barrier model for enhanced screening. Further, the position of the endothelium facing downwards poses an advantage for exposure testing. Rather than flowing aerosols downward into each concave well for exposure, we can simply flow aerosols past the underside of the exposed epithelium. This simplifies the requirements for an automated exposure system.

This model is limited in several ways. First, it does not yet include resident or circulating immune cells. Other models have added tissue-resident macrophages to the epithelium, mimicking the alveolar macrophages found in alveoli and respiratory bronchioles^{125,126,161}. Resident and circulating immune cells play a central role in the response to inflammatory insults and potentiate barrier function in response. Future iterations of this model will include immune cells. Leveraging the convenient placement of the epithelium facing downwards, immune transmigration with neutrophils, monocytes or other immune cells is feasible in this model. Note that we utilize a 3- μm Transwell pore size that was permissible to neutrophil migration in a related co-cultured airway model¹⁵². An additional limitation is the Transwell culture substrate. The distal airway epithelium is normally separated from the capillary endothelium by a lining of smooth muscle and a thin connective tissue layer composed of collagen fibers (lamina propria). Smooth muscle cells and the physical separation between cell types are not recapitulated in this model. Further, the plastic Transwell filter does not represent the true connective tissue separating the cell

types *in vivo*. However, similar barrier function and response to stimuli were recreated in this relatively simple model.

More broadly, epithelial-endothelial tissue barriers control access to the bloodstream at a variety of tissue sites including the respiratory tract and the mucosal barriers of the nasal passage, intestine, and eyes. This seeding method should be readily applicable to models emulating these other mucosal sites, as well. Different cell types may require tuning of the ratio of Optiprep to cell culture media. Here we used a 50/50 split by volume because it was well tolerated by the epithelial cells and resulted in near 100% flotation during the 2-hour culture period. However, 50/50 results in a density of 1.16 g/mL and a relatively increased liquid viscosity that may injure sensitive cell types. As most cells' density is close to 1.10 g/mL, a greater media:Optiprep ratio may still prove effective for more delicate cell types that need more media and lower viscosity to be successfully used in this method.

In conclusion, we propose that bilayer co-culture enhances the physiological relevance of many high-throughput tissue barrier models. However, the broader adoption of bilayer co-culture systems has been hampered by the difficulty of seeding cells on the underside of the membrane, a procedure that requires inversion of the membrane inserts and is particularly difficult in plates featuring 96- or more wells. In this study, we demonstrate that a robust co-culture model of the small airway epithelial-endothelial barrier can be produced at the 96-well scale using a robotic liquid handler-compatible procedure that circumvents the need for plate inversion during cell seeding by using high efficiency (>97%) attachment by density-driven cell flotation instead. This method

enhances the convenience of high-throughput co-culture to increase physiologic relevance of tissue barrier models for high-throughput screening.

CHAPTER 5. HIGH-THROUGHPUT DOSE-RESPONSE ANALYSIS OF DISTAL LUNG NEUTROPHIL INFILTRATION AND ACTIVATION

5.1 Introduction

Typically, neutrophils are the first immune cells to infiltrate the lungs during infection or injury^{67,162}. Neutrophils are innate immune cells that comprise the bulk of circulating white blood cells and are poised to detect localized distress signals in the form of chemoattractant gradients^{163,164}. Neutrophils migrate from the bloodstream to the injury site where they respond quickly and aggressively to clear pathogens, remove debris, and secrete pro-inflammatory and pro-regenerative mediators¹⁶⁵. These early actions set the stage for later tissue repair and re-establishment of homeostasis. However, dysregulated neutrophil activity can instead exacerbate tissue injury and interrupt repair^{165,166}. Neutrophils contribute to pathogenesis and perpetuate distal lung tissue injury in conditions ranging from the acute (e.g., acute respiratory distress syndrome¹⁶⁷, acute lung injury¹⁶⁸, and viral lower respiratory infection¹⁶⁹⁻¹⁷¹), to the chronic (e.g., chronic obstructive pulmonary disease⁶⁹, asthma⁷⁰, and CF¹⁷²⁻¹⁷⁴). In these and other conditions, dysregulated neutrophils infiltrate and damage the distal airways and alveoli, compromising overall lung function^{73,162,175,176}.

Consequently, controlling neutrophil-driven pathophysiology is a top priority across a multitude of inflammatory lung diseases^{173,177-180}. Clinical studies of available anti-inflammatory therapeutics, namely glucocorticoids and statins, have suggested an effect at improving clinical outcomes (pulmonary function, time to intubation, mortality) in various inflammatory lung diseases^{66,181-184}. *In vitro* evidence corroborates that

neutrophil chemotaxis may be affected by statins and glucocorticoids^{66,185}. However, the evidence for glucocorticoid and statin efficacy is relatively modest, comprising primarily retrospective analyses, population-based studies, and preclinical studies, so the final verdict on their use in inflammatory lung disease is inconclusive^{186–190}. Further, both drugs exhibit pleiotropic effects on a host of signaling pathways and biologic functions that can lead to harmful side effects^{186,191–193}. Therefore, novel inflammation-modulating therapeutic strategies are in development¹⁹⁴, including targeted small molecule inhibitors^{195–197}, micro- and nano-particles^{198,199}, monoclonal antibodies²⁰⁰, bioactive peptides²⁰¹, and engineered nucleic acids²⁰².

These efforts are hampered by the significant limitations in current preclinical testing modalities for predicting in-human efficacy of drug candidates. Animal models are preferred for assessments of pulmonary neutrophil modulation because they enable measurement of critical outcomes including air-blood barrier strength and degree of immune cell infiltration and activation in a disease-relevant tissue microenvironment^{203,204}. However, precise quantitation of infiltrated immune cells is challenging, and the effect of other cell types in the microenvironment on the final phenotype is difficult to isolate²⁶. Further, animal models have limited throughput and significant species-specific differences on the organ-, cell- and molecular-level that could affect drug candidates' efficacy^{41,205}. Finally, animals cannot reflect patient-specific responses to a given therapeutic, an emerging goal of personalized medicine²⁰⁶.

Therefore, human cell-based *in vitro* platforms have been developed to model neutrophil migration and activation. Traditional *in vitro* models with human cells have used cell culture inserts to incorporate bilayer epithelial-endothelial co-culture^{144,207}, air-liquid

interface culture²⁰⁸, and induction of disease-specific neutrophil phenotypes¹⁷³ to create physiologic relevance (**Table 3**). However, these platforms are typically low throughput (6- to 24-well plate) and require large volumes of primary cells and lung fluids that can be difficult to obtain in large volumes, especially in infants and children²².

Table 3. Summary of Previous Transmigration Assays

Article	Year	Format	Through-put (wells per plate)	Epithelium	Endo-thelium	TEER	ALI	Neutrophil phenotype
Cramer et al. ²⁰⁹	1980	Transwell	12	X		X		
Casale et al. ²¹⁰	1990	Transwell	24	X	X			
Liu et al. ²¹¹	1996	Transwell	12	X				
Casale & Carolan ²⁰⁷	1999	Transwell	24	X	X			
Kidney & Proud ²⁰⁸	2000	Transwell	12	X		X	X	
Mul et al. ¹⁴⁴	2000	Transwell	12	X	X			
Hu et al. ²¹²	2005	Transwell	24	X	X			X
Huh et al. ²¹³	2010	Microfluidic	N/A	X	X			
Kusek et al. ²¹⁴	2014	Transwell	24	X				
Yonker et al. ²¹⁵	2017	Transwell	24	X			X	
Forrest et al. ¹⁷³	2018	Alvetex	24	X			X	X
Mejias et al. ²¹⁶	2020	Microfluidic	6	X	X		X	
Nawroth et al. ¹⁵²	2020	Microfluidic	N/A	X	X		X	
This work	2022	Transwell	96	X	X	X	X	X

Therefore, lung microphysiological systems (MPS) have emerged to unite human relevance and organ-level functions *in vitro* in miniaturized platforms that require very small volumes and cell numbers²¹⁷. Microphysiological systems (MPS) are advanced *in vitro* culture platforms that mimic human tissue-level function and microenvironment by incorporating factors such as co-culture, three-dimensional geometry, cell migration, and mechanical cues^{1,42}. MPS enable studies of human-relevant physiology and cell-cell

interactions in a tightly controlled, replicable environment. Thus, they are uniquely poised to study inflammation, which is the process of immune cell infiltration and activation at a site of tissue injury, infection, or disease. Inflammation is tightly regulated by cell-cell interactions and signaling and develops unique signatures under different disease conditions. MPS could therefore recreate disease-specific inflammation under controlled conditions for studying pulmonary pathophysiology and testing therapeutics. Several microfluidic MPS modeled neutrophil transmigration into the distal lungs, but outcome measures have thus far been limited to image-based quantitation and velocity measurements^{130,152,216,218–221}. Microfluidic immune transmigration models have consistently reported low transmigrated cell yields ($10 - 10^3$ cells/device) that preclude standard analysis with flow cytometry and limit cell population-level insights. Further, to date, microfluidic platforms are technically demanding and costly to standardize, scale, and automate^{222,223}.

To enable detailed and high-content screening-compatible neutrophil transmigration studies, a mesoscale approach is required that incorporates advantages of both traditional macroscale and novel microscale culture models. Here, we report the use of a small-volume, 96-well format epithelial-endothelial bilayer neutrophil transmigration assay. The platform incorporates multifaceted quantitative readouts, including migrated neutrophil number and activation state with flow cytometry, quantitative epithelial or endothelial immunofluorescence, and barrier strength measurements based on trans-epithelial/endothelial electrical resistance. By migrating neutrophils towards primary CF patient sputum-derived airway liquid supernatant (ASN), the model reproduces CF lung disease with regards to neutrophil recruitment, dysfunctional activation, endothelial e-

selectin, and barrier property changes. Finally, the assay generates dose-response curves comparing transmigration inhibition efficacy for clinically available immunomodulators, JAK-inhibitor baricitinib and NF- κ B modulator dexamethasone.

5.2 Materials and Methods

5.2.1 Preparation of air-blood barrier array (ABBA)

The 96-well lung ABBA was prepared as previously reported by our group¹⁰⁰. Briefly, we modeled the epithelium by seeding the human small airway-like epithelial cell line NCI-H441 (American Type Culture Collection (ATCC)) on the underside of the Transwell membrane. This cell line recapitulates key properties of distal lung epithelium without introducing donor-dependent variability that could influence assay replicability. The endothelium was modeled with primary human umbilical vein endothelial cells (HUVECs, ATCC) that were pooled from multiple donors to reduce donor-specific variation.

5.2.2 Neutrophil transmigration assays

Human peripheral blood was obtained through venipuncture. All protocols for blood collection and processing were approved by the Institutional Review Boards of Georgia Institute of Technology and Emory University. Neutrophils were isolated according to manufacturer instructions (Miltenyi Biotec 130-104-434, and 130-098-196). Trans-epithelial electrical resistance was measured as previously described¹⁰⁰. Chemoattractants (leukotriene B₄, Cayman Chemical #20110; Interleukin 8, MyBioSource

#MBS9718666) were prepared at the specified concentrations in air-liquid interface (ALI) media. ALI media was prepared as described in Viola 2021. In CF assays, pooled patient airway supernatant was prepared as described²²⁴, diluted in ALI media, and placed in the receiver plate. In drug testing assays, isolated neutrophils were suspended in media containing specified drug concentrations (baricitinib, Cayman Chemical #16707; dexamethasone, Millipore Sigma #D2915-100MG). Media was completely removed from the top chamber of the Transwell inserts and neutrophils suspended in air-liquid interface medium were placed in the top chamber of the Transwell at 100 μ L/well, with 225,000-330,000 cells/well depending on the experiment. Conditions that were directly comparable used the same number of neutrophils in the top well. After neutrophils were placed in the top chamber, inserts were placed immediately into pre-warmed receiver plate containing the chemoattractant or patient sample. The plate was incubated for 16 hours at 37 °C, 95% humidity, 5% CO₂.

5.2.3 *Flow cytometry*

Freshly isolated neutrophils (hereafter called blood neutrophils) were stained for flow cytometry in a FACS tube immediately after isolation from whole blood. Transmigrated neutrophils were collected into non-tissue culture treated round-bottom 96-well plates for staining. All reagents were kept at 4 °C, incubations took place at 4 °C in the dark and all centrifugations were at 400g for 5 minutes at 4 °C or 25 °C. Washes consisted of 3 repeats of the following: diluting the suspension to 300 μ L with PBS+2.5 mM EDTA (pH 8), centrifugation, and aspiration of half the supernatant (150 μ L). To stain neutrophils, cells were collected from the receiver plate, washed, and pre-stained for 10 minutes with 1:500 Live/Dead (Biolegend 423102) and 1:100 Human TruStain FcX

(Biolegend 422302) in PBS-EDTA for 10 minutes. Cells were washed and incubated in the antibody cocktail for 30 minutes, containing the following antibodies at 3 μ L per antibody plus PBS-EDTA for a total volume of 200 μ L per well: Alexa Fluor® 647 anti-human CD63 (Biolegend 353016); PE/Cyanine7 anti-human CD66b (Biolegend 305116); APC/Cyanine7 anti-human CD16 (Biolegend 302018) ; Brilliant Violet 421™ anti-human CD62L (Biolegend 304828) (**Table 4**). Then cells were washed and fixed in 2% PFA for 5 minutes followed by washing and resuspension in PBS-EDTA. Stained neutrophils were stored at 4 °C protected from light until measurement on the Beckman Coulter Cytoflex S within 3 days of staining. Flow cytometry was performed using the Beckman Coulter Cytoflex S at 30 μ L/min collection speed. Compensation was collected using single-antibody stained Abc Beads for antibodies and Arc beads for live/dead according to manufacturer instructions. Gating and compensation matrix was performed in FlowJo. Cells were gated first SSC-A vs. SSC-H for singlets, then SSC-A vs KO525 for live cells. Cell quantitation and MFI were calculated using FlowJo. An example gating strategy is shown in **Figure 5-1**. The same gate was applied to all samples of the same experiment. New gates were applied for each experiment.

Table 4. Flow cytometry antibody list

Target	Color	Vendor	Catalog #	Product Name	Antibody Type
CD63	AlexaFluor 647	Biolegend	353016	Alexa Fluor® 647 anti-human CD63	Mouse IgG1, κ
CD66B	PE-Cy7	Biolegend	305116	PE/Cyanine7 anti-human CD66b	Mouse IgM, κ
CD16	APC-Cy7	Biolegend	302018	APC/Cyanine7 anti-human CD16	Mouse IgG1, κ

CD62L	Brilliant Violet 421	Biolegend	304828	Brilliant Violet 421™	Mouse IgG1, κ anti-human CD62L
-------	----------------------	-----------	--------	-----------------------	--------------------------------

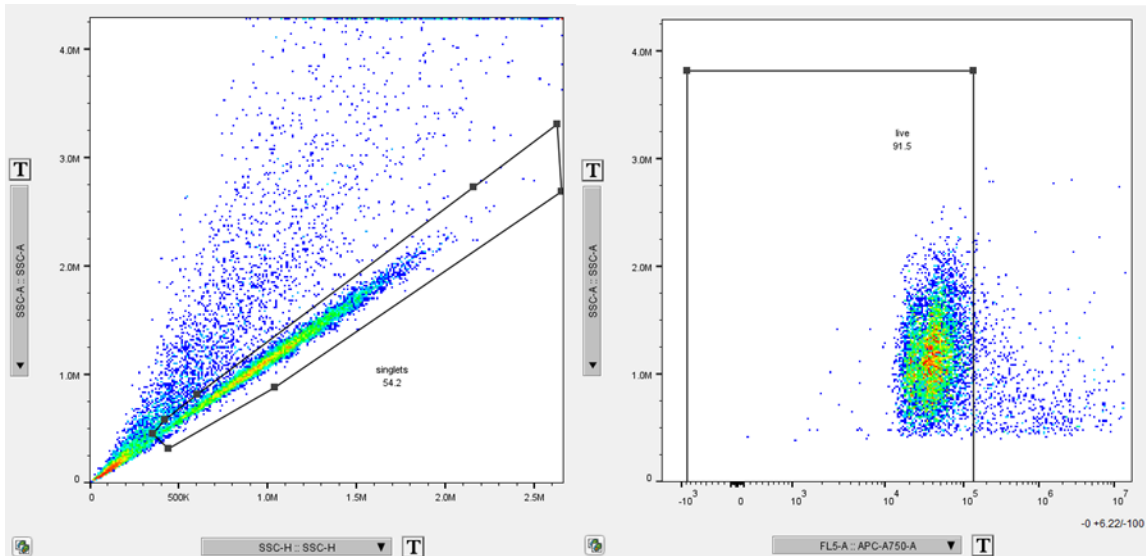


Figure 5-1 Gating strategy for neutrophil flow cytometry

Raw data collected by flow cytometry is processed in FlowJo. Events are first sorted by SSC-A vs. SSC-H into the gate shown to isolate singlet events (left panel). This group is then gated for live cells by selecting the population of events with a dead cell stain MFI below approximately 10⁵ (right panel).

5.2.4 Statistical analysis

All statistics were performed in GraphPad Prism 9. All significance tests were performed with $\alpha = 0.05$. **Figure 5-5(C)** Student's t test, unpaired, $\alpha = 0.05$. **Figure 5-5(D)** Simple Linear regression, $\alpha = 0.05$, 95% confidence interval (dashed lines). Wald Test was used to assess whether the regression line slope was significantly non-zero. **Figure 5-5(E), 5-5(F)**: Two-way ANOVA with post-hoc Tukey's t test for multiple comparisons with $\alpha = 0.05$ (95% confidence). **Figure 5-6(A)**, right: Mixed effects analysis with row matching and post-hoc Tukey's t-test, $\alpha = 0.05$ (95% confidence). **Figure 5-6(B),(C)**: Simple linear regression, $\alpha = 0.05$, 95% confidence interval (dashed lines). Wald's test for significantly non-zero regression slope. **Figure 5-6(D-F)**: Ordinary one-way ANOVA (unmatched),

post-hoc Tukey's t-test, $\alpha = 0.05$ (95% confidence). **Figure 5-7(B-D)**: Ordinary one-way ANOVA (unmatched), post-hoc Tukey's t-test, $\alpha = 0.05$ (95% confidence). **Figure 5-7(E-H)**: Student's t test, unpaired, $\alpha = 0.05$. **Figure 5-8(A),(B)**: Simple linear regression, $\alpha = 0.05$. **Figure 5-9(A-B)**: Nonlinear least-squares regression (log₁₀[inhibitor] vs. response logistic curve, three-parameter). No handling of outliers, no constraints, no weighting, 95% confidence interval. IC₅₀ value reported from the GraphPad model. However, IC₅₀ value can be calculated from the regression model by determining the x-value associated with 50% of the difference between the minimum and maximum values of the logistic curve. For all graphs: * $p \leq 0.05$, ** $p \leq 0.01$, *** $p \leq 0.001$, ***** $p \leq 0.0001$.

5.2.5 Cell culture

NCI-H441 human adenocarcinoma cell line (H441 cells) was purchased from American Type Culture Collection (ATCC) (ATCC® HTB-174™). NCIH441 cells were expanded in RPMI-1640 (ATCC® 30-2001™) supplemented with 9% fetal bovine serum (50 mL into 500 mL media for total volume 550 mL) and Penicillin-Streptomycin (Gibco™ 15140148) diluted 1:100 v:v. For routine culture, H441 cells were seeded at density 1e6 cells per 75 cm² in 60 mL cell culture media into a T-225 tissue culture flask. After passage (day 0), media was changed every 48 hours on the following schedule: day 2, 60 mL; day 4, 120 mL; day 6, passage. For media changes, NCI-H441 media was aspirated and replaced. For passage, NCI-H441 T-75 flasks were rinsed with 10 mL warm PBS (Ca²⁺ and Mg²⁺-free) and lifted with 2 mL 0.05% Trypsin-EDTA (Gibco™ 25300120). Trypsin was neutralized with media and cells were spun down (200 g, 5 min, 25 °C), resuspended in 1 mL RPMI media and counted for seeding with Nexcelcom Cellometer Auto T4 Bright Field Cell Counter (Nexcelcom Bioscience) using Trypan Blue viability stain. Cells were

used below the 8th passage after obtaining from ATCC. Primary pooled human umbilical vein endothelial cells (HUVECs) were purchased from ATCC (ATCC® PCS-100-013™) and expanded according to manufacturer instructions in Vascular Cell Basal Medium (ATCC® PCS-100-030™) supplemented with Endothelial Cell Growth Kit-VEGF (ATCC® PCS-100-041™) with added Penicillin-Streptomycin (Gibco™ 15140148) diluted 1:100 v:v. Cells were passaged at 60-80% confluence according to manufacturer instructions, counted with Nexcelcom Cellometer Auto T4 Bright Field Cell Counter (Nexcelcom Bioscience) using Trypan Blue viability stain, and used below passage 10 since expanding from ATCC.

5.2.6 Transwell preparation

H441-HUVEC bilayer co-cultured Transwells were prepared in Corning 96 well HTS plates as previously described¹⁰⁰. NCI-H441 cells were passaged and suspended at 1.18×10^{-6} cells/mL in 37 °C culture media. The cell solution was gently mixed with sterile, pre-warmed (37 °C) 50% v/v OptiPrep Density gradient medium (STEMCELL Technologies 07820) until a homogeneous solution was observed. The solution was immediately transferred to the lower chamber of the HTS 96-well plates (85 µL/well) using a multichannel pipettor or VIAFLO-96 liquid handler, ensuring adequate mixing for even cell distribution. This concentration and volume results in 50,000 cells/well (350,000 cells/cm²). The cells adhered in this condition for 2 hours in a humid incubator at 37 °C, 5%CO₂, 95% humidity.

After 2 hours, 150 µL cell culture media was slowly added to the bottom chamber and 75 µL was added to the top chamber using a VIAFLO-96 Liquid Handler. The plate

was then allowed to incubate overnight before HUVEC seeding. The day following NCIH441 seeding, the culture inserts were moved to a new receiver plate. HUVECs were seeded in the Transwell chamber on the opposite side of the NCI-H441 cells. HUVEC cells were passaged and suspended at 80,000 cells/mL. 10,000 cells/well in 100 μ L cell culture media were seeded in each well and allowed to incubate overnight. Inserts were transitioned to ALI 24–48 hours after HUVEC seeding. To culture at ALI, the media was removed from the bottom chamber and the media in the top chamber was replaced with 50/50% v/v NCI-H441 and HUVEC cell culture media with all supplements except fetal bovine serum (FBS). Instead of FBS, the media contained 1:50 v/v Ultrosor G serum substitute (final concentration 0.2 mg/mL) (Sartorius 15950-017) to promote differentiation and polarization of the epithelium. The plate was then cultured at ALI for 5–7 days until TEER reached above an average of 400 $\Omega \cdot \text{cm}^2$. Assays were typically performed on day 6 of ALI culture, day 9 since seeding NCI-H441. The process is summarized in **Figure 5-2** below.

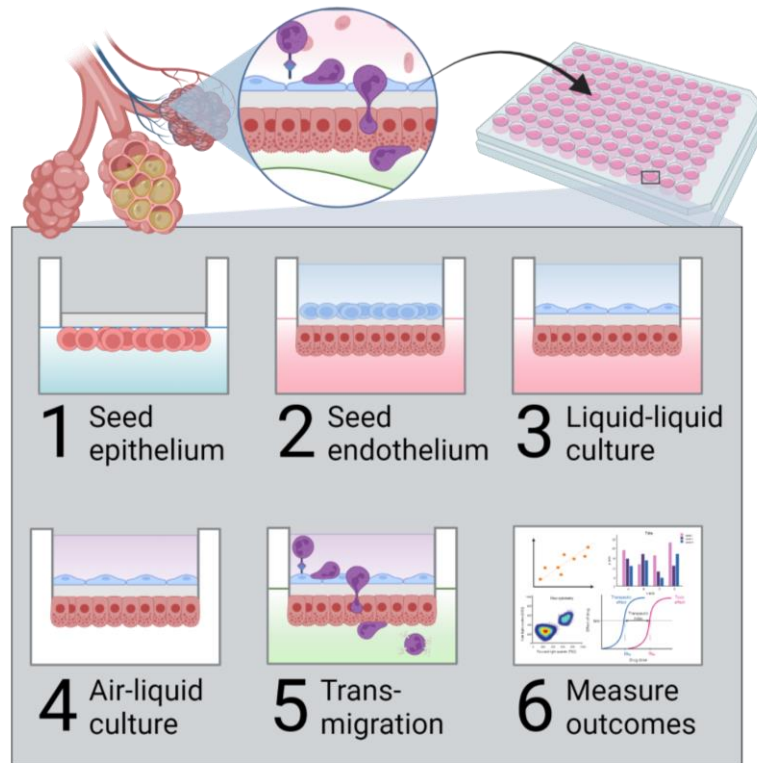


Figure 5-2 Preparation of Transwell bilayer coculture for transmigration assays

5.2.7 TEER measurement

Trans-epithelial electrical resistance (TEER). TEER was monitored prior to transmigration experiments using EVOM2 0-10 k Ω Range Epithelial Volt/Ohm Meter (World Precision Instruments) with the STX100C96 electrode (World Precision Instruments). The electrode was maintained as recommended by the manufacturer. Specifically, the electrode was cleaned by incubating overnight with Tergazyme (Alconox 1304-1), sanded gently as needed with sandpaper provided

by the manufacturer to keep the metal surfaces clean and exposed, and was soaked as needed in 5% v/v sodium hypochlorite for 5 minutes to maintain conductivity. Raw measurements of TEER were corrected according to the following formula:

$$TEER (\Omega \times cm^2) = [(Raw TEER (\Omega) - 200 \Omega) \times 0.143 cm^2]$$

200 Ω is the average value of a blank well with the equivalent volume of cell culture media, while 0.143 cm^2 is the surface area of the cell culture insert. For TEER measurements at ALI, 200 μ L/well 37 °C Earl's Balanced Salt Solution (EBSS) was added to the bottom chamber for measurement. For all TEER measurements, plates were placed on an electric warming plate set to 37 °C to maintain constant temperature because TEER can change with temperature.

5.3 Results and Discussion

5.3.1 Preparation of standardized ABBA array

Although *in vitro* neutrophil transmigration has been previously reported (**Table 3**), the application of miniaturized neutrophil migration in a high-throughput, physiologically relevant drug testing assay has not been described. To achieve such an assay requires rigorous quality standardization to ensure well-to-well and assay-to-assay reliability. Cell culture in 96-well microplates is notorious for suffering from edge-position dependent effects (i.e., edge effects) due to gradients in temperature, humidity, gas concentration, evaporation rate, and other environmental factors that influence cell metabolism, growth rates, and settling location^{225,226}. Therefore, cell culture and migration in this assay was validated against these factors by evaluation of barrier strength in each well after culturing with controlled humidity and temperature. Barrier strength reflects how well the epithelial-endothelial bilayer prevents the passage of matter such as ions, proteins,

and particles, and can be measured non-terminally using a TEER probe that applies a weak electric potential across the cell layer²²⁷. This allows the measurement of ion flux across inter- and intra-cellular pathways. A high TEER indicates high resistance to passive ion flow, and therefore a strong barrier.

Evaporation gradients are considered a primary cause of edge effects because the relative humidity of most cell culture incubators averages at 95% and transiently drops further when the door is opened^{228,229}. The ABBA is particularly susceptible to evaporation due to the small media reservoir (<150 μ L/well) and the air-exposed epithelium. Therefore, we developed a custom humidity chamber composed of a Nunc-well plate surrounded by 50-mL reagent reservoirs containing sterile water-saturated gauze with the plate in the center (**Figure 5-3**). ABBA plates that were cultured inside this humidity chamber within a standard cell culture incubator had reduced edge effects compared to plates without the humidity chamber (unpublished observation). Therefore, ABBA plates used in this study were cultured in the humidity chamber. Temperature gradients also cause edge effects including uneven cell seeding and growth rates due to the development of natural convection currents, which we observed when we performed seeding without temperature control (**Figure 5-4**)²³⁰.

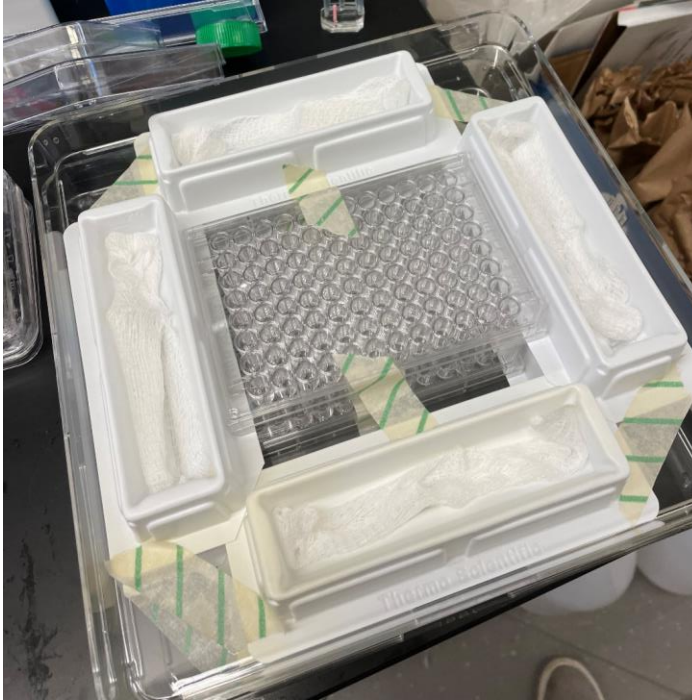


Figure 5-3 Humidity chamber prevents evaporation-dependent edge effects

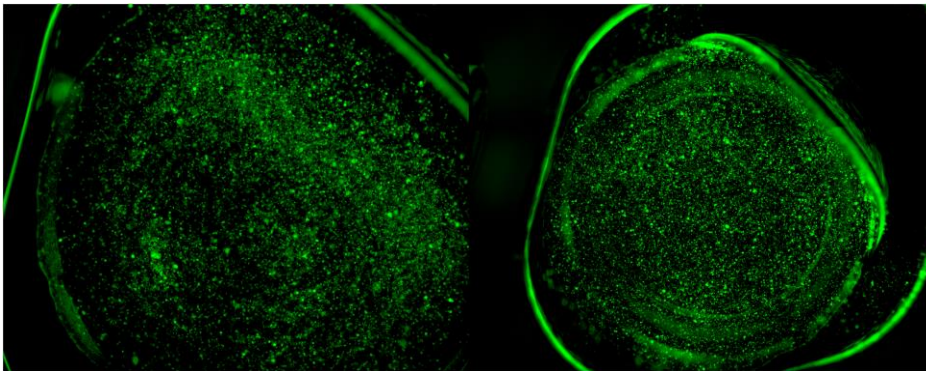


Figure 5-4 Edge effects due to temperature gradients.

Cell seeding without (left) and with (right) temperature control during seeding. Standardizing temperature during seeding prevents natural convection currents that distribute cells unevenly across the membrane.

Therefore, all handling of the ABBA plate during seeding, culture, and assay preparation were performed on an electric cell culture heating apparatus with all reagents kept at 37 °C. Indeed, performing epithelial and endothelial seeding with pre-warmed

plates on a heating plate significantly decreased barrier strength-related edge effects (unpublished observation).

To characterize edge effects on the ABBA, we measured TEER prior to transmigration and correlated it to edge position based on a scoring system where 0 corresponds to a corner, 1 to an edge well, 2 to wells 1 position away from an edge, etc. Previously we reported that the cell layers in the 96-well co-culture array was more likely to be subconfluent if TEER was below $286 \Omega \cdot \text{cm}^2$ ¹⁰⁰. We found that only the plate with mean TEER below $100 \Omega \cdot \text{cm}^2$ exhibited TEER-related edge effects, while plates with mean TEER above $200 \Omega \cdot \text{cm}^2$ did not exhibit significant position-dependent TEER effect. The lower TEER plates were most likely subconfluent based on previous observations, so we propose that the plates with low mean TEER exhibited edge effects due to subconfluent epithelial and/or endothelial cell layers caused by a combination of uneven cell seeding (temperature edge effect) and uneven growth rate (temperature and humidity edge effect). Nevertheless, plates that achieve even seeding and confluence showed higher TEER and no edge effects of TEER, suggesting that in most cases our mitigation efforts were effective.

5.3.2 Parameters for standardized transmigration in high-throughput

Next, we investigated the influence of barrier strength and edge position on the number of migrated neutrophils, a key assay outcome. We hypothesized that wells with significantly low TEER compared to the other wells on the same plate would allow the passage of more neutrophils by allowing neutrophils to migrate through areas that were not completely covered with epithelial cells, consistent with the same observations made by

Kidney and Proud (2000) during bronchial epithelial transmigration²⁰⁸. We conducted five independent transmigration experiments with assay plates having variable mean TEER (**Table 5**). Despite standardization of the plate preparation protocol, some variability between plates can occur. For each experiment, we correlated the number of migrated neutrophils from each well to the well's initial TEER. Linear regression analysis showed that there was a very significant ($p < 0.0001$) non-zero slope for the correlation between TEER and migrated neutrophil number in only the two plates with mean TEER 99.5 (+/- 41.4) and 206.3 (+/- 48.9) and these two correlations also had the highest r^2 values of 0.3988 and 0.2753, respectively (**Table 5**). One plate had a significant but weak correlation with $p = 0.001$ and $r^2 = 0.1316$. The remaining two plates had no significant correlation. These results suggest that TEER is related to migrated neutrophil number only when the mean plate TEER is at or below $206.3 \Omega \cdot \text{cm}^2$.

We next studied the effect of edge position on the number of migrated cells. The plates with mean TEER below $250 \Omega \cdot \text{cm}^2$ that demonstrated TEER-dependent edge effects also showed association between edge position and neutrophil number (**Figure 5-5**). Plate 3 did not exhibit TEER edge effects but did have neutrophil number edge effects. We speculate that this effect was not biological but rather was observed due to evaporation of edge wells during storage of the fixed cells before flow cytometry, concentrating the cells and creating a falsely higher value for edge wells during cytometry. Plate 5 experienced TEER and neutrophil edge effects, and we expect this was due to increased cell migration in wells with lower TEER due to edge-dependent differences in cell confluence, differentiation, or both. Control of plate evaporation during all stages of handling negates cell number edge effect in plates with no TEER-based edge effect.

Table 5. Effect of TEER and Edge Position on Migrated Cell Number

Exp.	n (wells)	TEER ($\Omega \cdot \text{cm}^2$)		Edge Effects?		TEER vs. Cell #	
		Mean	St. Dev.	TEER	Cell #	Goodness of fit	Significance
EXP. 5	96	99.5	41.4	Yes	Yes	$r^2 = 0.3988$	p < 0.0001
EXP. 3	59	206.3	48.9	No	Yes	$r^2 = 0.2753$	p < 0.0001
EXP. 1	48	266.2	58.3	No	No	$r^2 = 0.02438$	p = 0.3493
EXP. 4	91	271.0	55.1	No	No	$r^2 = 0.1316$	p = 0.0010
EXP. 2	24	273.1	58.8	No	No	$r^2 = 0.002197$	p = 0.8278

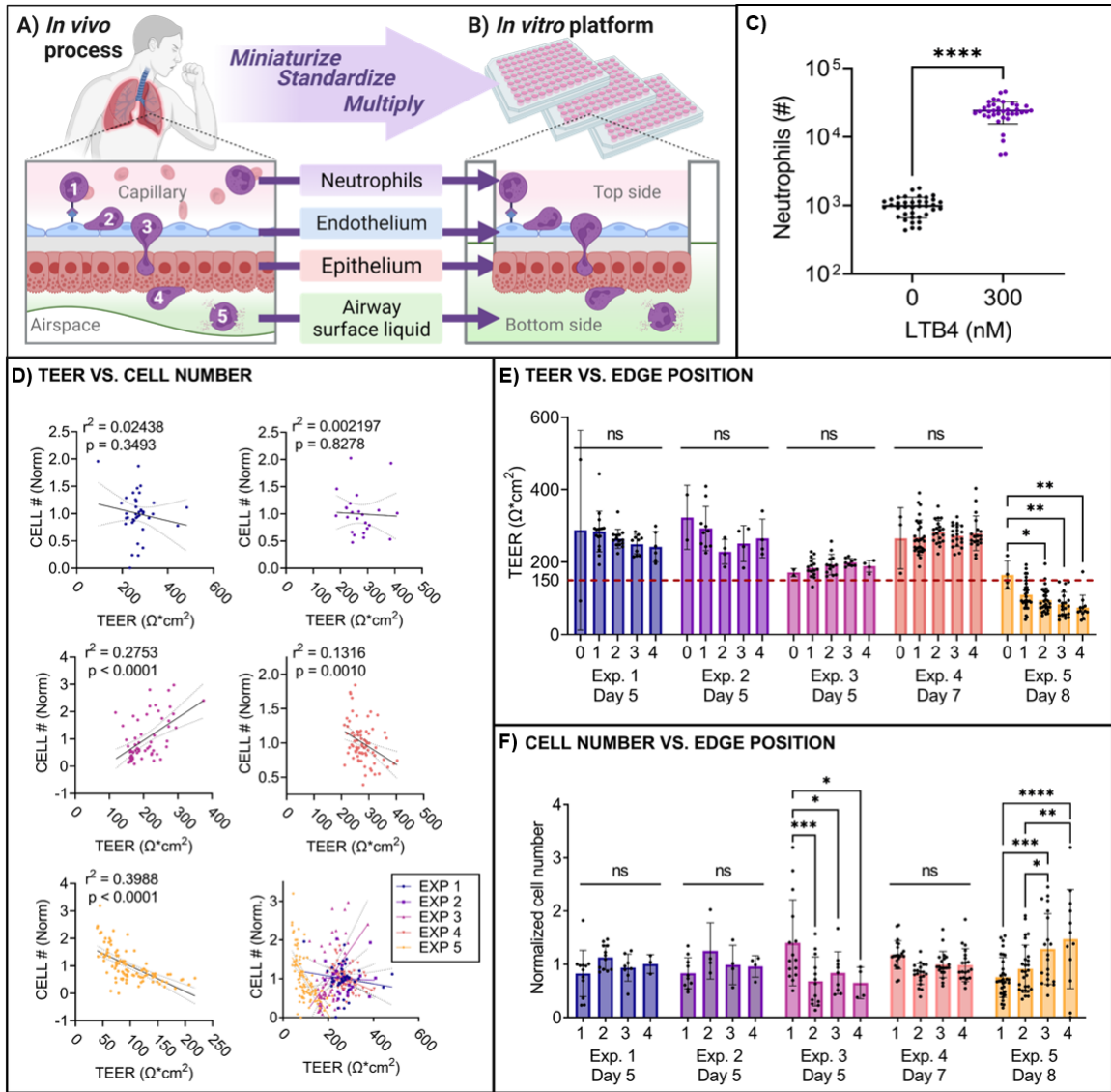


Figure 5-5 Transmigration assay models neutrophilic inflammation.

A) The distal lung's air-blood barrier is composed of a monolayered epithelium that grows opposite a capillary endothelium on a thin basement membrane. This tight barrier separates outside air from the bloodstream and facilitates gas exchange. During various lung injuries, neutrophils infiltrate the air space from the capillaries, first adhering to the endothelium (1), then rolling (2), crossing the endothelium and epithelium in succession (3) and arriving in the epithelial airway surface liquid (4). Upon arrival neutrophils are primed to respond to their microenvironment and may release granules containing proteases, inflammatory cytokines, chemokines and growth factors (5). **B)** We miniaturized and standardized this transmigration process in a minimally complex, high-throughput platform using a 96-well Transwell culture plate with air-liquid interface differentiated epithelial cells on the underside of a membrane opposite primary endothelial cells in plate as we previously described (Viola 2021). **D)** Migrated neutrophil number is free of TEER- and edge- dependence above a TEER threshold. In 5 independent Transwell plates cultured

on different days, TEER of each well was measured immediately prior to neutrophil transmigration for 16 hours. Then, the number of migrated neutrophils was counted and correlated with initial TEER using simple linear regression followed by Wald's test for slope significance (GraphPad Prism 9). **E)** TEER immediately prior to transmigration was independent of edge position unless the average plate TEER was below $150 \Omega \cdot \text{cm}^2$ (red dashed line). **F)** From the same 5 independent Transwell plates, the number of migrated neutrophils was independent of edge position unless the average TEER was below $200 \Omega \cdot \text{cm}^2$ (red solid line). Migrated cell number was not strongly correlated with TEER ($p > 0.05$) when mean plate TEER exceeded approximately $200 \Omega \cdot \text{cm}^2$ (red solid line), Table 5. Strong correlations, defined as $r^2 > 0.25$ and $p < 0.0001$, had opposite slopes. Overall, no consistent trend between TEER and cell number was observed. $n = 38, 24, 59, 79,$ and 96 wells for Experiments 1-5, respectively. All statistics were performed on GraphPad Prism 9 as follows. **A, B:** Two-way ANOVA with post-hoc Tukey's t -test for multiple comparisons without matching. **C:** Simple linear regression with $\alpha = 0.05$ and Wald test for significantly nonzero linear regression slope. $ns =$ not significant, $*p \leq 0.05$, $**p \leq 0.01$, $***p \leq 0.001$, $****p \leq 0.0001$

5.3.3 Dose-dependent neutrophil recruitment and activation

Neutrophils' primary activity in inflammation is migrating to a tissue site and becoming activated to clear debris and pathogens, and release antimicrobial products. While the specific phenotype of activation is disease- and tissue-specific, typical features of neutrophil activation are phagocytosis of pathogens and cellular debris, degranulation of proteases, cytokines, chemokines, and other mediators, production of reactive oxygen species, and the release of neutrophil extracellular traps⁷³. Neutrophil interactions with the endothelium and epithelium in a physiologic direction also prime them for action upon reaching the site of inflammation.

We used the ABBA to analyze epithelial-endothelial bilayer transmigration towards known chemokines in a dose-response format and measured key outcomes of migrated neutrophil number and activation state. *In vitro*, neutrophils migrate dose-dependently across epithelial monolayers towards IL-8 and LTB₄, and across epithelial-endothelial bilayers towards chemokines IL-1 β and TNF- α ^{207,208,210}. We showed that

chemoattractants IL-8 and LTB4 both attracted neutrophils dose-dependently from 5 independent donors (**Figure 5-6(A)**). Dose-response curves for each donor revealed strong, significant linear correlations ($r^2 > 0.75$, $p < 0.001$) between neutrophil number and chemoattractant dose. Wald's test comparing multiple linear correlation slopes suggested that the dose-response linear correlation slopes are significantly different between donors for transmigration to IL-8, but not LTB4. We speculate that such differences could be due to donor-specific difference in the expression of the neutrophil IL-8 receptor CXCR1, but further study is required²³¹. This experiment demonstrates the utility of this assay for sensitive detection of migrated neutrophil number across multiple donors and chemoattractants.

Neutrophil priming and activation entails surface mobilization of secretory vesicles and subsequent exocytosis or intracellular mobilization of granules containing cytokines, proteases and growth factors^{232,233}. To assess the assay's ability to detect neutrophil activation phenotypes, we conducted transmigration experiments at increasing doses of the chemoattractants LTB4 and TNF- α . Both chemoattractants dose-dependently attract neutrophils (**Figure 5-6(B-C)**). We saw significant downregulation of integrin receptor CD62L, also called L-selectin, suggesting that neutrophils interacted with endothelial and epithelial integrins during transmigration^{234,235}. The observed increased expression of surface CD66b reflects increasing degrees of neutrophil degranulation^{236,237} upon migration, as a consequence of increasing pro-inflammatory cytokine concentration^{238,239}, showing that neutrophils are sensitive to the magnitude of a pro-inflammatory stimulus. These results demonstrate that this assay can dose-dependently detect alterations in

neutrophil surface marker expression that associate with interactions between neutrophils and surrounding cells and mediators (**Figure 5-6(D-F)**).

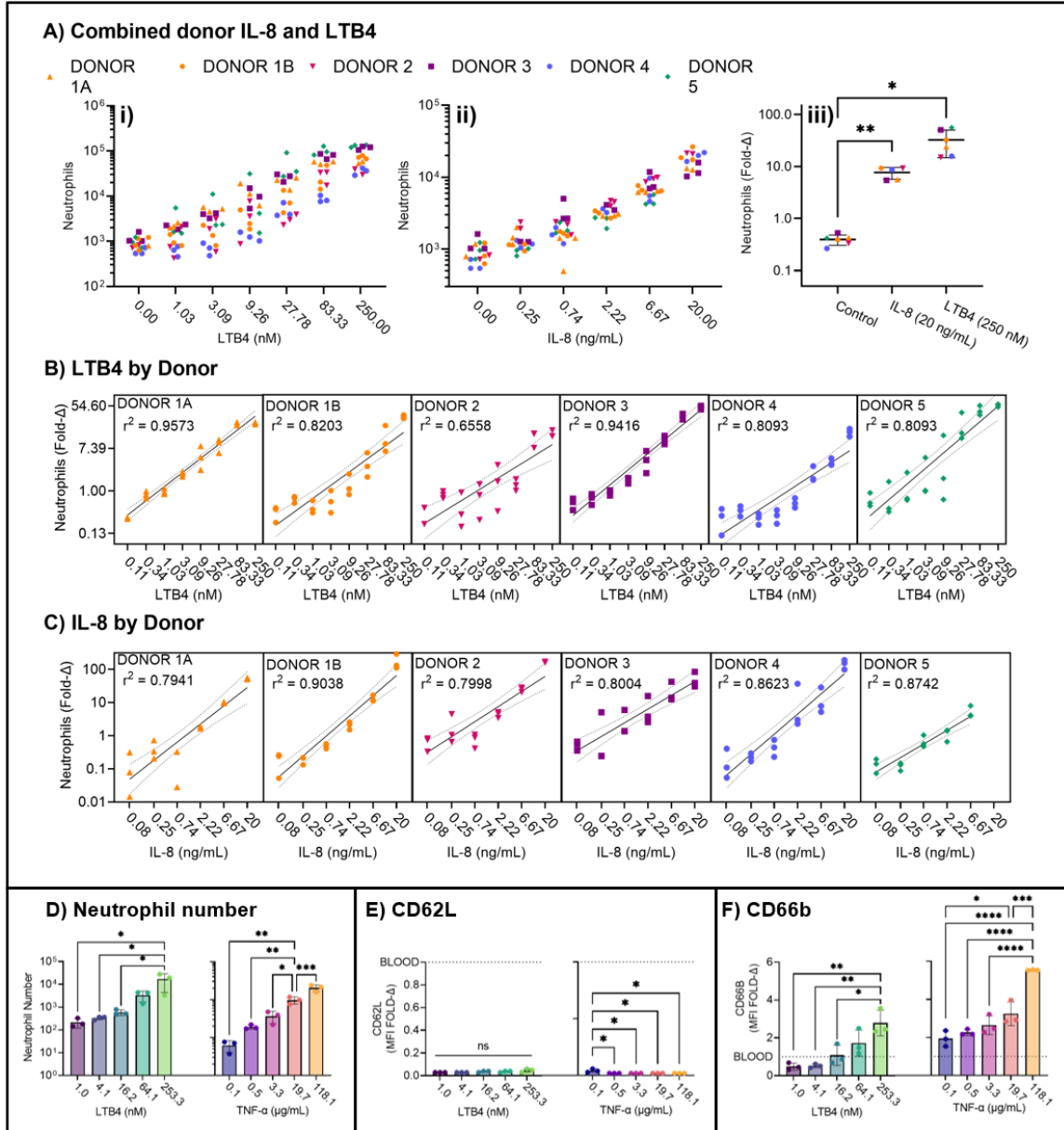


Figure 5-6. Neutrophils from different donors consistently migrate dose-dependently to chemoattractants

A) Combined dose-response for 5 donor transmigration to **i)** LTB4 or **ii)** IL-8. Donor 1A and 1B denote the same donor in independent experiments. **iii)** All six donors show similar magnitude of response to no chemoattractant, 20 ng/mL IL-8, or 250 nM LTB4. **B-C)** Dose-response log-log plots show linear correlation between chemoattractant concentration and number of migrated neutrophils across six donors for LTB4 (**B**) or IL-8 (**C**). Wald's test

*for linear correlation slopes suggests that the slope of the linear correlation line is significantly different between donors for IL-8 but not LTB4. D-F) Neutrophils are activated dose-dependently in response to chemokine gradients. Solid line indicates linear correlation line; dashed lines indicate 95% confidence intervals of the linear correlation. Statistical analyses performed using GraphPad Prism 9. Ns = not significant, * $p \leq 0.05$, ** $p \leq 0.01$, *** $p \leq 0.001$, **** $p \leq 0.0001$.*

5.3.4 Capturing a disease-specific microenvironment and inflammatory responses

Neutrophil phenotype and behaviors depend on disease-specific microenvironmental programming through soluble mediators and cell-cell binding interactions. Our assay is uniquely capable of providing the necessary microenvironmental cues to program neutrophils towards a disease-specific phenotype in a high-throughput, standardized, and miniature platform. Previous platforms have demonstrated that transmigration into CF airway surface liquid supernatant (ASN) programs neutrophils towards a CF-characteristic phenotype characterized by decreased bacterial killing, enhanced glycolysis, and increased respiratory burst¹⁷³. These “GRIM” neutrophils were also associated with decreased secretory vesicle marker CD16 and L-selectin (CD62L), and significantly increased degranulation markers CD63 and CD66b compared to blood neutrophils. We showed that this model system can reproduce these key expression markers of CF airway neutrophils. We obtained processed, pooled CF sputum from the Tirouvanziam laboratory at Emory University (under IRB 00042577) . Tirouvanziam laboratory processed the CF-ASN as previously described¹⁷³. We placed diluted CF-ASN in the bottom receiver plate. Neutrophils were allowed to migrate for 18 hours into CF sputum, diluted in cell culture at a ratio between 1:12 to 1:1 as shown.

CF sputum contains high concentrations of neutrophil chemoattractants and activators including TNF- α , IL-8, IL-1B, fMLP, C5a, and PAF²⁴⁰. We showed that neutrophils migrated dose-dependently to increasing concentrations of sputum, mimicking the same trend we demonstrated in response to known concentrations of defined chemokines. Second, we showed that TEER increases for low sputum concentration and decreases at high sputum concentration. We speculate that this effect is due to the beneficial growth factors and mediators in the sputum²⁴¹. At high sputum concentration in the assay, neutrophils migrate in high numbers and produce elastase and other proteases that damage the epithelium²⁴². At low sputum concentrations, very few neutrophils migrated and the liquid culture of the epithelium with sputum may have benefitted barrier function through the presence of growth factors in combination with a lower concentration of active neutrophil elastase. Finally, we stained the endothelium for the adhesion marker e-selectin and showed that it was dose-dependently increased with greater concentration of CF sputum on the epithelium. Indeed, CF patients exhibit increased soluble adhesion ligands including e-selectin^{243,244}, and incubation of human microvascular endothelial cells with soluble components of CF sputum induced upregulation of e-selectin that promoted neutrophil adhesion²⁴⁵. For surface marker expression analysis we excluded the 1:12 and 1:6 conditions due to low cell number. We found that neutrophils shed the integrin CD62L during transmigration as expected, and neutrophils' expression of CD66b was increased dose-dependently compared to the non-transmigrated control. CD63 increased compared to the non-transmigrated control, and CD16 decreased. This profile of markers mimics that of CF neutrophils as previously demonstrated. Overall, our model mimics CF-characteristics of increased neutrophil recruitment, increased expression of e-selectin, and

neutrophil activation and degranulation. Importantly, this model requires only 33 μL of pooled CF ASN per well for the 1:3 dilution that demonstrates CF-neutrophil mimicking characteristics. Therefore, the model reduces the sputum volume required in previous assays by over twenty-fold.

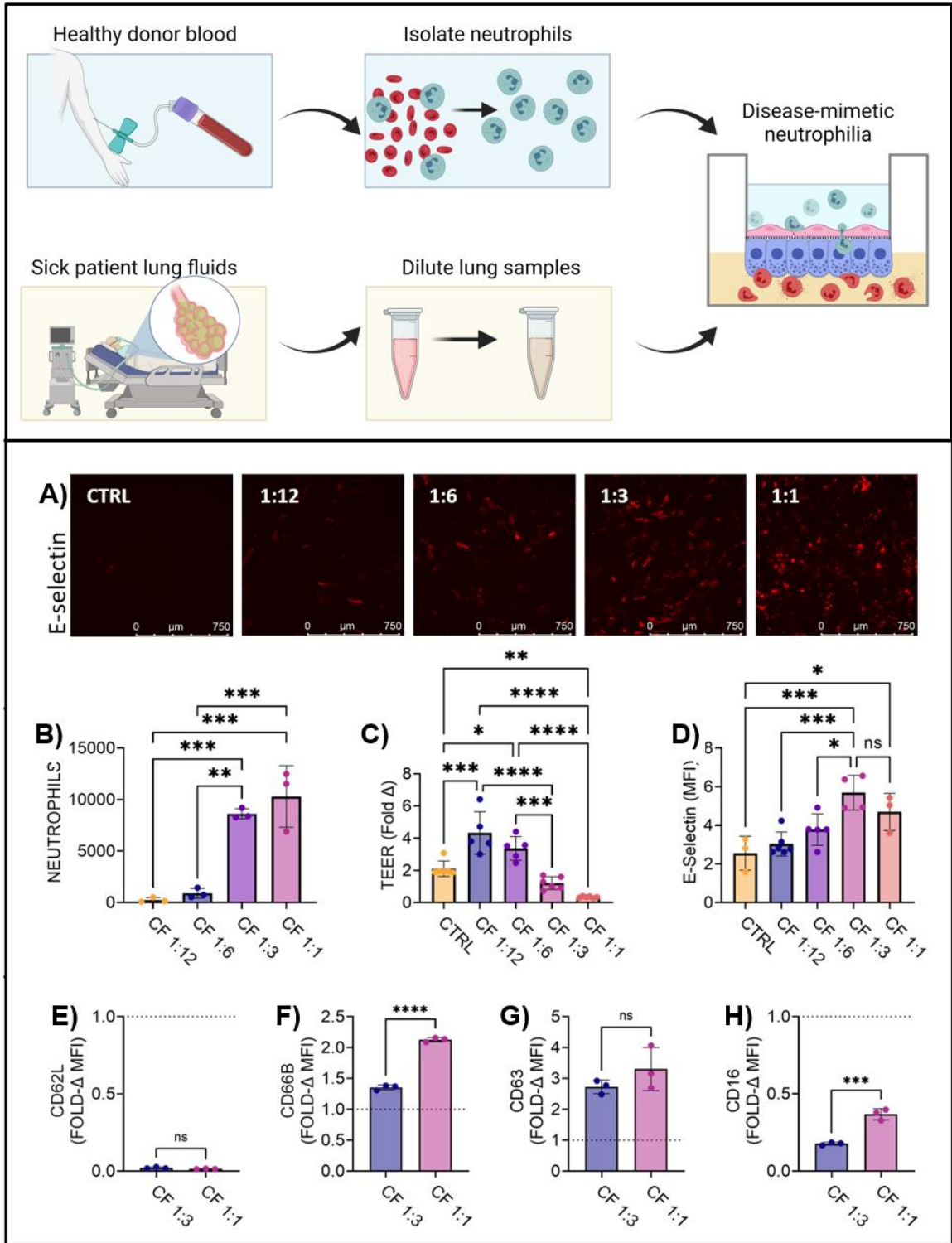


Figure 5-7. Transmigration replicates CF-like neutrophil activation and air-blood barrier properties

A) *E*-selectin immunofluorescence staining after 14 hours transmigration into CF airway supernatant diluted 1:12-1:1 vs. incubated in ALI medium without transmigration (CTRL). **B)** Number of migrated neutrophils after 14 hour migration to CF-ASN. **C)** TEER fold-change compared to the same wells' initial TEER. Control wells from the same plate were maintained at ALI for the duration of the experiment. Low concentration of CF-ASN (1:12, 1:6) increased TEER but highly concentrated CF-ASN reduced TEER compared to ALI controls. **D)** Endothelial *e*-selectin MFI, quantified using ImageJ analysis of immunofluorescence stains, was upregulated after CF-ASN transmigration dose-dependently. **E)** CD-62L, also called *L*-selectin, was shed from transmigrated neutrophils. **F,G)** CD66b and CD63 were upregulated compared to blood neutrophils prior to transmigration (dashed line) indicating degranulation. **H)** CD16 was downregulated compared to blood neutrophils (dashed line) indicating CF-like activation. All statistics performed using GraphPad Prism 9. **B-D)** One-way ANOVA with post-hoc Tukey's *t*-test for multiple comparisons without matching. **E-H)** Student's *t*-test (unpaired). For all tests, $\alpha = 0.05$. *ns* = not significant, * $p \leq 0.05$, ** $p \leq 0.01$, *** $p \leq 0.001$, **** $p \leq 0.0001$.

5.3.5 Dose-response comparison of immunomodulatory therapeutics baricitinib and dexamethasone

Finally, a key application of this assay is high-throughput immunomodulatory drug screening in a human-relevant microenvironment. To our knowledge, all previous assessments of drug effects on neutrophil transmigration were performed without epithelial-endothelial bilayer transmigration. The bilayer of lung structural cells enhances physiologic relevance of therapeutic testing by including the effects of anti-inflammatory agents on both neutrophils and surrounding cell types that are intimately involved in the coordination of neutrophil transmigration²⁴⁶. Endothelial and epithelial cells express adhesion ligands including *e*- and *p*-selectin, ICAM and VCAM that facilitate transcellular extravasation²⁴⁷. Both cell layers also respond to insults by releasing neutrophil chemoattractants including LTB₄, IL8, and TNF- α ^{248,249}. Finally, the cell barrier regulates the transfer of proteins and small molecules, compartmentalizing the epithelial chemoattractant gradient from endothelial drugs¹¹⁰. Importantly, the sequestration of

therapeutics to the endothelial layer in a physiologic manner may prevent the action of therapeutics from reaching airway neutrophils. We showed that permeability of the cell bilayer is maintained after 14-hour transmigration to LTB4. **Table 6** shows that the bilayer permeability remains within the range of epithelial monolayers

Table 6. Permeability of epithelial-endothelial bilayers post-transmigration

Value	Pore size	Cell type	Author
2.7 ng/cm ² (2.1e-7 cm/s)	3 μm	H441-HUVEC bilayer (post-transmigration)	This work
10-150 ng/cm ²	0.4 or 1 μm	Primary nasal epithelium	Kreft 2020 ⁶⁶
1e-5 to 1e-7 cm/s	0.4 or 1 μm	Calu-3	Kreft 2015
0.2-1e-6 cm/s	0.4 μm	Calu3, 16HBE140, NHBE	Bosquillon 2017
1.58e-7 cm/s	0.4 μm	H441	Salomon 2014

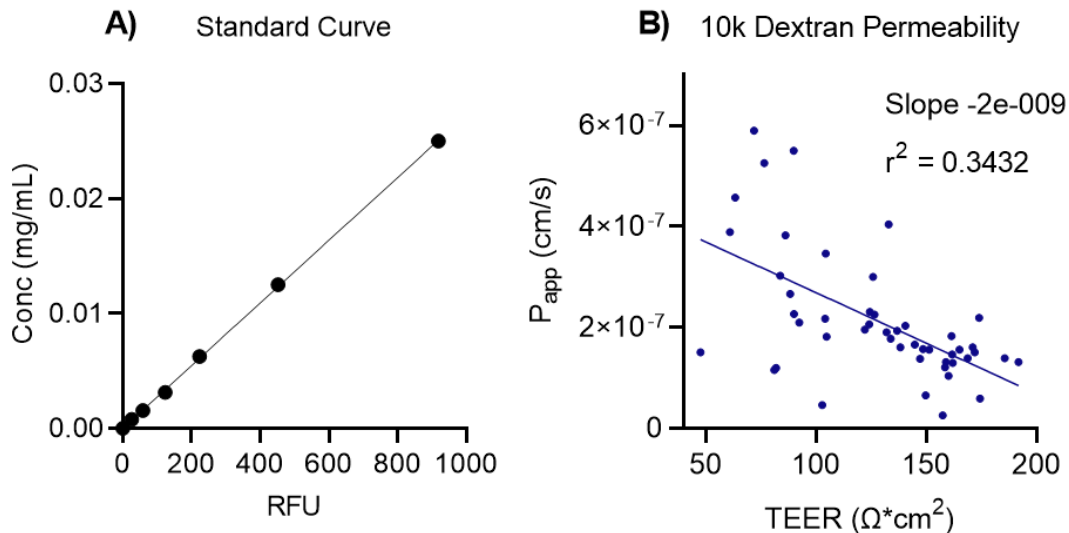


Figure 5-8 Permeability vs. TEER after transmigration

A) Standard curve of 10k Dextran vs. relative fluorescence units. **B)** Relationship between Transwell TEER and permeability to 10k Dextran with Simple Linear Regression (GraphPad Prism 9).

We tested the effects of two clinically available anti-inflammatory therapeutics of different mechanisms, dexamethasone (brand names Ozurdex, Maxidex, DexPak 6 Day,

and others) and baricitinib (Brand name Olumiant). Dexamethasone is an established glucocorticoid, which is a class of synthetic hormones that have for many years been employed to control pulmonary inflammation⁶⁶. Glucocorticoids primarily act through the abrogation of NF- κ B-dependent pro-inflammatory gene transcription, and the upregulation of anti-inflammatory genes^{250,251}. Glucocorticoids are generally effective at controlling lymphocytic pulmonary inflammation, are widely used in the management of obstructive lung disease, and have shown promise in the treatment of COVID-19 ARDS⁶⁶. *In vivo* studies have shown a reduction in neutrophil numbers in the BALF of mice injured with LPS and VILI^{252,253}. Importantly, the precise quantitation of infiltrated neutrophils in BALF is technically challenging due to the unknown dilution of BALF with saline during sample collection²⁶. Therefore, this study compliments existing evidence in a defined migration platform with known dilution factors to assess the wholistic effect of dexamethasone on the transepithelial-transendothelial recruitment of neutrophils along an IL-8 chemoattractant gradient.

We contrasted dexamethasone with a novel anti-inflammatory baricitinib that belongs to the group of Janus kinase (JAK) inhibitors (JAKinibs). JAKs mediate the signal transduction of Type I and II cytokine receptors that bind over 50 cytokines, interleukins, colony stimulating factors and hormones²⁵⁴. Therefore JAKinibs have been in clinical development over the last decade for the treatment of various inflammatory disorders, primarily rheumatoid arthritis and dermatologic autoimmune conditions^{254,255}. JAKinibs have recently become promising pulmonary anti-inflammatory candidates in obstructive lung disease, COVID-19 lung disease, and asthma, among others²⁵⁶⁻²⁶⁰. Baricitinib in particular has inhibited neutrophil infiltration to the joints in human clinical trials for

rheumatoid arthritis²⁶¹ and to the distal lungs of rhesus macaques infected with COVID-19²⁶². However, the mechanisms by which baricitinib may directly or indirectly interfere with neutrophil recruitment are still unclear despite these promising results.

We simulated an acute inflammatory event in the distal lungs by placing IL-8 (20 ng/mL) on the epithelial side of the ABBA bilayer. We added neutrophils to increasing concentrations of each drug and allowed overnight (16 hours) transmigration to IL-8. For Donor 1, baricitinib inhibited the transmigration of neutrophils with an IC₅₀ of 2.698 (95% CI 0.6169 – 10.34) (Run 1) and 1.375 (95% CI 0.1981 – 8.197) (Run 2). Dexamethasone failed to reduce the number of transmigrated neutrophils in both trials for Donor 1. Interestingly, Donor 2 neutrophils did not respond to baricitinib or dexamethasone, retaining a basal rate of IL-8 induced transmigration under all drug conditions. Importantly, **Figure 4-5(D)** shows that the total number of migrated neutrophils is similar for both donors, confirming that Donor 2 did have significant IL-8 mediated neutrophil migration as opposed to no migration at all which would have also shown no drug effect.

Dexamethasone failed to inhibit neutrophil transmigration despite previous evidence that glucocorticoids are effective at reducing neutrophil infiltration *in vivo*. However, glucocorticoids have been shown to have no effect on pulmonary neutrophil infiltration and even increase its magnitude in animal studies of lung injury with LPS, bleomycin, and Ventilator-induced lung injury^{263–265}. Further, intravenous glucocorticoids increased pulmonary neutrophil infiltration in multiple studies in human asthma patients^{266,267}. The effects of glucocorticoids on pulmonary neutrophil recruitment, therefore, are not settled.

The negative effects of glucocorticoids are thought to result from the established role of glucocorticoids in promotion of neutrophil survival²⁶⁸⁻²⁷⁰, enhancement of endothelial adhesion²⁷¹⁻²⁷³, and recruitment through the BLT-1 pathway that is not suppressed, and may be increased, by glucocorticoids²⁷⁴. Schleimer (2004) suggests that the beneficial clinical effects of glucocorticoids in lung disease *in vivo* emerge from the suppression of chemoattractant gradients that recruit neutrophils, rather than the direct abrogation of neutrophil chemotaxis, reasoning that “the inhibitory effects of glucocorticoids on leukocyte recruitment are mediated at the level of the production of the chemoattractants, not at the level of the leukocyte response. If chemoattractants (e.g., C3a, C5a, SAA, etc.) can be generated in the presence of glucocorticoids, then neutrophils and other cells with appropriate receptors are free to migrate despite the presence of glucocorticoids.²⁷⁵ Indeed, glucocorticoids suppress macrophage, epithelial, and endothelial production of chemoattractant proteins such as IL-8 and TNF- α , which supports *in vivo* studies showing reduced neutrophil recruitment^{66,276,277}. Our results, however, mirror other studies showing that after chemoattractants are available to neutrophils, glucocorticoids fail to interrupt neutrophil chemotaxis²⁶⁸.

In contrast to dexamethasone, baricitinib reduced transmigration of neutrophils by two- to four-fold despite the presence of an IL-8 chemoattractant gradient, but only for one of two donors tested. Baricitinib’s mechanisms of inhibiting neutrophil recruitment in this model are not clear and further mechanistic study is required. However, we speculate that baricitinib inhibits JAK3 signaling downstream of the IL-8 receptor signaling cascade to inhibit IL-8 mediated transmigration in this model. In this study, neutrophils were transmigrated to IL-8 which binds to neutrophils through CXCR1. Significantly, CXCR1

signal transduction does not require JAK1 or JAK2, the primary targets of baricitinib. However, previous work showed that IL-8-driven, CXCR1-mediated chemotaxis depends on JAK3²⁷⁸. Baricitinib shows potency against JAK3 (≈ 560 nmol/L) in addition to its more potent inhibition of JAK1 and JAK2 (IC₅₀ 5.9 and 5.7 nmol/L, respectively)^{279,280}. Indeed, other studies found that JAK1/2 inhibition prevents neutrophil chemotaxis towards IL-8 *in vitro*²⁸¹ and reduces neutrophil aggregation in humans with rheumatoid arthritis.

Baricitinib could also affect epithelial-endothelial barrier properties and behavior. The endothelium facilitates transmigration by upregulating e-selectin and other adhesion ligands in response to the applied chemoattractant gradient. Blockade of JAK1/2 could in theory interrupt endothelial adhesive protein mobilization as well as prevent endothelial release of chemoattractant proteins and molecules. However, JAK1/2 inhibition with ruxolitinib did not significantly reduce the expression of ICAM-1, VCAM-1 or e-selectin in response to TNF- α stimulation in human aortic endothelial cells²⁸². Additionally, JAK1 mediates epithelial type I interferon signaling, particularly sensing of interferon gamma (IFN- γ)^{283,284}. IFN- γ modulates several key events in neutrophil transmigration. It controls epithelial expression of neutrophil adhesion molecules and enhances neutrophil-epithelial adhesion^{208,285}. Additionally, IFN- γ directly influences neutrophil recruitment *in vivo* via the intermediate CCL3²⁸⁶. Finally, JAK1/2 inhibition could indirectly preserve epithelial-endothelial barrier strength during inflammation by reducing JAK1/2 dependent cytokine signaling, including type I interferon signaling. Indeed, many JAK1 or JAK2-dependent cytokine cascades are implicated in loss of tight junction and adherens junction stability and a resultant decrease in barrier strength in various epithelial and endothelial cells and tissues²⁸⁷⁻²⁹⁰. JAK/STAT inhibition is therefore a promising therapeutic target for

ulcerative colitis, irritable bowel syndrome, and atopic dermatitis, diseases with characteristically weak epithelial barrier function²⁹¹⁻²⁹³. However, these potential positive effects of JAK1 inhibition on the epithelial-endothelial barrier strength would **not** be likely to affect the number of migrated neutrophils in our model. We showed that barrier strength is poorly associated with the number of migrated neutrophils (Figure 5-5). Therefore, an improved barrier function, while incredibly important to disease resolution, is unlikely to directly influence the number of migrated neutrophils in our model. Nevertheless, barrier strength with and without neutrophil migration in the presence of therapeutics should be explored in future investigations as a key outcome of drug treatment.

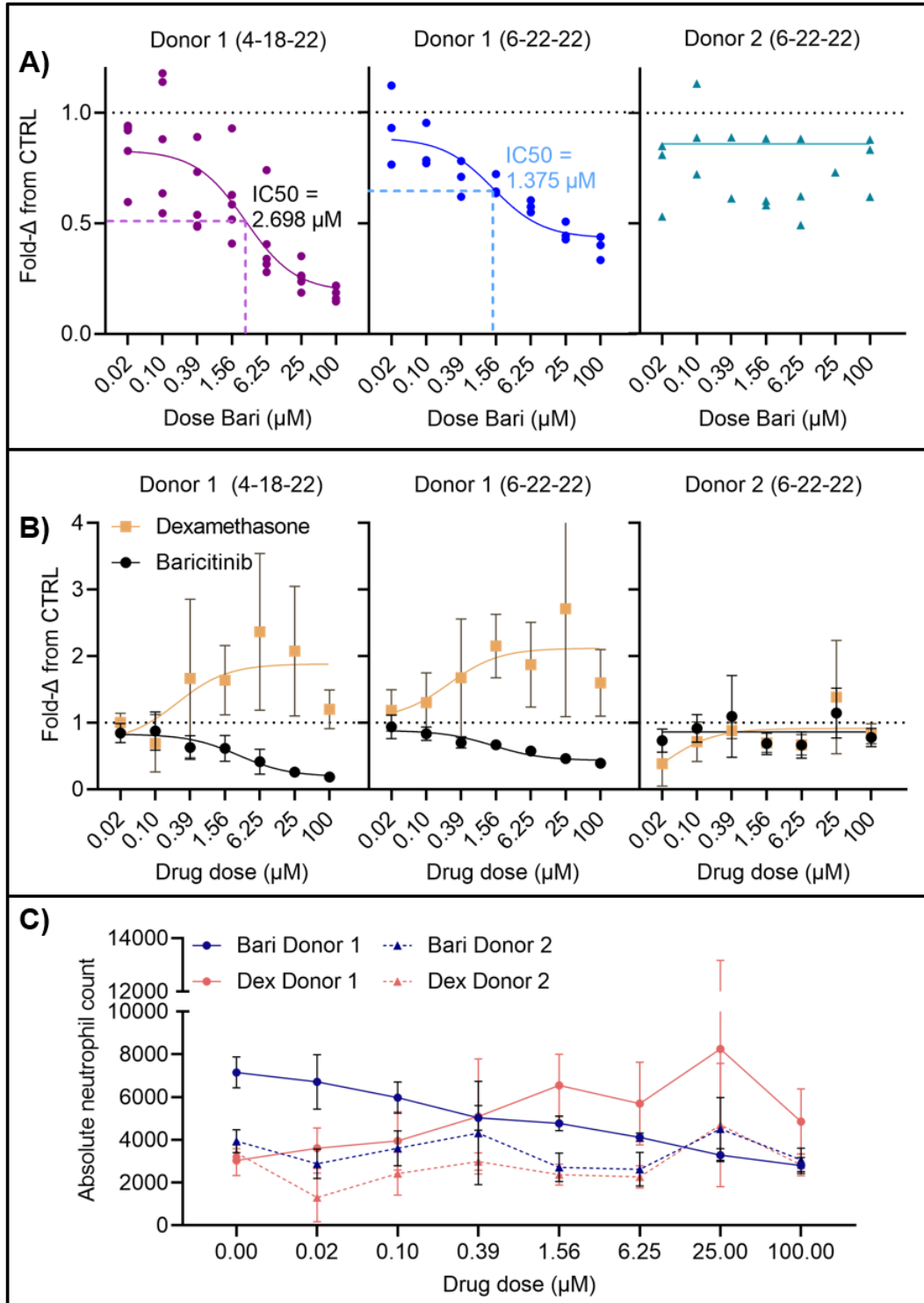


Figure 5-9 Baricitinib vs. dexamethasone dose-response

A) Baricitinib dose-response for two donors showing Logistic curve-fit model applied to the log₁₀(dose) vs. fold-change response. Donor 1 replicated two months apart. B) Comparison of baricitinib and dexamethasone dose-response from the same experiments

as A) showing logistic curve-fit model applied to the $\log_{10}(\text{dose})$ vs. fold-change response. C) Absolute neutrophil counts vs. drug dose for both drugs.

5.4 Discussion

In this chapter, we develop a novel high-throughput, small volume method for the assessment of neutrophil transmigration through an epithelial-endothelial bilayer. We demonstrate that transmigration to both agonist and inhibitor is dose-dependent and that transmigration in the presence of an agonist (chemoattractant) results in comparable dose-response results while transmigration in the presence of inhibitors (baricitinib and dexamethasone) induces differential results for two donors.

Further, we demonstrate that the model is capable of recapitulating key aspects of CF lung disease. This capability arises from the model's inclusion of CF sputum derived from patients. The transmigration into sputum followed by overnight incubation produces neutrophils with a phenotype similar to those of children with CF. Further, the exposure results in dose-dependently increasing endothelial expression of e-selectin, an adhesion molecule that promotes neutrophil transmigration. The capability to reproduce the functional aspects of CF lung disease *in vitro* in such high-throughput and small volume is unprecedented.

CHAPTER 6. CONCLUSIONS AND FUTURE DIRECTIONS

The methods developed herein represent a technological advance as well as an improvement in opportunities to study airway disease. In the first Aim we describe a novel mechanism for the stable generation of liquid plugs that injure the airway epithelium. In the second chapter we innovate a method to prepare standardized 96-well plates of lung air-blood barrier microtissues. In Aim 3 we apply the 96-well ABBA to generate a highly validated neutrophil transmigration assay. These technological achievements open the door to future detailed biological studies of the small airways. The key innovative aspects of these advances, and their applicability to novel investigations, are discussed herein.

6.1 Major challenges

6.1.1 *Tracheal aspirate sample dilution effects and phenotypic validation*

Work with unpooled primary tracheal aspirate samples in the neutrophil transmigration assay was significantly limited by the dilution of samples with saline. This dilution is clinically necessary but results in significant variation in the concentration of proteins and cells in each collected sample. Several strategies can be developed to overcome this variation for patient-specific transmigration studies.

First, samples may be lyophilized and reconstituted in an equal concentration for each patient. This strategy makes the most sense with very dilute samples (< 0.05 mg/mL total protein) but will compromise delicate proteins and mediators that are susceptible to degradation during lyophilization, freezing, and/or resuspension. Second, the total protein concentration may be quantified, for example, using a Bradford Assay, and each sample

diluted to the same total protein concentration. This strategy is best when the samples being tested are significantly concentrated (>0.2 mg/mL total protein) but fails when the dilute samples are too dilute. Another strategy to overcome dilution effects is to simply supplement each sample with the same concentration of a known chemokine, e.g., LTB₄. This ensures all samples will migrate neutrophils. However, this strategy could induce non-physiological neutrophil activation by stimulating LTB₄-mediated responses that were not necessarily present in the patient's microenvironment in the lung. It is likely, however, that LTB₄ concentrations are high in the ARDS lung due to endogenous production by neutrophils, and that that LTB₄ degrades during sample collection and preparation. Therefore, restoration of a physiologically relevant LTB₄ concentration (50-100 μ M) may be reasonable.

The most robust method to ensure that sample dilution effects are controlled is the direct comparison of patient-derived tracheal aspirate neutrophils with the assay-generated airway-like neutrophils that were migrated into their same aspirate. This type of study would be reasonably feasible if the outcome were RNA transcription. Tracheal aspirate must be processed and frozen immediately after collection, and in the process the cells from the aspirate may be separated and stored in RNA-later. However, separation of the tracheal aspirate cell content into different cell types before lysis would be extremely difficult, requiring live cell FACS, and therefore the RNA sample would be contaminated with epithelial and macrophage RNA. The second method of comparison would be flow cytometry, which is also feasible by staining and fixing the cell portion of aspirate and later measuring the cells' expression of surface markers using flow cytometry. This data could be compared directly to the transmigrated neutrophils generated by the same patients'

tracheal aspirate. The limitation of this technique is that flow cytometry can only easily measure about 13 surface markers at a time, and at absolute maximum 30 (with great difficulty). This is significantly less information than genomics and transcriptomics provides.

Finally, the “holy grail” of patient specific airway neutrophil mimicking would be to migrate patient-derived peripheral neutrophils into autologous tracheal aspirate. This would generate the most similar possible system that would be most likely to mimic patient responses appropriately and provide predictive power for therapeutics. This would be extremely difficult to achieve, requiring both tracheal aspirate and blood collection and processing. Although feasible in a small scale (3-6 patients), this method is impractical for data collection at reasonable patient numbers (100+ patients), limiting its utility.

6.1.2 Challenge: Sources of variability in ABBA experiments

6.1.2.1 Well-to-well

It is critical for ABBA plates to maintain as much standardization as possible for inter- and intra-assay reliability. The primary sources of well-to-well variability within a single plate are temperature and humidity gradients, especially during epithelial cell seeding. Edge effects are especially prominent due to temperature-related convection currents (Figure 5-4). Evaporation gradients can develop during long-term incubator culture due to increased medium evaporation at edge wells compared to central wells. Therefore, humidity is supplemented with a custom humidity chamber to prevent uneven evaporation (Figure 5-5). Other sources of well-to-well variation include poor cell suspension mixing during seeding, accidental puncture of membranes with pipette tips, and

contamination. All of these variation sources are minimized by controlling temperature and humidity and employing correct culture and sterility techniques. To minimize the influence of well-to-well variability on experimental results, experimental conditions should be tested in at least 3 wells per condition on a single plate. These are denoted as technical replicates throughout this text.

6.1.2.2 Plate-to-plate

A moderate limitation to the ABBA plate and neutrophil transmigration assay is modest plate-to-plate variability in mean TEER. This effect was shown not to significantly impact neutrophil transmigration numbers but could become important in studies of barrier function. The most appropriate way to handle this variability is to include a control condition that experimental samples can be normalized against. Then different plates can be compared using these normalized values. This is also useful in neutrophil transmigration assays, since the absolute number of neutrophils measured on flow cytometry can vary significantly (>10%) even with identical handling and collection conditions due to slightly different degrees of cell loss during cell collection and processing. For example, in a TEER assay, we quantify the TEER change as % of initial TEER. For transmigration assays, we normalize experimental conditions as fold-change from a defined control such as an IL-8 well (20 ng/mL) with no other components. Inclusion of an LTB₄ or IL-8 dose-response standard curve would be perhaps even more efficacious at normalizing transmigrated cells although we have found that normalizing against IL-8 allows comparable results across different experiments in several studies, including agonist and inhibitor dose-responses.

6.1.2.3 Neutrophil and transmigration variations

The ABBA transmigration assay requires primary human neutrophils because no suitable cell line is available that captures neutrophil phenotype appropriately. As described in Chapter 5 (Figure 5-6 and 5-9), some variation in neutrophil number and therapeutic responses can be attributed to biological differences between donors. Different donors are denoted as biological replicates. To mitigate the influence of donor-dependent differences on experimental outcomes, it is important to repeat experiments with at least 3-4 neutrophil donors (biological replicates) and at least 3 technical replicates per donor. Therefore, to adequately characterize a single experimental condition, a total of 9 wells is needed. Importantly, this requirement is also in place for experiments in lower-throughput transmigration systems. This requirement for high numbers of replicates highlights the importance of scaling up transmigration to 96-well plates.

6.1.3 Functional assay outcomes

Because the ABBA transmigration assay protocol is optimized for high-throughput flow cytometry, neutrophil analysis can be expanded to analysis of functional outcomes in addition to cell surface markers. Specifically, key functional behaviors that can be quantified with flow cytometry include phagocytosis (of either fluorescent beads or fluorescent bacteria (pHrodo particles by ThermoFisher Scientific)); generation of reactive oxygen species (CellROX™ by Invitrogen); and transcription (SYTO™ RNASelect™ by Invitrogen). Additionally, supernatant concentration of cytokines and production of proteases should be quantified for a full picture of neutrophil phenotype post-transmigration. Particularly, MPO and neutrophil elastase are important proteases that can directly influence epithelial-endothelial barrier integrity and should be key outcome

measures. Kits are available to quantify their concentration and activity (abcam ab270204; ab272101; ab111749; ab204730).

6.1.4 *Epithelial and endothelial biological relevance*

The epithelium in the ABBA is a cell line and the endothelial cells are pooled, primary HUVECs. Neither of these is particularly faithful to the real lung cells we are modelling. They provide advantages of standardization and predictability but limit our translational potential. The methods described herein can be applied to primary human epithelial and endothelial cells with minimal modifications.

Further, the barrier generated by the method we developed reflects a healthy lung. For a more accurate representation of pathophysiology, primary epithelium and endothelium from diseased patients is required. For example, patients with COPD and asthma are much more sensitive to changes in air quality than healthy individuals. Culturing the ABBA with COPD-derived epithelium and endothelium compared to healthy donor cells might help us understand why aerosolized pollutants more potently impact COPD lungs and induce neutrophilia whereas they do not have these effects in healthy people.

6.2 Novelty and Future Applications

6.2.1 *Isolation of disease-relevant phenomena*

A primary advantage of *in vitro* models is the ability to completely define and control the microenvironment. *In vitro*, one can easily identify the influence of a specific variable on an outcome of interest. However, *in vitro* models generally lack the complex tissue

architecture, physical stimuli, and cell-cell interactions necessary to recapitulate key events in disease pathophysiology. Therefore, an *in vitro* model that captures tissue architecture, cell-cell interactions, and physical stimuli using human cells in a completely controlled microenvironment greatly expands the range of studies available to investigators of human disease pathophysiology. This is the niche of microphysiological systems. In this section, we present methods to isolate key physiological events in small airway disease using this platform.

6.2.1.1 Fluid mechanical injury of the epithelium

First, we isolated the effects of fluid mechanical stress on the small airway epithelium. This platform enables studies of the specific impact of fluid properties, air pressure and flow rate, and airway diameter on the airway epithelium. These variables may be modulated independently or in concert to determine the interactions between them on the epithelium. This type of study is impossible without such a microphysiological system. Control over ventilation parameters and airway surface liquid properties is not so precise in animals and certainly not in human patients. Learning the impact of these variables on human disease will guide studies of future therapeutic strategies that mitigate the damage of fluid mechanical stress. Is it more important to lower ASL viscosity or surface tension? Are the smallest diameter airways more at risk of fluid mechanical injury than the larger diameter distal airways? Are fluid mechanical injuries contributing to inflammatory mediator production that induces inflammatory cell infiltration? These questions can be answered in future studies using this platform. Ultimately this knowledge can guide targeted therapeutic studies in animals and human patients.

6.2.1.2 Epithelial-endothelial potentiation of barrier properties

Second, we present a high-throughput, small volume model of epithelial-endothelial bilayer co-culture. This bilayer maintains separation of the air and blood in the distal lungs where capillaries and epithelia are in close proximity. Compromised epithelial-endothelial barrier function results in pulmonary edema that can lead to acute lung injury and acute respiratory distress syndrome. Therefore, the ABBA recapitulates this critical bilayer coordination of air-blood barrier function to enable studies of single and combinatorial stimuli on epithelial and endothelial responses, and how these responses result in alterations of barrier function.

Critically, the high-throughput and small volume afforded by the ABBA enable unprecedented investigations of how isolated and combinatorial stimuli impact air-blood barrier function. This is a key advantage of *in vitro* systems: the ability to build a “bottom-up” investigation of various aspects of lung exposure. Similar culture arrangements have been developed in the past to investigate the role of epithelial-endothelial interactions on the potentiation of barrier function and propagation of cell signals. This platform extends that capability to the throughput necessary to investigate these phenomena with unprecedented precision and experimental rigor. Particularly, no previous system has introduced the critical throughput necessary to investigate and compare the effects of large numbers of stimuli on epithelial-endothelial barrier function.

6.2.1.3 Application: atmospheric toxicology

One example application is the study of atmospheric pulmonary toxicology. Air pollutants exist only as a mixture and the contribution of individual pollutants to lung

disease is difficult to discern in the direct study of exposed human lungs. The number of individual pollutant compounds measured in the atmosphere is estimated between 10-100 thousand, greatly exceeding the amount that is reasonable to investigate in animals²⁹⁴. The ABBA can screen up to 96-compounds per plate (or 32 in triplicate) and the preparation and culture of the ABBA plate is completely automatable. Additionally, the outcomes of barrier function, namely permeability and TEER, are compatible with automation. The epithelial and endothelial compartments are accessible for studies of ROS generation, cytotoxicity, and supernatant composition for soluble mediators produced by each cell type. Such a systematic study of both the individual contributions of pollutants, and possible combinatorial interactions between compounds, has never before been possible.

6.2.1.4 Application: ARDS direct and indirect lung injury

Because ARDS is a syndrome rather than a disease with any unifying mechanistic cause, there are multiple injuries that can result in acute respiratory failure leading to ARDS. Particularly, ARDS can result from direct epithelial injuries, such as viral infection or aspiration, and from indirect, or endothelial, injuries such as sepsis. So far, clinical distinctions between direct and indirect lung injury have been identified such as differences in genetic risk factors, likelihood of recovery and complications, etc. However, understanding is limited regarding the influence of specific immunomodulatory therapeutics on the outcomes of patients with direct vs. indirect lung injury. This is in large part due to the challenges of conducting large-scale randomized, controlled trials. Even when such trials are conducted, the mechanisms by which one drug or another is effective are not reasonably discernible in patients due to the number of interfering variables. Therefore, experimental models of therapeutic efficacy *in vitro* are a valuable alternative

for investigating specific therapeutics' likelihood to work on direct vs. indirect lung injury and to investigate potential mechanisms of action that may later be verified with targeted investigations of human samples. The ABBA can model direct or indirect lung injury resulting in loss of barrier function. We demonstrate direct lung injury resultant in barrier loss in Chapter 3 (Figure 3-5(B)). Indirect sepsis-like injury could be simulated with the addition to the endothelial compartment of neutrophil extracellular traps (NETs), damage-associated molecular patterns, pathogen-associated molecular patterns, cytokines, or procoagulant factors²⁹⁵. Further, neutrophil or other immune cell migration in response to this ARDS-mimetic injury could be explored in future studies using the ABBA.

6.2.1.5 Immune cell recruitment in a disease-relevant microenvironment

In Aim 3 we model the recruitment and activation of peripheral blood neutrophils during distal lung inflammation. This assay extends previously established neutrophil recruitment models into a validated, high-throughput assay with well-characterized outcomes that can be compared across conditions and experiments. Therefore, novel combinations of stimuli can be investigated on a single assay plate and the number of combinations is far more reasonable. An illustrative example is the study of protein and metabolite mediators in the development of acute respiratory distress syndrome. Typical studies use -omics on BALF specimens to identify key mediators of ARDS lung disease by comparison of ARDS to healthy samples. However, this top-down approach can only identify correlations, so preclinical studies are needed to confirm their significance. However the numbers of proteins and metabolites with differential levels between the healthy and ARDS lung still exceeds the hundreds for each^{296,297}. Further, the synergistic or antagonistic relationships between multiple key mediators and the resultant effects on

epithelial-endothelial barrier function and neutrophil recruitment is prohibitively difficult to predict *a priori* or *in silico*. Therefore, high-throughput screening of key ARDS-relevant compounds and their effects on the air-blood barrier and neutrophil recruitment would significantly contribute to the net understanding of ARDS lung disease. This platform enables such studies with unprecedented scale and standardization owing to the automation capabilities described previously.

6.2.2 *Dose-response analysis of therapeutics and toxins*

The dose-response curve, describing the quantitative relationship between a defined stimulus and response, was developed in the fields of toxicology and molecular pharmacology. Dose-response relationships are typically employed to discern the molecular mechanisms of action employed by a therapeutic or toxin to exert some predetermined effect on a cellular system²⁹⁸. For molecular therapeutics, the dose-response curve has enabled detailed and testable hypotheses for the drug mechanism of action based on clear cellular readouts such as cell viability or function of a specific target enzyme²⁹⁹.

However, dose-response relationships are also generated *in vivo* that determine the net effects of the test compound on the physiology of a living animal. Specific indicators of a biological process are measured, e.g., cholesterol level, production of target serum biomarkers, blood oxygenation, etc. LD50 curves can be generated that describe the dose of a compound that induces death in 50% of subjects²⁹⁸. These *in vivo* studies provide “top down” information on the potency and physiological effects of a test compound in a complex living system. However, establishment of human relevance in animal studies is

often difficult. Additionally, the precise molecular mechanisms that lead to physiologic outcomes are very difficult to discern in a system as complex as a living animal.

Dose-response relationships in humans are equally as difficult to parse as in animals. While functional and physiologic indicators can be related to exposure to a stimulus, the mechanisms driving this relationship are difficult to identify due to confounding variables and the inability to study pre- and post-exposure outcomes in the same individual.

Therefore, *in vitro* microphysiological systems could reproduce physiology and function in a controlled environment and provide a novel paradigm for the investigation of the relationship between dose and physiology. The ABBA and its neutrophil transmigration assay establish powerful methods for such investigations. We already demonstrated that the ABBA generates dose-response curves for exposure to multiple viruses, soluble organic aerosols, chemokines, and patient-derived airway fluids. Further the ABBA affords multifactorial outputs related directly to physiology including number of migrated cells, epithelial-endothelial barrier function, expression of inflammatory mediators, and endothelial adhesion marker expression. These outcomes enable detailed investigations that may link physiologic associations to molecular mechanisms.

For example, epidemiological studies identified an association between secondary organic aerosol concentration and alterations in lung function, increased incidence of chronic obstructive pulmonary disease exacerbations, and cardiopulmonary-associated deaths¹⁴⁹. Our *in vitro* model showed, quantitatively, that exposure to secondary organic aerosol dose-dependently increased epithelial ROS production and endothelial pro-inflammatory cytokine production. Preliminary data in our model also suggests that both

environmentally derived pollutants and chemically produced secondary organic aerosols may induce a dose-dependent increase in neutrophil infiltration (data not shown). Such findings would strongly support the epidemiological associations between inflammatory lung disease and PM_{2.5} exposure.

The implications of accessible dose-response curve generation in a microphysiological system are far-reaching. Novel studies of both mono-exposure and combinatorial exposure and the associated impact on functional outcomes- primarily barrier function and neutrophil infiltration- have not previously been accessible. The applications of this system to quantitative pharmacology and toxicology are unprecedented.

6.2.3 Patient-specific physiology and drug responses

The ABBA neutrophil transmigration assay demonstrates impressive patient-dependent sensitivity in the detection of both inhibitor (drug) and agonist (chemoattractant) dose-responses. The study of individual donor biology and therapeutic responses is becoming extremely important in clinical medicine³⁰⁰⁻³⁰⁴. Many therapies are already FDA approved, but their efficacy across patients with the same disease presentation is inconsistent. Identification of likely responder patients is a critical step towards improved patient outcomes, especially in critical care³⁰⁰. As an illustrative example, we will describe the application of this assay to the identification of likely responder patients pediatric acute respiratory distress syndrome (PARDS).

Acute respiratory distress syndrome (ARDS) is a severe, life-threatening lung condition defined by acute-onset pulmonary edema and refractory hypoxemia requiring

invasive mechanical ventilation³⁰⁵. Pediatric ARDS (PARDS) can develop in children with influenza, respiratory syncytial virus, and trauma or aspiration injury, and other causes. PARDS has a 20% mortality rate and affects 45,000 children per year in the United States³⁰⁶. While progress in supportive care measures has improved outcomes, no pharmacologic therapies targeting ARDS pathophysiology have reduced mortality in children or adults.

A hallmark of ARDS is the rapid accumulation of pathologically activated neutrophils in the distal pulmonary tract^{68,307–309}. Lung-recruited ARDS neutrophils have increased lifespans and exaggerated degranulation and reactive oxygen species production, but paradoxically decreased bacterial killing capability^{310,311}. Neutrophil degranulation and NETosis products promote inflammation and injure epithelial and endothelial cells, thus interrupting tissue repair^{312–316}. Increased presence of neutrophils, their products, and their chemoattractants are all correlated to increased ARDS severity and mortality^{30,175,177,317}.

Despite the key role of neutrophils in ARDS pathophysiology, neutrophil-targeting therapies have failed to reduce mortality rate and ventilator-free days in clinical trials^{307,318–320}. This lack of progress is in large part attributed to the heterogeneity of ARDS. Its range of etiologies (sepsis, pneumonia, aspiration, trauma) and covariates (e.g., age, sex, race, pre-existing conditions) are thought to substantially influence the resultant molecular and cellular pathobiology so that drug responses are inconsistent across patients, resulting in negative trial results. Indeed, whole blood genomic profiling cannot yield a consistent ARDS gene expression signature³²¹. To address this heterogeneity, trialists attempt to predict treatment responses by subgrouping patients by these variables, or in combination with clinical presentation (e.g., severity score, degree of hypoxia, oxygen dependence).

However, these types of subgrouping have proven to be limited in prediction of intervention responses³²², in large part because clinical presentation, it seems, is relatively disconnected from the underlying pathobiology that would most strongly predict drug response. For example, patients with low blood oxygen and chest infiltrates on x-ray could have vastly disparate inflammatory processes driving the pulmonary edema that causes these symptoms and would therefore respond to differently to the same drugs.

Therefore, trialists want to connect patient-specific pathobiology with potential treatment responses for a plethora of candidate drugs. Researchers have therefore turned to proteomic and metabolomic profiling of peripheral blood and tracheal aspirate to associate treatment response with key biomarkers using machine learning. This strategy has successfully identified several key serum biomarkers that associate with response to simvastatin, fluid management strategy and PEEP strategy^{323–325}. These discoveries were made by a retrospective machine-learning analysis of data from large-scale clinical trials. Such insights may be translatable to other therapeutics, but without understanding the pathobiological significance of the biomarkers discovered by the machine learning model, no useful inferences about other drug responses can be made. Additionally, since the number of candidate therapeutics is ever-growing, conducting individual trials for every therapeutic candidate is virtually unachievable, especially in children. Pediatric patient populations are limited, and coordination of a trial for each available drug candidate is impractical, expensive, and slow, so alternative methods are needed.

Therefore, there is an urgent, unmet need to associate pediatric pathobiology with actionable treatment responses using alternative methods that do not require large-scale clinical trials. We propose that the ABBA could address this need by testing drug responses

in vitro rather than in a clinical trial. With this strategy, we could test more drugs by testing multiple drugs per patient, and we could more confidently determine whether a drug affected physiology by conducting detailed analysis of cells and mediators in the assay. Typical *in vitro* drug testing often cannot capture patient-specific physiology, and its accompanying heterogeneity. Further, typical *in vitro* assays often oversimplify the cell microenvironment and eliminate functional outcomes of importance to disease physiology.

The ABBA neutrophil transmigration assay, however, could use primary patient-specific tracheal aspirate and primary peripheral neutrophils to recapitulate the patient-specific recruitment and activation of peripheral blood neutrophils that migrate into the PARDS lung microenvironment. This small-volume, high-throughput functional assay enables multiplexed drug testing for the assessment of neutrophil-targeted PARDS therapeutics. The assay can be used in the future to link patient-specific pathobiological markers in the blood and/or tracheal aspirate to potential drug responses. This association between pathobiological signature and actionable drug responses is urgently needed to advance the treatment of PARDS. Ultimately, these findings would lay the groundwork for designing future studies of neutrophil-targeted therapy in a subset of children who could most benefit. Finally, the approach described for PARDS can be expanded further other inflammatory lung diseases with heterogeneous presentation and drug responses, such as COPD, CF, bronchiectasis, and viral lower respiratory infection. Such insights are unprecedented and could guide the application of immunomodulators in clinical medicine.

6.2.4 *Generalizability*

The techniques, assays and approaches described here can be expanded to other cell types and diseases with minimal modification. For example, expansion of the ABBA to

primary cells requires only changing the media from RPMI to primary cell medium, while retaining the rest of the protocol in identical fashion. Altering the immune cells is also possible. Other studies using Transwell membranes or equivalent poly(ethylene terephthalate) membranes with 3 μm pore size have demonstrated migration of eosinophils³²⁶, dendritic cells³²⁷, monocytes³²⁸, and lymphocytes³²⁹. Therefore the assay can extend beyond CF and ARDS applications to other lung diseases and even other tissue barriers. Inflammation and barrier function are critical components of disease in the skin, gut, and oral and vaginal mucosa, in addition to the lung.

6.3 Closing statement

In this thesis we present novel platforms for the study of small airway dysfunction. These methods generate novel insights on the relationship between the epithelium, endothelium, and infiltrating neutrophils and enable unprecedented future studies of the impact of therapeutics and toxins on that relationship. Further, these methods enable unprecedented patient-specific studies of pulmonary pathophysiology and therapeutic responses. The methods we present are robustly validated and ready for application to biomedical research questions across pulmonary physiology and medicine.

REFERENCES

1. Viola, H. *et al.* Microphysiological systems modeling acute respiratory distress syndrome that capture mechanical force-induced injury-inflammation-repair. *APL Bioeng.* **3**, 041503 (2019).
2. West, J. B. & Luks, A. *West's Respiratory Physiology: The Essentials.* (Wolters Kluwer, 2016).
3. Hogg, J. C. & Hackett, T.-L. Structure and Function Relationships in Diseases of the Small Airways. *Ann. Am. Thorac. Soc.* **15**, S18–S25 (2018).
4. Hammersley, J. R. & Olson, D. E. Physical models of the smaller pulmonary airways. *J. Appl. Physiol.* **72**, 2402–2414 (1992).
5. Burgel, P.-R. *et al.* Small airways diseases, excluding asthma and COPD: an overview. *Eur. Respir. Rev.* **22**, 131–147 (2013).
6. Barnes, P. J. Small Airways in COPD. *N. Engl. J. Med.* **350**, 2635–2637 (2004).
7. Tirouvanziam, R., Khazaal, I. & Péault, B. Primary inflammation in human cystic fibrosis small airways. *Am. J. Physiol.-Lung Cell. Mol. Physiol.* **283**, L445–L451 (2002).
8. Tiddens, H. A. W. M., Donaldson, S. H., Rosenfeld, M. & Paré, P. D. Cystic fibrosis lung disease starts in the small airways: Can we treat it more effectively? *Pediatr. Pulmonol.* **45**, 107–117 (2010).
9. Morales, M. M. *et al.* Small airway remodeling in acute respiratory distress syndrome: a study in autopsy lung tissue. *Crit. Care* **15**, R4 (2011).

10. Hansell, D. M., Rubens, M. B., Padley, S. P. & Wells, A. U. Obliterative bronchiolitis: individual CT signs of small airways disease and functional correlation. *Radiology* **203**, 721–726 (1997).
11. Agnew, J. E. Bronchiolar aerosol deposition and clearance. *Eur. Respir. J.* **9**, 1118–1122 (1996).
12. Usmani, O. S., Singh, D., Spinola, M., Bizzi, A. & Barnes, P. J. The prevalence of small airways disease in adult asthma: A systematic literature review. *Respir. Med.* **116**, 19–27 (2016).
13. Beers, M. F. & Morrisey, E. E. The three R's of lung health and disease: repair, remodeling, and regeneration. *J. Clin. Invest.* **121**, 2065–2073 (2011).
14. Crosby, L. M. & Waters, C. M. Epithelial repair mechanisms in the lung. *Am. J. Physiol.-Lung Cell. Mol. Physiol.* **298**, L715–L731 (2010).
15. D'Angelo, E., Pecchiari, M. & Gentile, G. Dependence of lung injury on surface tension during low-volume ventilation in normal open-chest rabbits. *J. Appl. Physiol.* **102**, 174–182 (2007).
16. Parker, J. C., Hernandez, L. A. & Peevy, K. J. Mechanisms of ventilator-induced lung injury. *Crit. Care Med.* **21**, 131–143 (1993).
17. Hu, Y. *et al.* A microfluidic model to study fluid dynamics of mucus plug rupture in small lung airways. *Biomicrofluidics* **9**, 044119 (2015).
18. Hill, D. B., Button, B., Rubinstein, M. & Boucher, R. C. Physiology and Pathophysiology of Human Airway Mucus. *Physiol. Rev.* (2022)
doi:10.1152/physrev.00004.2021.

19. Szabari, M. V. *et al.* Relation between Respiratory Mechanics, Inflammation, and Survival in Experimental Mechanical Ventilation. *Am. J. Respir. Cell Mol. Biol.* **60**, 179–188 (2019).
20. Swartz, M. A., Tschumperlin, D. J., Kamm, R. D. & Drazen, J. M. Mechanical stress is communicated between different cell types to elicit matrix remodeling. *Proc. Natl. Acad. Sci. U. S. A.* **98**, 6180–6185 (2001).
21. Tschumperlin, D. J. & Drazen, J. M. Mechanical Stimuli to Airway Remodeling. *Am. J. Respir. Crit. Care Med.* **164**, S90–S94 (2001).
22. Shields, M. D. & Riedler, J. Bronchoalveolar Lavage and Tracheal Aspirate for Assessing Airway Inflammation in Children. *Am. J. Respir. Crit. Care Med.* **162**, S15–S17 (2000).
23. Liao, M. *et al.* Single-cell landscape of bronchoalveolar immune cells in patients with COVID-19. *Nat. Med.* 1–3 (2020) doi:10.1038/s41591-020-0901-9.
24. Xiong, Y. *et al.* Transcriptomic characteristics of bronchoalveolar lavage fluid and peripheral blood mononuclear cells in COVID-19 patients. *Emerg. Microbes Infect.* **9**, 761–770 (2020).
25. Nakos, G., Kitsiouli, E. I., Tsangaris, I. & Lekka, M. E. Bronchoalveolar lavage fluid characteristics of early intermediate and late phases of ARDS. *Intensive Care Med.* **24**, 296–303 (1998).
26. Hoecke, L. V., Job, E. R., Saelens, X. & Roose, K. Bronchoalveolar Lavage of Murine Lungs to Analyze Inflammatory Cell Infiltration. *JoVE J. Vis. Exp.* e55398 (2017) doi:10.3791/55398.

27. Baughman, R. P., Bosken, C. H., Loudon, R. G., Hurtubise, P. & Wesseler, T. Quantitation of Bronchoalveolar Lavage with Methylene Blue. *Am. Rev. Respir. Dis.* **128**, 266–270 (1983).
28. D'Angio, C. T., Basavegowda, K., Avissar, N. E., Finkelstein, J. N. & Sinkin, R. A. Comparison of Tracheal Aspirate and Bronchoalveolar Lavage Specimens from Premature Infants. *Neonatology* **82**, 145–149 (2002).
29. Drusano, G. L. *et al.* Dilution Factor of Quantitative Bacterial Cultures Obtained by Bronchoalveolar Lavage in Patients with Ventilator-Associated Bacterial Pneumonia. *Antimicrob. Agents Chemother.* **62**, e01323-17 (2018).
30. Steinberg, K. P. *et al.* Evolution of bronchoalveolar cell populations in the adult respiratory distress syndrome. *Am. J. Respir. Crit. Care Med.* **150**, 113–122 (1994).
31. Basil, M. C. *et al.* Human distal airways contain a multipotent secretory cell that can regenerate alveoli. *Nature* **604**, 120–126 (2022).
32. Méndez, A. *et al.* Primary infection by Pneumocystis induces Notch-independent Clara cell mucin production in rat distal airways. *PLOS ONE* **14**, e0217684 (2019).
33. Thurman, A. L. *et al.* A Single-Cell Atlas of Large and Small Airways at Birth in a Porcine Model of Cystic Fibrosis. *Am. J. Respir. Cell Mol. Biol.* **66**, 612–622 (2022).
34. Derseh, H. B. *et al.* Small airway remodeling in a sheep model of bleomycin-induced pulmonary fibrosis. *Exp. Lung Res.* **46**, 409–419 (2020).
35. McGonigle, P. & Ruggeri, B. Animal models of human disease: Challenges in enabling translation. *Biochem. Pharmacol.* **87**, 162–171 (2014).

36. Pound, P. & Ritskes-Hoitinga, M. Is it possible to overcome issues of external validity in preclinical animal research? Why most animal models are bound to fail. *J. Transl. Med.* **16**, 1–8 (2018).
37. Boretto, M. *et al.* Patient-derived organoids from endometrial disease capture clinical heterogeneity and are amenable to drug screening. *Nat. Cell Biol.* **21**, 1041–1051 (2019).
38. Reddy, K. *et al.* Subphenotypes in critical care: translation into clinical practice. *Lancet Respir. Med.* **8**, 631–643 (2020).
39. Fulcher, L. M., Gabriel, S., Burns, K. A., Yankaskas, J. R. & Randell, S. H. Well-Differentiated Human Airway Epithelial Cell Cultures. in *Human Cell Culture Protocols* vol. 107 183–206 (Humana Press, 2004).
40. Sweeney, T. E., Lofgren, S., Khatri, P. & Rogers, A. J. Gene Expression Analysis to Assess the Relevance of Rodent Models to Human Lung Injury. *Am. J. Respir. Cell Mol. Biol.* **57**, 184–192 (2017).
41. Seok, J. *et al.* Genomic responses in mouse models poorly mimic human inflammatory diseases. *Proc. Natl. Acad. Sci.* **110**, 3507–3512 (2013).
42. Kamm, R. D. *et al.* Perspective: The promise of multi-cellular engineered living systems. *APL Bioeng.* **2**, 040901 (2018).
43. Wirtz, H. R. & Dobbs, L. G. The effects of mechanical forces on lung functions. *Respir. Physiol.* **119**, 1–17 (2000).
44. Liu, M., Tanswell, A. K. & Post, M. Mechanical force-induced signal transduction in lung cells. *Am. J. Physiol.-Lung Cell. Mol. Physiol.* **277**, L667–L683 (1999).

45. Waters, C. M., Roan, E. & Navajas, D. Mechanobiology in Lung Epithelial Cells: Measurements, Perturbations, and Responses. in *Comprehensive Physiology* (ed. Terjung, R.) (John Wiley & Sons, Inc., 2012). doi:10.1002/cphy.c100090.
46. Albert, R. K. The Role of Ventilation-induced Surfactant Dysfunction and Atelectasis in Causing Acute Respiratory Distress Syndrome. *Am. J. Respir. Crit. Care Med.* **185**, 702–708 (2012).
47. Grotberg, J. B. Crackles and Wheezes: Agents of Injury? *Ann. Am. Thorac. Soc.* **16**, 967–969 (2019).
48. dos Santos, C. C. & Slutsky, A. S. The Contribution of Biophysical Lung Injury to the Development of Biotrauma. *Annu. Rev. Physiol.* **68**, 585–618 (2006).
49. Bilek, A. M., Dee, K. C. & Gaver, D. P. Mechanisms of surface-tension-induced epithelial cell damage in a model of pulmonary airway reopening. *J. Appl. Physiol.* **94**, 770–783 (2003).
50. Yalcin, H. C., Perry, S. F. & Ghadiali, S. N. Influence of airway diameter and cell confluence on epithelial cell injury in an in vitro model of airway reopening. *J. Appl. Physiol.* **103**, 1796–1807 (2007).
51. Kay, S. S., Bilek, A. M., Dee, K. C. & Gaver, D. P. Pressure gradient, not exposure duration, determines the extent of epithelial cell damage in a model of pulmonary airway reopening. *J. Appl. Physiol.* **97**, 269–276 (2004).
52. Higueta-Castro, N., Mihai, C., Hansford, D. J. & Ghadiali, S. N. Influence of airway wall compliance on epithelial cell injury and adhesion during interfacial flows. *J. Appl. Physiol.* **117**, 1231–1242 (2014).

53. Huh, D. *et al.* Acoustically detectable cellular-level lung injury induced by fluid mechanical stresses in microfluidic airway systems. *Proc. Natl. Acad. Sci. U. S. A.* **104**, 18886–18891 (2007).
54. Tavana, H., Zamankhan, P., Christensen, P. J., Grotberg, J. B. & Takayama, S. Epithelium damage and protection during reopening of occluded airways in a physiologic microfluidic pulmonary airway model. *Biomed. Microdevices* **13**, 731–742 (2011).
55. Fujioka, H., Takayama, S. & Grotberg, J. B. Unsteady propagation of a liquid plug in a liquid-lined straight tube. *Phys. Fluids* **20**, 062104 (2008).
56. Hassan, E. A., Uzgoren, E., Fujioka, H., Grotberg, J. B. & Shyy, W. Adaptive Lagrangian-Eulerian computation of propagation and rupture of a liquid plug in a tube. *Int. J. Numer. Methods Fluids* **67**, 1373–1392 (2011).
57. Muradoglu, M., Romanò, F., Fujioka, H. & Grotberg, J. B. Effects of surfactant on propagation and rupture of a liquid plug in a tube. *J. Fluid Mech.* **872**, 407–437 (2019).
58. Douville, N. J. *et al.* Combination of fluid and solid mechanical stresses contribute to cell death and detachment in a microfluidic alveolar model. *Lab Chip* **11**, 609–619 (2011).
59. Jacob, A.-M. & Gaver, D. P. Atelectrauma disrupts pulmonary epithelial barrier integrity and alters the distribution of tight junction proteins ZO-1 and claudin 4. *J. Appl. Physiol.* **113**, 1377–1387 (2012).

60. Higueta-Castro, N. *et al.* Using a Novel Microfabricated Model of the Alveolar-Capillary Barrier to Investigate the Effect of Matrix Structure on Atelectrauma. *Sci. Rep.* **7**, 1–13 (2017).
61. Albelda, S. M. Endothelial and Epithelial Cell Adhesion Molecules. *Am. J. Respir. Cell Mol. Biol.* **4**, 195–203 (1991).
62. Leckband, D. E., le Duc, Q., Wang, N. & de Rooij, J. Mechanotransduction at cadherin-mediated adhesions. *Curr. Opin. Cell Biol.* **23**, 523–530 (2011).
63. Ma, X. *et al.* Fibers in the Extracellular Matrix Enable Long-Range Stress Transmission between Cells. *Biophys. J.* **104**, 1410–1418 (2013).
64. Nieman, G. F., Gatto, L. A. & Habashi, N. M. Impact of mechanical ventilation on the pathophysiology of progressive acute lung injury. *J. Appl. Physiol.* **119**, 1245–1261 (2015).
65. Nieman, G. F. *et al.* Acute lung injury: how to stabilize a broken lung. *Crit. Care* **22**, 136 (2018).
66. Amratia, D. A., Viola, H. & Ioachimescu, O. C. Glucocorticoid therapy in respiratory illness: bench to bedside. *J. Investig. Med.* (2022) doi:10.1136/jim-2021-002161.
67. Moldoveanu, B. *et al.* Inflammatory mechanisms in the lung. *J. Inflamm. Res.* **2**, 1–11 (2008).
68. Williams, A. E. & Chambers, R. C. The mercurial nature of neutrophils: still an enigma in ARDS? *Am. J. Physiol.-Lung Cell. Mol. Physiol.* **306**, L217–L230 (2013).

69. Butler, A., Walton, G. M. & Sapey, E. Neutrophilic Inflammation in the Pathogenesis of Chronic Obstructive Pulmonary Disease. *COPD J. Chronic Obstr. Pulm. Dis.* **0**, 1–13 (2018).
70. Chang, H. S. *et al.* Neutrophilic inflammation in asthma: mechanisms and therapeutic considerations. *Expert Rev. Respir. Med.* **11**, 29–40 (2017).
71. Zheng, L. *et al.* Airway neutrophilia in stable and bronchiolitis obliterans syndrome patients following lung transplantation. *Thorax* **55**, 53–59 (2000).
72. Wang, S.-Z. & Forsyth, K. D. The interaction of neutrophils with respiratory epithelial cells in viral infection. *Respirology* **5**, 1–9 (2000).
73. Giacalone, V. D., Margaroli, C., Mall, M. A. & Tirouvanziam, R. Neutrophil Adaptations upon Recruitment to the Lung: New Concepts and Implications for Homeostasis and Disease. *Int. J. Mol. Sci.* **21**, 851 (2020).
74. Barkal, L. J. *et al.* Microbial volatile communication in human organotypic lung models. *Nat. Commun.* **8**, (2017).
75. Huh, D. *et al.* A Human Disease Model of Drug Toxicity–Induced Pulmonary Edema in a Lung-on-a-Chip Microdevice. *Sci. Transl. Med.* **4**, 159ra147-159ra147 (2012).
76. Choe, M. M., Sporn, P. H. S. & Swartz, M. A. Extracellular Matrix Remodeling by Dynamic Strain in a Three-Dimensional Tissue-Engineered Human Airway Wall Model. *Am. J. Respir. Cell Mol. Biol.* **35**, 306–313 (2006).
77. Ventura, B. D., Lemerle, C., Michalodimitrakis, K. & Serrano, L. From in vivo to in silico biology and back. *Nature* **443**, 527–533 (2006).

78. Benam, K. H. *et al.* Matched-Comparative Modeling of Normal and Diseased Human Airway Responses Using a Microengineered Breathing Lung Chip. *Cell Syst.* **3**, 456-466.e4 (2016).
79. Sellgren, K. L., Butala, E. J., Gilmour, B. P., Randell, S. H. & Grego, S. A. biomimetic multicellular model of the airways using primary human cells. *Lab Chip* **14**, 3349–3358 (2014).
80. Mertz, D. R., Ahmed, T. & Takayama, S. Engineering cell heterogeneity into organs-on-a-chip. *Lab. Chip* **18**, 2378–2395 (2018).
81. Henry, O. F. H. *et al.* Organs-on-chips with integrated electrodes for trans-epithelial electrical resistance (TEER) measurements of human epithelial barrier function. *Lab. Chip* **17**, 2264–2271 (2017).
82. Felder, M. *et al.* Impaired Wound Healing of Alveolar Lung Epithelial Cells in a Breathing Lung-On-A-Chip. *Front. Bioeng. Biotechnol.* **7**, (2019).
83. Felder, M., Stucki, A. O., Stucki, J. D., Geiser, T. & Guenat, O. T. The potential of microfluidic lung epithelial wounding: towards in vivo-like alveolar microinjuries. *Integr. Biol. Quant. Biosci. Nano Macro* **6**, 1132–1140 (2014).
84. Glindmeyer, H. W., Smith, B. J. & Gaver, D. P. In situ enhancement of pulmonary surfactant function using temporary flow reversal. *J. Appl. Physiol.* **112**, 149–158 (2011).
85. Aogáin, M. *et al.* Distinct “Immunoallertypes” of Disease and High Frequencies of Sensitization in Non–Cystic Fibrosis Bronchiectasis. *Am. J. Respir. Crit. Care Med.* **199**, 842–853 (2018).

86. King, G. G., James, A., Harkness, L. & Wark, P. A. B. Pathophysiology of severe asthma: We've only just started. *Respirology* **23**, 262–271 (2018).
87. Pezzulo, A. A. *et al.* Glucose Depletion in the Airway Surface Liquid Is Essential for Sterility of the Airways. *PLOS ONE* **6**, e16166 (2011).
88. Chen, Z. *et al.* Determination of rheology and surface tension of airway surface liquid: a review of clinical relevance and measurement techniques. *Respir. Res.* **20**, 1–14 (2019).
89. Boucher, R. Regulation of airway surface liquid volume by human airway epithelia. *Pflüg. Arch.* **445**, 495–498 (2003).
90. Grotberg, J. B. Respiratory fluid mechanics. *Phys. Fluids* **23**, 021301 (2011).
91. Ghadiali, S. N. & Gaver, D. P. Biomechanics of liquid–epithelium interactions in pulmonary airways. *Respir. Physiol. Neurobiol.* **163**, 232–243 (2008).
92. Tavana, H. *et al.* Dynamics of Liquid Plugs of Buffer and Surfactant Solutions in a Micro-Engineered Pulmonary Airway Model. *Langmuir* **26**, 3744–3752 (2010).
93. Stringer, C., Wang, T., Michaelos, M. & Pachitariu, M. Cellpose: a generalist algorithm for cellular segmentation. *Nat. Methods* **18**, 100–106 (2021).
94. Weibel, E. R. & Gomez, D. M. Architecture of the Human Lung: Use of quantitative methods establishes fundamental relations between size and number of lung structures. *Science* **137**, 577–585 (1962).
95. Guckenberger, D. J., Groot, T. E. de, Wan, A. M. D., Beebe, D. J. & Young, E. W. K. Micromilling: a method for ultra-rapid prototyping of plastic microfluidic devices. *Lab. Chip* **15**, 2364–2378 (2015).

96. Fahy, J. V. & Dickey, B. F. Airway Mucus Function and Dysfunction. *N. Engl. J. Med.* **363**, 2233–2247 (2010).
97. Lin, V. Y. *et al.* Excess mucus viscosity and airway dehydration impact COPD airway clearance. *Eur. Respir. J.* **55**, (2020).
98. Dunican, E. M. *et al.* Mucus plugs in patients with asthma linked to eosinophilia and airflow obstruction. *J. Clin. Invest.* **128**, 997–1009 (2018).
99. Fujioka, H. & Grotberg, J. B. Steady Propagation of a Liquid Plug in a Two-Dimensional Channel. *J. Biomech. Eng.* **126**, 567–577 (2004).
100. Viola, H. *et al.* A High-Throughput Distal Lung Air–Blood Barrier Model Enabled By Density-Driven Underside Epithelium Seeding. *Adv. Healthc. Mater.* 2100879 (2021) doi:10.1002/adhm.202100879.
101. Haghnegahdar, A., Zhao, J. & Feng, Y. Lung aerosol dynamics of airborne influenza A virus-laden droplets and the resultant immune system responses: An in silico study. *J. Aerosol Sci.* **134**, 34–55 (2019).
102. Darquenne, C. Aerosol Deposition in Health and Disease. *J. Aerosol Med. Pulm. Drug Deliv.* **25**, 140–147 (2012).
103. Gobel, J. *et al.* A Phenotypic High-Throughput Screen with RSV-Infected Primary Human Small Airway Epithelial Cells (SAECs). *J. Biomol. Screen.* **20**, 729–738 (2015).
104. Bluhmki, T. *et al.* Development of a miniaturized 96-Transwell air–liquid interface human small airway epithelial model. *Sci. Rep.* **10**, 13022 (2020).

105. Gard, A. L. *et al.* High-Throughput Human Primary Cell-Based Airway Model for Evaluating Influenza, Coronavirus, or other Respiratory Viruses *in vitro*. *bioRxiv* 2020.05.23.112797 (2020) doi:10.1101/2020.05.23.112797.
106. Salomon, J. J. *et al.* The Cell Line NCI-H441 Is a Useful *in Vitro* Model for Transport Studies of Human Distal Lung Epithelial Barrier. *Mol. Pharm.* **11**, 995–1006 (2014).
107. Huang, S. *et al.* Establishment and characterization of an *in vitro* human small airway model (SmallAir™). *Eur. J. Pharm. Biopharm.* **118**, 68–72 (2017).
108. Bhowmick, R. & Gappa-Fahlenkamp, H. Cells and Culture Systems Used to Model the Small Airway Epithelium. *Lung* **194**, 419–428 (2016).
109. Schlingmann, B., Molina, S. A. & Koval, M. Claudins: Gatekeepers of lung epithelial function. *Semin. Cell Dev. Biol.* **42**, 47–57 (2015).
110. Blume, C. *et al.* Cellular crosstalk between airway epithelial and endothelial cells regulates barrier functions during exposure to double-stranded RNA. *Immun. Inflamm. Dis.* **5**, 45–56 (2017).
111. Maniatis, N. A., Kotanidou, A., Catravas, J. D. & Orfanos, S. E. Endothelial pathomechanisms in acute lung injury. *Vascul. Pharmacol.* **49**, 119–133 (2008).
112. Janga, H. *et al.* Site-specific and endothelial-mediated dysfunction of the alveolar-capillary barrier in response to lipopolysaccharides. *J. Cell. Mol. Med.* **22**, 982–998 (2018).
113. Lentsch, A. B. & Ward, P. A. Regulation of inflammatory vascular damage. *J. Pathol.* **190**, 343–348 (2000).

114. Tam, A., Wadsworth, S., Dorscheid, D., Man, S. F. P. & Sin, D. D. The airway epithelium: more than just a structural barrier. *Ther. Adv. Respir. Dis.* **5**, 255–273 (2011).
115. Bdeir, K. *et al.* Neutrophil α -Defensins Cause Lung Injury by Disrupting the Capillary–Epithelial Barrier. *Am. J. Respir. Crit. Care Med.* **181**, 935–946 (2010).
116. Ichikawa, A. *et al.* CXCL10-CXCR3 Enhances the Development of Neutrophil-mediated Fulminant Lung Injury of Viral and Nonviral Origin. *Am. J. Respir. Crit. Care Med.* **187**, 65–77 (2013).
117. Hulme, K. D. *et al.* High glucose levels increase influenza-associated damage to the pulmonary epithelial-endothelial barrier. *eLife* **9**, e56907 (2020).
118. Short, K. R. *et al.* Influenza virus damages the alveolar barrier by disrupting epithelial cell tight junctions. *Eur. Respir. J.* **47**, 954–966 (2016).
119. Kasper, J. *et al.* Inflammatory and cytotoxic responses of an alveolar-capillary coculture model to silica nanoparticles: Comparison with conventional monocultures. *Part. Fibre Toxicol.* **8**, 6 (2011).
120. Klein, S. G., Serchi, T., Hoffmann, L., Blömeke, B. & Gutleb, A. C. An improved 3D tetraculture system mimicking the cellular organisation at the alveolar barrier to study the potential toxic effects of particles on the lung. *Part. Fibre Toxicol.* **10**, 31 (2013).
121. Emmeler, J. *et al.* Assessment of Alterations in Barrier Functionality and Induction of Proinflammatory and Cytotoxic Effects After Sulfur Mustard Exposure of an In Vitro Coculture Model of the Human Alveolo-Capillary Barrier. *Inhal. Toxicol.* **19**, 657–665 (2007).

122. Hermanns, M. I. *et al.* Assessment of respiratory sensitizers: Cytokine responses in a 3D alveolo-capillary barrier model in vitro. *Adv. Biomater. Devices Med.* **2**, (2015).
123. Papritz, M. *et al.* Side-specific effects by cadmium exposure: Apical and basolateral treatment in a coculture model of the blood–air barrier. *Toxicol. Appl. Pharmacol.* **245**, 361–369 (2010).
124. Willems, C. H. M. P. *et al.* Alveolocapillary model system to study alveolar re-epithelialization. *Exp. Cell Res.* **319**, 64–74 (2013).
125. Dohle, E. *et al.* Human Co- and Triple-Culture Model of the Alveolar-Capillary Barrier on a Basement Membrane Mimic. *Tissue Eng. Part C Methods* **24**, 495–503 (2018).
126. Costa, A., de Souza Carvalho-Wodarz, C., Seabra, V., Sarmiento, B. & Lehr, C.-M. Triple co-culture of human alveolar epithelium, endothelium and macrophages for studying the interaction of nanocarriers with the air-blood barrier. *Acta Biomater.* **91**, 235–247 (2019).
127. Wepler, A., Rowter, D., Hermanns, I., Kirkpatrick, C. J. & Issekutz, A. C. Modulation of Endotoxin-Induced Neutrophil Transendothelial Migration by Alveolar Epithelium in a Defined Bilayer Model. *Exp. Lung Res.* **32**, 455–482 (2006).
128. Huh, D. *et al.* Reconstituting Organ-Level Lung Functions on a Chip. *Science* **328**, 1662–1668 (2010).
129. Drasler, B. *et al.* An Inflamed Human Alveolar Model for Testing the Efficiency of Anti-inflammatory Drugs in vitro. *Front. Bioeng. Biotechnol.* **8**, 987 (2020).

130. Benam, K. H. *et al.* Small airway-on-a-chip enables analysis of human lung inflammation and drug responses in vitro. *Nat. Methods* **13**, 151–157 (2016).
131. Chowdhury, F., Howat, W. J., Phillips, G. J. & Lackie, P. M. Interactions between endothelial cells and epithelial cells in a combined cell model of airway mucosa: effects on tight junction permeability. *Exp. Lung Res.* **36**, 1–11 (2010).
132. Papazian, D., Würtzen, P. A. & Hansen, S. W. K. Polarized Airway Epithelial Models for Immunological Co-Culture Studies. *Int. Arch. Allergy Immunol.* **170**, 1–21 (2016).
133. Mackowiak, B., Wang, H. & Li, L. Inverted culture plate system for cellular co-culture. (2019).
134. Ren, H., Birch, N. P. & Suresh, V. An Optimised Human Cell Culture Model for Alveolar Epithelial Transport. *PLOS ONE* **11**, e0165225 (2016).
135. Gazdar, A. F. *et al.* Peripheral Airway Cell Differentiation in Human Lung Cancer Cell Lines. *Cancer Res.* **50**, 5481–5487 (1990).
136. Zuo, W.-L. *et al.* Ontogeny and Biology of Human Small Airway Epithelial Club Cells. *Am. J. Respir. Crit. Care Med.* **198**, 1375–1388 (2018).
137. Rokicki, W., Rokicki, M., Wojtacha, J. & Dželjijli, A. The role and importance of club cells (Clara cells) in the pathogenesis of some respiratory diseases. *Kardiochirurgia Torakochirurgia Pol. Pol. J. Cardio-Thorac. Surg.* **13**, 26–30 (2016).
138. Hermanns, M. I., Unger, R. E., Kehe, K., Peters, K. & Kirkpatrick, C. J. Lung epithelial cell lines in coculture with human pulmonary microvascular endothelial

- cells: development of an alveolo-capillary barrier in vitro. *Lab. Invest.* **84**, 736 (2004).
139. del Vecchio, P. J. *et al.* Culture and characterization of pulmonary microvascular endothelial cells. *Vitro Cell. Dev. Biol. - Anim.* **28**, 711–715 (1992).
140. Medina-Leyte, D. J., Domínguez-Pérez, M., Mercado, I., Villarreal-Molina, M. T. & Jacobo-Albavera, L. Use of Human Umbilical Vein Endothelial Cells (HUVEC) as a Model to Study Cardiovascular Disease: A Review. *Appl. Sci.* **10**, 938 (2020).
141. OptiPrep™ (Iodixanol) Density Gradient Medium | STEMCELL Technologies. https://www.stemcell.com/optipreptm.html#product.info.scientific_resources.
142. Grover, W. H. *et al.* Measuring single-cell density. *Proc. Natl. Acad. Sci.* **108**, 10992–10996 (2011).
143. Hermanns Maria Iris *et al.* An impaired alveolar-capillary barrier in vitro: effect of proinflammatory cytokines and consequences on nanocarrier interaction. *J. R. Soc. Interface* **7**, S41–S54 (2010).
144. Mul, F. P. J. *et al.* Sequential migration of neutrophils across monolayers of endothelial and epithelial cells. *J. Leukoc. Biol.* **68**, 529–537 (2000).
145. Nishiguchi, A., Singh, S., Wessling, M., Kirkpatrick, C. J. & Möller, M. Basement Membrane Mimics of Biofunctionalized Nanofibers for a Bipolar-Cultured Human Primary Alveolar-Capillary Barrier Model. *Biomacromolecules* **18**, 719–727 (2017).
146. Bhattacharya, R. F. H., Sunita Bhattacharya, Jahar. Crosstalk signaling between alveoli and capillaries - Rebecca F. Hough, Sunita Bhattacharya, Jahar Bhattacharya, 2018. *Pulm. Circ.* (2018).

147. Fischer, S. *et al.* Signaling mechanism of extracellular RNA in endothelial cells. *FASEB J.* **23**, 2100–2109 (2009).
148. Kroll, J. H. & Seinfeld, J. H. Chemistry of secondary organic aerosol: Formation and evolution of low-volatility organics in the atmosphere. *Atmos. Environ.* **42**, 3593–3624 (2008).
149. Déméautis, T. *et al.* Pathogenic Mechanisms of Secondary Organic Aerosols. *Chem. Res. Toxicol.* (2022) doi:10.1021/acs.chemrestox.1c00353.
150. Ito, T., Bekki, K., Fujitani, Y. & Hirano, S. The toxicological analysis of secondary organic aerosol in human lung epithelial cells and macrophages. *Environ. Sci. Pollut. Res.* **26**, 22747–22755 (2019).
151. Chowdhury, P. H. *et al.* Connecting the Oxidative Potential of Secondary Organic Aerosols with Reactive Oxygen Species in Exposed Lung Cells. *Environ. Sci. Technol.* **53**, 13949–13958 (2019).
152. Nawroth, J. C. *et al.* A Microengineered Airway Lung Chip Models Key Features of Viral-induced Exacerbation of Asthma. *Am. J. Respir. Cell Mol. Biol.* **63**, 591–600 (2020).
153. Frampton, J. P. *et al.* Rapid Self-Assembly of Macroscale Tissue Constructs at Biphasic Aqueous Interfaces. *Adv. Funct. Mater.* **25**, 1694–1699 (2015).
154. Han, C., Takayama, S. & Park, J. Formation and manipulation of cell spheroids using a density adjusted PEG/DEX aqueous two phase system. *Sci. Rep.* **5**, 11891 (2015).
155. Chandrasekaran, A. *et al.* Magnetic microboats for floating, stiffness tunable, air-liquid interface epithelial cultures. *Lab. Chip* **19**, 2786–2798 (2019).

156. Farkas, D. *et al.* Toll-like Receptor 3 Is a Therapeutic Target for Pulmonary Hypertension. *Am. J. Respir. Crit. Care Med.* **199**, 199–210 (2018).
157. Ito, Y. *et al.* Influenza induces IL-8 and GM-CSF secretion by human alveolar epithelial cells through HGF/c-Met and TGF- α /EGFR signaling. *Am. J. Physiol.-Lung Cell. Mol. Physiol.* **308**, L1178–L1188 (2015).
158. Pothlichet, J. *et al.* Type I IFN Triggers RIG-I/TLR3/NLRP3-dependent Inflammasome Activation in Influenza A Virus Infected Cells. *PLOS Pathog.* **9**, e1003256 (2013).
159. Larson, B., Banks, P., Sherman, H. & Rothenberg, M. Automation of Cell-Based Drug Absorption Assays in 96-Well Format Using Permeable Support Systems. *J. Lab. Autom.* **17**, 222–232 (2012).
160. Zang, R., Li, D., Tang, I.-C., Wang, J. & Yang, S.-T. Cell-Based Assays in High-Throughput Screening for Drug Discovery. *Int. J. Biotechnol. Wellness Ind.* **1**, 31–51 (2012).
161. Kasper, J. Y., Hermanns, M. I., Unger, R. E. & Kirkpatrick, C. J. A responsive human triple-culture model of the air–blood barrier: incorporation of different macrophage phenotypes. *J. Tissue Eng. Regen. Med.* **11**, 1285–1297 (2017).
162. Summers, C. Chasing the ‘Holy Grail’ – Modulating Neutrophils in Inflammatory Lung Disease. *Am. J. Respir. Crit. Care Med.* (2019) doi:10.1164/rccm.201902-0333ED.
163. Mortaz, E., Alipoor, S. D., Adcock, I. M., Mumby, S. & Koenderman, L. Update on Neutrophil Function in Severe Inflammation. *Front. Immunol.* **9**, (2018).

164. Petri, B. & Sanz, M.-J. Neutrophil chemotaxis. *Cell Tissue Res.* **371**, 425–436 (2018).
165. Amulic, B., Cazalet, C., Hayes, G. L., Metzler, K. D. & Zychlinsky, A. Neutrophil Function: From Mechanisms to Disease. *Annu. Rev. Immunol.* **30**, 459–489 (2012).
166. Khajah, M. *Role of Neutrophils in Disease Pathogenesis*. (BoD – Books on Demand, 2017).
167. Rebetz, J., Semple, J. W. & Kapur, R. The Pathogenic Involvement of Neutrophils in Acute Respiratory Distress Syndrome and Transfusion-Related Acute Lung Injury. *Transfus. Med. Hemotherapy* **45**, 290–298 (2018).
168. Abraham, E. Neutrophils and acute lung injury. *Crit. Care Med.* **31**, S195 (2003).
169. Camp, J. V. & Jonsson, C. B. *A role for neutrophils in viral respiratory disease*. *Frontiers in Immunology* vol. 8 (Frontiers Media S.A., 2017).
170. Borges, L., Pithon-Curi, T. C., Curi, R. & Hatanaka, E. COVID-19 and Neutrophils: The Relationship between Hyperinflammation and Neutrophil Extracellular Traps. *Mediators Inflamm.* **2020**, e8829674 (2020).
171. Cavallaro, E. C., Liang, K.-K., Lawrence, M. D., Forsyth, K. D. & Dixon, D.-L. Neutrophil infiltration and activation in bronchiolitic airways are independent of viral etiology. *Pediatr. Pulmonol.* **52**, 238–246 (2017).
172. Laval, J., Ralhan, A. & Hartl, D. Neutrophils in cystic fibrosis. *Biol. Chem.* **397**, 485–496 (2016).
173. Forrest, O. A. *et al.* Frontline Science: Pathological conditioning of human neutrophils recruited to the airway milieu in cystic fibrosis. *J. Leukoc. Biol.* **104**, 665–675 (2018).

174. Margaroli, C. *et al.* Transcriptional firing represses bactericidal activity in cystic fibrosis airway neutrophils. *Cell Rep. Med.* **2**, 100239 (2021).
175. Yang, S.-C., Tsai, Y.-F., Pan, Y.-L. & Hwang, T.-L. Understanding the role of neutrophils in acute respiratory distress syndrome. *Biomed. J.* (2020)
doi:10.1016/j.bj.2020.09.001.
176. Jasper, A. E., McIver, W. J., Sapey, E. & Walton, G. M. Understanding the role of neutrophils in chronic inflammatory airway disease. *F1000Research* **8**, F1000 Faculty Rev-557 (2019).
177. Potey, P. M., Rossi, A. G., Lucas, C. D. & Dorward, D. A. Neutrophils in the initiation and resolution of acute pulmonary inflammation: understanding biological function and therapeutic potential. *J. Pathol.* **247**, 672–685 (2019).
178. Mårdh, C. K. *et al.* Targets of Neutrophil Influx and Weaponry: Therapeutic Opportunities for Chronic Obstructive Airway Disease. *J. Immunol. Res.* **2017**, e5273201 (2017).
179. De Volder, J., Vereecke, L., Joos, G. & Maes, T. Targeting neutrophils in asthma: A therapeutic opportunity? *Biochem. Pharmacol.* **182**, 114292 (2020).
180. Hazeldine, J. & Lord, J. M. Neutrophils and COVID-19: Active Participants and Rational Therapeutic Targets. *Front. Immunol.* **12**, (2021).
181. Kruger, P. S. & Terblanche, M. Statins in patients with sepsis and ARDS: is it over? No. *Intensive Care Med.* **43**, 675–676 (2017).
182. Janda, S., Park, K., FitzGerald, J. M., Etminan, M. & Swiston, J. Statins in COPD: A Systematic Review. *Chest* **136**, 734–743 (2009).

183. So, J. Y., Dhungana, S., Beros, J. J. & Criner, G. J. Statins in the treatment of COPD and asthma—where do we stand? *Curr. Opin. Pharmacol.* **40**, 26–33 (2018).
184. Mandal, P. *et al.* Atorvastatin as a stable treatment in bronchiectasis: a randomised controlled trial. *Lancet Respir. Med.* **2**, 455–463 (2014).
185. Sadhra, C. S. *et al.* S114 Simvastatin improves neutrophil migratory targeting in COPD: in vitro studies supporting Statin use as a potential adjuvant therapy. *Thorax* **68**, A59–A60 (2013).
186. Bradbury, P., Traini, D., Ammit, A. J., Young, P. M. & Ong, H. X. Repurposing of statins via inhalation to treat lung inflammatory conditions. *Adv. Drug Deliv. Rev.* **133**, 93–106 (2018).
187. Hothersall, E., McSharry, C. & Thomson, N. C. Potential therapeutic role for statins in respiratory disease. *Thorax* **61**, 729–734 (2006).
188. Feldman, C. The Role of Statins in Respiratory Diseases. *Clin. Pulm. Med.* **16**, 95–100 (2009).
189. Marzilli, M. Pleiotropic Effects of Statins. *Am. J. Cardiovasc. Drugs* **10**, 3–9 (2010).
190. Chan, E. D., Chan, M. M., Chan, M. M. & Marik, P. E. Use of glucocorticoids in the critical care setting: Science and clinical evidence. *Pharmacol. Ther.* **206**, 107428 (2020).
191. McEvoy, C. E. & Niewoehner, D. E. Adverse Effects of Corticosteroid Therapy for COPD: A Critical Review. *Chest* **111**, 732–743 (1997).
192. Walsh, L. J. *et al.* Adverse effects of oral corticosteroids in relation to dose in patients with lung disease. *Thorax* **56**, 279–284 (2001).

193. Golomb, B. A. & Evans, M. A. Statin Adverse Effects. *Am. J. Cardiovasc. Drugs* **8**, 373–418 (2008).
194. Németh, T., Sperandio, M. & Mócsai, A. Neutrophils as emerging therapeutic targets. *Nat. Rev. Drug Discov.* **19**, 253–275 (2020).
195. Xie, Z., Yang, X., Duan, Y., Han, J. & Liao, C. Small-Molecule Kinase Inhibitors for the Treatment of Nononcologic Diseases. *J. Med. Chem.* **64**, 1283–1345 (2021).
196. Jamilloux, Y. *et al.* JAK inhibitors for the treatment of autoimmune and inflammatory diseases. *Autoimmun. Rev.* **18**, 102390 (2019).
197. Yang, Y., Wang, H., Kouadir, M., Song, H. & Shi, F. Recent advances in the mechanisms of NLRP3 inflammasome activation and its inhibitors. *Cell Death Dis.* **10**, 1–11 (2019).
198. Ben-Akiva, E., Witte, S. E., Meyer, R., Rhodes, K. & Green, J. Polymeric micro- and nanoparticles for immune modulation. *Biomater. Sci.* **7**, 14–30 (2019).
199. Mejías, J. C. *et al.* Neutrophil-targeted, protease-activated pulmonary drug delivery blocks airway and systemic inflammation. *JCI Insight* **4**, e131468.
200. Hafeez, U., Gan, H. K. & Scott, A. M. Monoclonal antibodies as immunomodulatory therapy against cancer and autoimmune diseases. *Curr. Opin. Pharmacol.* **41**, 114–121 (2018).
201. Yeo, J. & Shahidi, F. Chapter 1 - Bioactive peptides in health and disease: an overview. in *Biologically Active Peptides* (eds. Toldrá, F. & Wu, J.) 1–26 (Academic Press, 2021). doi:10.1016/B978-0-12-821389-6.00007-8.
202. Jani, M. S., Veetil, A. T. & Krishnan, Y. Precision immunomodulation with synthetic nucleic acid technologies. *Nat. Rev. Mater.* **4**, 451–458 (2019).

203. Huang, G. *et al.* Neutrophilic Inflammation in the Immune Responses of Chronic Obstructive Pulmonary Disease: Lessons from Animal Models. *J. Immunol. Res.* **2017**, e7915975 (2017).
204. Knapp, S. LPS and bacterial lung inflammation models. *Drug Discov. Today Dis. Models* **6**, 113–118 (2009).
205. Lin, S. *et al.* Comparison of the transcriptional landscapes between human and mouse tissues. *Proc. Natl. Acad. Sci.* **111**, 17224–17229 (2014).
206. Irimia, D. & Wang, X. Inflammation-on-a-Chip: Probing the Immune System Ex Vivo. *Trends Biotechnol.* **36**, 923–937 (2018).
207. Casale, T. B. & Carolan, E. J. Cytokine-induced sequential migration of neutrophils through endothelium and epithelium. *Inflamm. Res.* **48**, 22–27 (1999).
208. Kidney, J. C. & Proud, D. Neutrophil Transmigration across Human Airway Epithelial Monolayers. *Am. J. Respir. Cell Mol. Biol.* **23**, 389–395 (2000).
209. Cramer, E. B., Milks, L. C. & Ojakian, G. K. Transepithelial migration of human neutrophils: an in vitro model system. *Proc. Natl. Acad. Sci.* **77**, 4069–4073 (1980).
210. Casale, T. B. & Abbas, M. K. Comparison of leukotriene B₄-induced neutrophil migration through different cellular barriers. *Am. J. Physiol.-Cell Physiol.* **258**, C639–C647 (1990).
211. Liu, L., Mul, F. P., Lutter, R., Roos, D. & Knol, E. F. Transmigration of human neutrophils across airway epithelial cell monolayers is preferentially in the physiologic basolateral-to-apical direction. *Am. J. Respir. Cell Mol. Biol.* **15**, 771–780 (1996).

212. Hu, M. *et al.* Regulation of polymorphonuclear leukocyte apoptosis: role of lung endothelium-epithelium bilayer transmigration. *Am. J. Physiol.-Lung Cell. Mol. Physiol.* **288**, L266–L274 (2005).
213. Huh, D. *et al.* Reconstituting organ-level lung functions on a chip. *Science* **328**, 1662–1668 (2010).
214. Kusek, M. E., Pazos, M. A., Pirzai, W. & Hurley, B. P. In vitro Coculture Assay to Assess Pathogen Induced Neutrophil Trans-epithelial Migration. *J. Vis. Exp. JoVE* (2014) doi:10.3791/50823.
215. Yonker, L. M. *et al.* Development of a Primary Human Co-Culture Model of Inflamed Airway Mucosa. *Sci. Rep.* **7**, 8182 (2017).
216. C. Mejías, J., R. Nelson, M., Liseth, O. & Roy, K. A 96-well format microvascularized human lung-on-a-chip platform for microphysiological modeling of fibrotic diseases. *Lab. Chip* **20**, 3601–3611 (2020).
217. Bai, H. & Ingber, D. E. What can an organ-on-a-chip teach us about human lung physiology? *Physiology* (2022) doi:10.1152/physiol.00012.2022.
218. Huh, D. *et al.* Reconstituting Organ-Level Lung Functions on a Chip. *Science* **328**, 1662–1668 (2010).
219. Barkal, L. J. *et al.* Microbial volatile communication in human organotypic lung models. *Nat. Commun.* **8**, 1770 (2017).
220. Plebani, R. *et al.* Modeling pulmonary cystic fibrosis in a human lung airway-on-a-chip. *J. Cyst. Fibros.* (2021) doi:10.1016/j.jcf.2021.10.004.
221. Bai, H. *et al.* Mechanical control of innate immune responses against viral infection revealed in a human lung alveolus chip. *Nat. Commun.* **13**, 1928 (2022).

222. Cong, H. & Zhang, N. Perspectives in translating microfluidic devices from laboratory prototyping into scale-up production. *Biomicrofluidics* **16**, 021301 (2022).
223. R. Reyes, D. *et al.* Accelerating innovation and commercialization through standardization of microfluidic-based medical devices. *Lab. Chip* **21**, 9–21 (2021).
224. Dobosh, B., Giacalone, V. D., Margaroli, C. & Tirouvanziam, R. Mass production of human airway-like neutrophils via transmigration in an organotypic model of human airways. *STAR Protoc.* **2**, 100892 (2021).
225. Lundholt, B. K., Scudder, K. M. & Pagliaro, L. A Simple Technique for Reducing Edge Effect in Cell-Based Assays. *J. Biomol. Screen.* **8**, 566–570 (2003).
226. Maddox, C. B., Rasmussen, L. & White, E. L. Adapting Cell-Based Assays to the High-Throughput Screening Platform: Problems Encountered and Lessons Learned. *JALA J. Assoc. Lab. Autom.* **13**, 168–173 (2008).
227. Srinivasan, B. *et al.* TEER measurement techniques for in vitro barrier model systems. *J. Lab. Autom.* **20**, 107–126 (2015).
228. Das, V., Fürst, T., Gurská, S., Džubák, P. & Hajdúch, M. Evaporation-reducing Culture Condition Increases the Reproducibility of Multicellular Spheroid Formation in Microtiter Plates. *J. Vis. Exp. JoVE* (2017) doi:10.3791/55403.
229. Douglas S. Auld, P. D. *et al.* *Microplate Selection and Recommended Practices in High-throughput Screening and Quantitative Biology. Assay Guidance Manual [Internet]* (Eli Lilly & Company and the National Center for Advancing Translational Sciences, 2020).

230. Lau, C. Y., Zahidi, A. A. A., Liew, O. W. & Ng, T. W. A direct heating model to overcome the edge effect in microplates. *J. Pharm. Biomed. Anal.* **102**, 199–202 (2015).
231. Kato, H., Tsuchiya, N. & Tokunaga, K. Single nucleotide polymorphisms in the coding regions of human CXC-chemokine receptors CXCR1, CXCR2 and CXCR3. *Genes Immun.* **1**, 330–337 (2000).
232. Vogt, K. L., Summers, C., Chilvers, E. R. & Condliffe, A. M. Priming and de-priming of neutrophil responses in vitro and in vivo. *Eur. J. Clin. Invest.* **48**, e12967 (2018).
233. Vogt, K. L., Summers, C. & Condliffe, A. M. The clinical consequences of neutrophil priming. *Curr. Opin. Hematol.* **26**, 22–27 (2019).
234. Ivetic, A. A head-to-tail view of L-selectin and its impact on neutrophil behaviour. *Cell Tissue Res.* **371**, 437–453 (2018).
235. Hyun, Y.-M. & Hong, C.-W. Deep insight into neutrophil trafficking in various organs. *J. Leukoc. Biol.* **102**, 617–629 (2017).
236. Simard, J.-C., Girard, D. & Tessier, P. A. Induction of neutrophil degranulation by S100A9 via a MAPK-dependent mechanism. *J. Leukoc. Biol.* **87**, 905–914 (2010).
237. Deree, J. *et al.* Neutrophil Degranulation and the Effects of Phosphodiesterase Inhibition. *J. Surg. Res.* **133**, 22–28 (2006).
238. Willems, J., Joniau, M., Cinque, S. & van Damme, J. Human granulocyte chemotactic peptide (IL-8) as a specific neutrophil degranulator: comparison with other monokines. *Immunology* **67**, 540–542 (1989).

239. Futosi, K., Fodor, S. & Mócsai, A. Reprint of Neutrophil cell surface receptors and their intracellular signal transduction pathways. *Int. Immunopharmacol.* **17**, 1185–1197 (2013).
240. Mackerness, K. J., Jenkins, G. R., Bush, A. & Jose, P. J. Characterisation of the range of neutrophil stimulating mediators in cystic fibrosis sputum. *Thorax* **63**, 614–620 (2008).
241. Shute, J., Marshall, L., Bodey, K. & Bush, A. Growth factors in cystic fibrosis – when more is not enough. *Paediatr. Respir. Rev.* **4**, 120–127 (2003).
242. Voynow, J. A., Fischer, B. M. & Zheng, S. Proteases and cystic fibrosis. *Int. J. Biochem. Cell Biol.* **40**, 1238–1245 (2008).
243. De Rose, V. *et al.* Circulating Adhesion Molecules in Cystic Fibrosis. *Am. J. Respir. Crit. Care Med.* **157**, 1234–1239 (1998).
244. Declercq, M., Treps, L., Carmeliet, P. & Witters, P. The role of endothelial cells in cystic fibrosis. *J. Cyst. Fibros.* **18**, 752–761 (2019).
245. Mitola, S. *et al.* Tumor Necrosis Factor- α in Airway Secretions from Cystic Fibrosis Patients Upregulate Endothelial Adhesion Molecules and Induce Airway Epithelial Cell Apoptosis: Implications for Cystic Fibrosis Lung Disease. *Int. J. Immunopathol. Pharmacol.* **21**, 851–865 (2008).
246. Gong, Y. *et al.* Dynamic contributions of P- and E-selectins to β 2-integrin-induced neutrophil transmigration. *FASEB J.* **31**, 212–223 (2017).
247. Kumar, S. D., Krishnamurthy, K., Manikandan, J., Pakeerappa, P. N. & Pushparaj, P. N. Deciphering the key molecular and cellular events in neutrophil transmigration during acute inflammation. *Bioinformation* **6**, 111–114 (2011).

248. Fox, S. E., Lu, W., Maheshwari, A., Christensen, R. D. & Calhoun, D. A. The effects and comparative differences of neutrophil specific chemokines on neutrophil chemotaxis of the neonate. *Cytokine* **29**, 135–140 (2005).
249. Kobayashi, Y. *Neutrophil infiltration and chemokines*. *Critical Reviews in Immunology* (2006). doi:10.1615/critrevimmunol.v26.i4.20.
250. Cruz-Topete, D. & Cidlowski, J. A. Glucocorticoids: Molecular Mechanisms of Action. in *Immunopharmacology and Inflammation* (eds. Riccardi, C., Levi-Schaffer, F. & Tiligada, E.) 249–266 (Springer International Publishing, 2018). doi:10.1007/978-3-319-77658-3_11.
251. Panettieri, R. A. *et al.* Non-genomic Effects of Glucocorticoids: An Updated View. *Trends Pharmacol. Sci.* **40**, 38–49 (2019).
252. Allcock, G. H., Allegra, M., Flower, R. J. & Perretti, M. Neutrophil accumulation induced by bacterial lipopolysaccharide: effects of dexamethasone and annexin 1. *Clin. Exp. Immunol.* **123**, 62–67 (2001).
253. Al-Harbi, N. O. *et al.* Dexamethasone Attenuates LPS-induced Acute Lung Injury through Inhibition of NF- κ B, COX-2, and Pro-inflammatory Mediators. *Immunol. Invest.* **45**, 349–369 (2016).
254. Schwartz, D. M. *et al.* JAK inhibition as a therapeutic strategy for immune and inflammatory diseases. *Nat. Rev. Drug Discov.* **16**, 843–862 (2017).
255. Fragoulis, G. E., McInnes, I. B. & Siebert, S. JAK-inhibitors. New players in the field of immune-mediated diseases, beyond rheumatoid arthritis. *Rheumatology* **58**, i43–i54 (2019).

256. Defnet, A. E., Hasday, J. D. & Shapiro, P. Kinase inhibitors in the treatment of obstructive pulmonary diseases. *Curr. Opin. Pharmacol.* **51**, 11–18 (2020).
257. Kubo, S. *et al.* Janus Kinase Inhibitor Baricitinib Modulates Human Innate and Adaptive Immune System. *Front. Immunol.* **9**, 1510 (2018).
258. Zak, M., Dengler, H. S. & Rajapaksa, N. S. Inhaled Janus Kinase (JAK) inhibitors for the treatment of asthma. *Bioorg. Med. Chem. Lett.* **29**, 126658 (2019).
259. Jorgensen, S. C. J., Tse, C. L. Y., Burry, L. & Dresser, L. D. Baricitinib: A Review of Pharmacology, Safety, and Emerging Clinical Experience in COVID-19. *Pharmacother. J. Hum. Pharmacol. Drug Ther.* **40**, 843–856 (2020).
260. Richardson, P. *et al.* Baricitinib as potential treatment for 2019-nCoV acute respiratory disease. *The Lancet* **395**, e30–e31 (2020).
261. Kremer, J. *et al.* FRI0090 Analysis of neutrophils, lymphocytes, and platelets in pooled phase 2 and phase 3 studies of baricitinib for rheumatoid arthritis. *Ann. Rheum. Dis.* **76**, 512–512 (2017).
262. Hoang, T. N. *et al.* Baricitinib treatment resolves lower-airway macrophage inflammation and neutrophil recruitment in SARS-CoV-2-infected rhesus macaques. *Cell* **184**, 460-475.e21 (2021).
263. Aoki, K. *et al.* Role of CXC chemokines in the enhancement of LPS-induced neutrophil accumulation in the lung of mice by dexamethasone. *Biochem. Biophys. Res. Commun.* **294**, 1101–1108 (2002).
264. Vega, M. A. *et al.* Dexamethasone fails to improve bleomycin-induced acute lung injury in mice. *Physiol. Rep.* **7**, e14253 (2019).

265. Hegeman, M. A. *et al.* Dexamethasone Attenuates VEGF Expression and Inflammation but Not Barrier Dysfunction in a Murine Model of Ventilator-Induced Lung Injury. *PLOS ONE* **8**, e57374 (2013).
266. Hauber, H.-P. *et al.* Effect of HFA-flunisolide on peripheral lung inflammation in asthma. *J. Allergy Clin. Immunol.* **112**, 58–63 (2003).
267. Tien Nguyen, L., Lim, S., Oates, T. & Chung, K. F. Increase in airway neutrophils after oral but not inhaled corticosteroid therapy in mild asthma. *Respir. Med.* **99**, 200–207 (2005).
268. Schleimer, R. P., Freeland, H. S., Peters, S. P., Brown, K. E. & Derse, C. P. An assessment of the effects of glucocorticoids on degranulation, chemotaxis, binding to vascular endothelium and formation of leukotriene B₄ by purified human neutrophils. *J. Pharmacol. Exp. Ther.* **250**, 598–605 (1989).
269. Ronchetti, S., Ricci, E., Migliorati, G., Gentili, M. & Riccardi, C. How Glucocorticoids Affect the Neutrophil Life. *Int. J. Mol. Sci.* **19**, 4090 (2018).
270. S. Saffar, A., Ashdown, H. & S. Gounni, A. The Molecular Mechanisms of Glucocorticoids-Mediated Neutrophil Survival. *Curr. Drug Targets* **12**, 556–562 (2011).
271. Kerachian, M. A. *et al.* Effect of high-dose dexamethasone on endothelial haemostatic gene expression and neutrophil adhesion. *J. Steroid Biochem. Mol. Biol.* **116**, 127–133 (2009).
272. Matsuda, A. *et al.* Corticosteroid enhances TNF- α -mediated leukocyte adhesion to pulmonary microvascular endothelial cells. *Allergy* **63**, 1610–1616 (2008).

273. Forsyth, K. D. & Talbot, V. Role of glucocorticoids in neutrophil and endothelial adhesion molecule expression and function. *Mediators Inflamm.* **1**, 101–106 (1992).
274. Stankova, J., Turcotte, S., Harris, J. & Rola-Pleszczynski, M. Modulation of Leukotriene B4 Receptor-1 Expression by Dexamethasone: Potential Mechanism for Enhanced Neutrophil Survival. *J. Immunol.* **168**, 3570–3576 (2002).
275. Schleimer, R. P. Glucocorticoids Suppress Inflammation but Spare Innate Immune Responses in Airway Epithelium. *Proc. Am. Thorac. Soc.* **1**, 222–230 (2004).
276. Ehrchen, J. M., Roth, J. & Barczyk-Kahlert, K. More Than Suppression: Glucocorticoid Action on Monocytes and Macrophages. *Front. Immunol.* **10**, (2019).
277. Parrillo, J. E. & Fauci, A. S. Mechanisms of Glucocorticoid Action on Immune Processes. *Annu. Rev. Pharmacol. Toxicol.* **19**, 179–201 (1979).
278. Henkels, K. M., Frondorf, K., Gonzalez-Mejia, M. E., Doseff, A. L. & Gomez-Cambronero, J. IL-8-induced neutrophil chemotaxis is mediated by Janus kinase 3 (JAK3). *FEBS Lett.* **585**, 159–166 (2011).
279. Markham, A. Baricitinib: First Global Approval. *Drugs* **77**, 697–704 (2017).
280. Eberl, H. C. *et al.* Chemical proteomics reveals target selectivity of clinical Jak inhibitors in human primary cells. *Sci. Rep.* **9**, 14159 (2019).
281. Mitchell, T. S., Moots, R. J. & Wright, H. L. Janus kinase inhibitors prevent migration of rheumatoid arthritis neutrophils towards interleukin-8, but do not inhibit priming of the respiratory burst or reactive oxygen species production. *Clin. Exp. Immunol.* **189**, 250–258 (2017).

282. Nicole M. Valenzuela. Late phase endothelial cell inflammation is characterized by interferon response genes and driven by JAK/STAT, not NFκB. *Vascul. Pharmacol.* **146**, 107090 (2022).
283. Shi, L., Ramaswamy, M., Manzel, L. J. & Look, D. C. Inhibition of Jak1-Dependent Signal Transduction in Airway Epithelial Cells Infected with Adenovirus. *Am. J. Respir. Cell Mol. Biol.* **37**, 720–728 (2007).
284. Fenwick, P. S., Macedo, P., Kilty, I. C., Barnes, P. J. & Donnelly, L. E. Effect of JAK Inhibitors on Release of CXCL9, CXCL10 and CXCL11 from Human Airway Epithelial Cells. *PLOS ONE* **10**, e0128757 (2015).
285. Bloemen, P. G. *et al.* Stimulation of both human bronchial epithelium and neutrophils is needed for maximal interactive adhesion. *Am. J. Physiol.-Lung Cell. Mol. Physiol.* **270**, L80–L87 (1996).
286. Bonville, C. A. *et al.* Interferon-gamma coordinates CCL3-mediated neutrophil recruitment in vivo. *BMC Immunol.* **10**, 14 (2009).
287. Lei, H., Crawford, M. S. & McCole, D. F. JAK-STAT Pathway Regulation of Intestinal Permeability: Pathogenic Roles and Therapeutic Opportunities in Inflammatory Bowel Disease. *Pharmaceuticals* **14**, 840 (2021).
288. Mizutani, Y., Takagi, N., Nagata, H. & Inoue, S. Interferon- γ downregulates tight junction function, which is rescued by interleukin-17A. *Exp. Dermatol.* **30**, 1754–1763 (2021).
289. Naydenov, N. G. *et al.* Novel mechanism of cytokine-induced disruption of epithelial barriers. *Tissue Barriers* **1**, e25231 (2013).

290. Saatian, B. *et al.* Interleukin-4 and interleukin-13 cause barrier dysfunction in human airway epithelial cells. *Tissue Barriers* **1**, e24333 (2013).
291. Sayoc, A., Preciado, R., Krishnan, M. & McCole, D. F. Tofacitinib Inhibits Intestinal Epithelial JAK-STAT Signaling and Prevents Barrier Dysfunction Induced by Interferon-Gamma (IFN- γ). *FASEB J.* **32**, 873.20-873.20 (2018).
292. Hartwig, O. *et al.* Leaky gut model of the human intestinal mucosa for testing siRNA-based nanomedicine targeting JAK1. *J. Controlled Release* **345**, 646–660 (2022).
293. Dainichi, T. *et al.* The epithelial immune microenvironment (EIME) in atopic dermatitis and psoriasis. *Nat. Immunol.* **19**, 1286–1298 (2018).
294. Hallquist, M. *et al.* The formation, properties and impact of secondary organic aerosol: current and emerging issues. *Atmospheric Chem. Phys.* **9**, 5155–5236 (2009).
295. Joffre, J., Hellman, J., Ince, C. & Ait-Oufella, H. Endothelial Responses in Sepsis. *Am. J. Respir. Crit. Care Med.* **202**, 361–370 (2020).
296. Metwaly, S. M. & Winston, B. W. Systems Biology ARDS Research with a Focus on Metabolomics. *Metabolites* **10**, 207 (2020).
297. Bhargava, M., Higgins, L., Wendt, C. H. & Ingbar, D. H. Application of clinical proteomics in acute respiratory distress syndrome. *Clin. Transl. Med.* **3**, 34 (2014).
298. Calabrese, E. J. The Emergence of the Dose–Response Concept in Biology and Medicine. *Int. J. Mol. Sci.* **17**, 2034 (2016).
299. Plenge, R. M., Scolnick, E. M. & Altshuler, D. Validating therapeutic targets through human genetics. *Nat. Rev. Drug Discov.* **12**, 581–594 (2013).

300. Matthay, M. A. *et al.* Phenotypes and personalized medicine in the acute respiratory distress syndrome. *Intensive Care Med.* **46**, 2136–2152 (2020).
301. The ARDSnet Investigators *et al.* Personalized medicine for ARDS: the 2035 research agenda. *Intensive Care Med.* **42**, 756–767 (2016).
302. Clancy, J. P. & Jain, M. Personalized Medicine in Cystic Fibrosis. *Am. J. Respir. Crit. Care Med.* **186**, 593–597 (2012).
303. Paggi, D. A. & Polack, F. P. Toward Personalized Medicine in Bronchiolitis. *Am. J. Respir. Crit. Care Med.* **199**, 1456–1458 (2019).
304. Schuetz, P. Personalized medicine of patients with respiratory infections through the measurement of specific blood biomarkers: fact or fiction? *Expert Rev. Respir. Med.* **11**, 605–607 (2017).
305. Matthay, M. A. *et al.* Acute respiratory distress syndrome. *Nat. Rev. Dis. Primer* **5**, (2019).
306. Khemani, R. G. *et al.* Paediatric acute respiratory distress syndrome incidence and epidemiology (PARDIE): an international, observational study. *Lancet Respir. Med.* **7**, 115–128 (2019).
307. Chiang, C.-C., Korinek, M., Cheng, W.-J. & Hwang, T.-L. Targeting Neutrophils to Treat Acute Respiratory Distress Syndrome in Coronavirus Disease. *Front. Pharmacol.* **11**, 572009 (2020).
308. Pugin, J., Verghese, G., Widmer, M. C. & Matthay, M. A. The alveolar space is the site of intense inflammatory and profibrotic reactions in the early phase of acute respiratory distress syndrome. *Crit. Care Med.* **27**, 304–312 (1999).

309. Zemans, R. L. & Matthay, M. A. What drives neutrophils to the alveoli in ARDS? *Thorax* **72**, 1–3 (2017).
310. Vassallo, A., Wood, A. J., Subburayalu, J., Summers, C. & Chilvers, E. R. The counter-intuitive role of the neutrophil in the acute respiratory distress syndrome. *Br. Med. Bull.* **131**, 43–55 (2019).
311. Grunwell, J. R. *et al.* Neutrophil Dysfunction in the Airways of Children with Acute Respiratory Failure Due to Lower Respiratory Tract Viral and Bacterial Coinfections. *Sci. Rep.* **9**, 2874 (2019).
312. Song, C. *et al.* NETs promote ALI/ARDS inflammation by regulating alveolar macrophage polarization. *Exp. Cell Res.* **382**, 111486 (2019).
313. Smedly, L. A. *et al.* Neutrophil-mediated injury to endothelial cells. Enhancement by endotoxin and essential role of neutrophil elastase. *J. Clin. Invest.* **77**, 1233–1243 (1986).
314. Bosmann, M. *et al.* Extracellular histones are essential effectors of C5aR- and C5L2-mediated tissue damage and inflammation in acute lung injury. *FASEB J.* **27**, 5010–5021 (2013).
315. Bendib, I., Chaisemartin, L. de, Dessap, A. M., Chollet-Martin, S. & Prost, N. de. Understanding the Role of Neutrophil Extracellular Traps in Patients With Severe Pneumonia and ARDS. *CHEST* **156**, 1278–1280 (2019).
316. Simon, R. H., DeHart, P. D. & Todd, R. F. Neutrophil-induced injury of rat pulmonary alveolar epithelial cells. *J. Clin. Invest.* **78**, 1375–1386 (1986).

317. Grunwell, J. R. *et al.* Differential type I interferon response and primary airway neutrophil extracellular trap release in children with acute respiratory distress syndrome. *Sci. Rep.* **10**, 19049 (2020).
318. Iwata, K. *et al.* Effect of Neutrophil Elastase Inhibitor (Sivelestat Sodium) in the Treatment of Acute Lung Injury (ALI) and Acute Respiratory Distress Syndrome (ARDS): A Systematic Review and Meta-Analysis. *Intern. Med.* **49**, 2423–2432 (2010).
319. Aikawa, N. & Kawasaki, Y. Clinical utility of the neutrophil elastase inhibitor sivelestat for the treatment of acute respiratory distress syndrome. *Ther. Clin. Risk Manag.* **10**, 621–629 (2014).
320. Zhang, Y. *et al.* Effects of N-acetylcysteine treatment in acute respiratory distress syndrome: A meta-analysis. *Exp. Ther. Med.* **14**, 2863–2868 (2017).
321. Sweeney, T. E. *et al.* Multicohort Analysis of Whole-Blood Gene Expression Data Does Not Form a Robust Diagnostic for Acute Respiratory Distress Syndrome. *Crit. Care Med.* **46**, 244–251 (2018).
322. Wilson, J. G. & Calfee, C. S. ARDS Subphenotypes: Understanding a Heterogeneous Syndrome. in *Annual Update in Intensive Care and Emergency Medicine 2020* (ed. Vincent, J.-L.) 67–79 (Springer International Publishing, 2020). doi:10.1007/978-3-030-37323-8_5.
323. Calfee, C. S. *et al.* Acute respiratory distress syndrome subphenotypes and differential response to simvastatin: secondary analysis of a randomised controlled trial. *Lancet Respir. Med.* **6**, 691–698 (2018).

324. Famous, K. R. *et al.* Acute Respiratory Distress Syndrome Subphenotypes Respond Differently to Randomized Fluid Management Strategy. *Am. J. Respir. Crit. Care Med.* **195**, 331–338 (2016).
325. Calfee, C. S. *et al.* Subphenotypes in acute respiratory distress syndrome: latent class analysis of data from two randomised controlled trials. *Lancet Respir. Med.* **2**, 611–620 (2014).
326. Yamamoto, H., Sedgwick, J. B., Vrtis, R. F. & Busse, W. W. The Effect of Transendothelial Migration on Eosinophil Function. *Am. J. Respir. Cell Mol. Biol.* **23**, 379–388 (2000).
327. Gröbner, S., Lukowski, R., Autenrieth, I. B. & Ruth, P. Lipopolysaccharide induces cell volume increase and migration of dendritic cells. *Microbiol. Immunol.* **58**, 61–67 (2014).
328. Paradis, A., Leblanc, D. & Dumais, N. Optimization of an in vitro human blood–brain barrier model: Application to blood monocyte transmigration assays. *MethodsX* **3**, 25–34 (2016).
329. Mooren, O. L., Li, J., Nawas, J. & Cooper, J. A. Endothelial cells use dynamic actin to facilitate lymphocyte transendothelial migration and maintain the monolayer barrier. *Mol. Biol. Cell* **25**, 4115–4129 (2014).